Near infrared variability phenomena in young stellar objects

Catarina Alves de Oliveira

München, 2008

Near infrared variability phenomena in young stellar objects

Catarina Alves de Oliveira

Dissertation
an der Fakultät für Physik
der Ludwig–Maximilians–Universität
München

vorgelegt von
Catarina Alves de Oliveira
aus Afife, Portugal

München, den 4. Juli 2008

Erstgutachter: Prof. Dr. Andreas Burkert
Zweitgutachter: Prof. Dr. Henk Spruit
Tag der mündlichen Prüfung: 17. September 2008

Zusammenfassung

Diese Dissertation stellt eine Beobachtungsstudie des ρ Ophiuchi Sternhaufens, eines der uns am nächsten gelegenen Sternentstehungsgebiete, vor und verfolgt das Ziel Sternaktivität in jungen stellaren Objekten zu charakterisieren. Variabilität ist ein allgemeines Merkmal von Vorhauptreihensternen und hat ihren Ursprung in Vorgängen, die im Zusammenhang mit magnetischen Feldern, Akkretionsscheiben und zirkumstellarer Extinktion stehen. Variabilitätsdurchmusterungen im Infraroten geben Einsichten in die stellaren und zirkumstellaren Umgebungen und liefern Informationen über die Dynamik der magnetischen Vorgänge und Akkretionsprozesse. Für die vorliegende Studie wurde eine photometrische Untersuchung von ρ Ophiuchi im Nahinfraroten über ein grosses Gesichtsfeld von $\sim$0.8 deg^2 ausgeführt. Dabei wurde der Sternhaufen in 14 Nächten verteilt über 2 Jahre mit der Wide Field Camera (WFCAM) am United Kingdom Infrared Telescope beobachtet. Statistische Methoden wie der multi-band Kreuzkorrelationsindex und das reduzierte Chi-Quadrat Verfahren wurden benutzt um Variabilität zu identifizieren und vom Rauschen der Messung zu unterschieden. Variabilität im Nahinfrarot wurde für die Hälfte der bekannten ρ Ophiuchi Sterne nachgewiesen. Verschiedene Variabilitätsmuster treten auf und können dem Vorhandensein von Flecken auf der Sternoberfläche, Veränderungen der zirkumstellaren Extinktion oder Änderungen in der Akkretionsscheibengeometrie zugeordnet werden.

Darüber hinaus wird in dieser Dissertation untersucht, ob photometrische Variabilität als Auswahlkriterium für neue leuchtkraftarme Mitglieder von galaktischen Sternenstehungsgebieten mit bis hin zu sehr kleinen Massen herangezogen werden kann. Dieses neue Auswahlverfahren kann dabei helfen Verzerrungen anderer Methoden zu beseitigen. So können mit diesem Verfahren zum Beispiel junge Quellen identifiziert werden, die keinen Infrarotexzess aufweisen oder schwache Hα Emission zeigen. Diese kürzlich entdeckte Methode kann erheblich dazu beitragen eine vollständige Erhebung aller jungen Objekte in Sternenstehungsgebieten zu erhalten, welches als wichtigstes Ziel von galaktischen Sternenstehungsstudien verbleibt. Aufgrund ihrer Variabilität wurde eine neue Population von Objekten entdeckt, die vermutlich Teil des ρ Ophiuchi Sternhaufens ist. Vier mögliche Mitglieder wurden mittels niedrigauflösender Nahinfrarotspektroskopie als Vorhauptreihensterne bestätigt.

Schliesslich ist die vorliegende Studie die erste ihrer Art im Infraroten, sowohl bezüglich der Grösse des untersuchten Gebietes als auch ihrer Empfindlichkeit, wobei kürzliche Entwicklungen für Instrumente der Infrarotastronomie eingesetzt wurden. Für zukünftige Variabilitätsstudien im Infraroten ist das Instrument HAWK-I (High-Acuity Wide-field K-band Imager), das neue Infrarot-Instrument am Very Large Telescope, von Bedeutung. Dieses ist die zurzeit am weitesten entwickelte Infrarot-Kamera an einem 8-meter Teleskop. Dieses Instrument wurde während der Dissertationszeit montiert und in Betrieb genommen und wird mit Schwerpunkt auf den Beitrag der Autorin zu diesem Projekt vorgestellt.

Abstract

This thesis presents an observational study of one of the nearest star-forming regions, the ρ Ophiuchi cluster, with the goal of characterising stellar activity in young stellar objects. Variability is a common characteristic of pre-main-sequence (PMS) stars and originates from mechanisms related to magnetic fields, accretion discs, and circumstellar extinction. Variability surveys in the infrared (IR) can probe stellar and circumstellar environments and provide information about the dynamics of the on going magnetic and accretion processes. To this end, a large-field ($\sim$0.8 deg^2), near-IR photometric survey of ρ Ophiuchi has been conducted using the Wide Field Camera (WFCAM) at the United Kingdom Infrared Telescope (UKIRT), which monitored the cluster over 14 nights in two consecutive years. Statistical tools, such as the multi-band cross correlation index and the reduced chi-square, were used to disentangle signals of variability from noise. Variability in the near-IR is found to be present in half of the known population of ρ Ophiuchi. The behaviours shown are several and can be associated with the existence of spots on the stellar surface, variations in circumstellar extinction, or changes in the geometry of an accretion disc.

Furthermore, this thesis explores the feasibility of using photometric variability as a criterion for selection of new low-luminosity candidates of galactic star forming regions down to very low masses. The use of this new selection method could help remove the biases from other techniques. For example, it has the advantage of identifying young sources that do not show IR-excess or have small Hα emission. The use of this relatively new technique should contribute significantly to obtain a full census of the young objects in star formation regions, which remains one of the most important goals of galactic star formation studies. Using variability, a new population of objects has been uncovered, that is believed to be part of the ρ Ophiuchi cluster. Using low-resolution near-IR spectroscopy, 4 candidate members have been confirmed as PMS stars.

Finally, the survey presented in this thesis is the first of its kind in the IR, both in large area surveyed and sensitivity, taking advantage of recent developments in IR astronomical instrumentation. Of future relevance for IR variability studies is the new IR-imager at the Very Large Telesope (VLT), HAWK-I (High-Acuity Wide-field K-band Imager), the most advanced IR camera on an 8-meter telescope at the present moment. The instrument was assembled and commissioned during the progress of this thesis, and is presented here, giving emphasis to the contribution of the author to the project.

Contents

List of Figures

List of Tables

Chapter 1

Introduction

1.1 Motivation

It is now commonly accepted that stars form in giant molecular clouds, which fragment and begin to collapse giving origin to protostellar objects. The observational characteristics of these young objects in their very first evolutionary stages are the fingerprints of the physics involved in their formation process. Although there are general accepted views on the way star-formation occurs and young stellar objects (YSOs) evolve to the main-sequence, there is still a long way to go between the broader theories and an agreed paradigm which can explain in detail the wide range of existing observational properties of YSOs. For example, despite the fact that it is now accepted that the properties of YSOs are governed by magnetic fields and accretion, several questions remain regarding how the star-disc interaction takes place, or how magnetic fields evolve as stars approach the main-sequence. The same is true for the study of discs around YSOs. Their existence has long been predicted, and direct confirmation achieved. However, some of the basic properties, such as the disc masses and mass-accretion rates, are still unknown and largely debated. These constitute fundamental problems that must be solved in order to understand other mechanisms, such as the angular momentum regulation, which allow the young star to evolve without disrupting, as well as the evolution and stability of a potential planet-forming disc.

The complex nature of these phenomena calls for the use of several diagnostics which can probe different parts of a system when studying YSOs. Although only spectroscopy can tackle the details of the ongoing processes and dynamics, it is the use of imaging techniques that can provide extensive knowledge on large samples of young stellar clusters. The variability of YSOs, both spectral and photometrical, has been a defining characteristic of these objects from the very start of their study. This makes the inclusion of the time domain necessary when studying their properties. Thus, photometric variability studies of entire clusters, as the study presented in this thesis, can provide a large dataset of photometric properties of many coeval YSOs over a significant time range. These also have a future value for detailed follow-up of objects where

variability is tracing the physical phenomena responsible for the evolution of YSOs.

1.2 Young stars: from discovery to the current paradigms

1.2.1 An historical overview

The class of 'T Tauri variable stars' was defined in the classical work of Joy (1945), although at the time the young nature of these objects was still unknown. In his 1945 paper, Joy defined photometric and spectroscopically this new class of objects as being low luminosity stars associated with dark or bright nebulosity, showing irregular light variations of about 3 mag, and having spectral types F5 to G5 with emission lines that resemble the solar chromosphere. Additional discoveries of T Tauri stars followed Joy's work in Taurus (Joy 1949) and Ophiuchus (Struve & Rudkjøbing 1949). At that time, T Tauri stars were always seen in association with nebulosity and thought of as being stars moving through an interstellar cloud. In parallel to these discoveries, Ambartsumian (1954) was proposing OB and T associations as sites of ongoing star-formation, where groups of stars formed from the same molecular cloud. The combination of both discoveries resulted in a paradigm shift, where the idea of stars passing through an interstellar cloud was abandoned in favour of a scenario where stars are born in interstellar clouds (Bertout 2007). Later, Herbig (1962) defined the class of T Tauri stars using only spectroscopic information, which should show in their spectra hydrogen, CaII, FeI λ4063 $\mathring{A}$ and λ4132 $\mathring{A}$ emission lines, and usually, but not always, [SiII] λ4068, 4076, 6716, 6731 $\mathring{A}$, and [OI] λ6300, 6363 $\mathring{A}$ also in emission. Furthermore, Herbig proposed for the first time strong LiI λ6707 $\mathring{A}$ absorption as a possible defining characteristic. These criteria are now used to define the class of classical T Tauri stars (hereafter, CTTS), and the strong LiI absorption is known to be a defining characteristic of their youth (Martin et al. 1998).

Despite these advances, many questions remained unsolved in the study of T Tauri stars. Although several observations of optical and UV 'veiling' (photospheric absorption lines are seen filled in, in what is now known to be caused by the excess continuum emission from the region where the accretion shocks occur, see for example, Gullbring et al. 2000) kept on appearing, there was still no credible explanation for this phenomenon. It was only in the 1970's that Walker (1972) proposed the existence of a circumstellar disc to explain the spectroscopic properties of YY Ori stars and Lynden-Bell & Pringle (1974) built a theoretical foundation to this empirical disc picture. However, there was no general acceptance of this view at the time, and almost a decade had to go by until the idea was revisited. The 1980's were the stage for a succession of observational discoveries lead by the launch of the first space observatories which started probing the X-ray regime (e.g., Giacconi 1981, and references

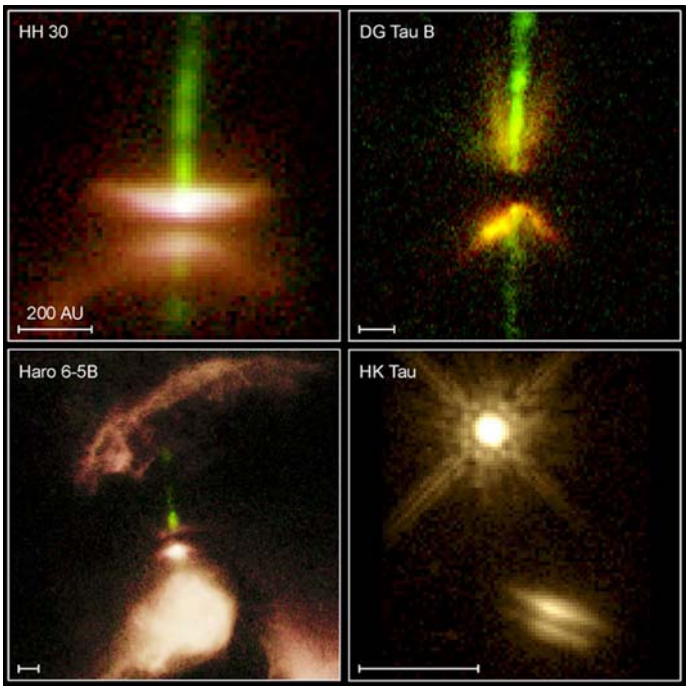

Figure 1.1: Discs and jets around young stars as observed by the Hubble Space Telescope. Credits: HST NASA/ESA

therein). The advances in theory kept pace with the new observations and the disc hypothesis for T Tauri stars re-emerged at the end of that decade (e.g., Shu et al. 1987; Strom et al. 1989, and many others, see Bertout (2007) and references therein). Walter (1987) presented the properties for a new class of T Tauri stars which do not have a circumstellar disc, and are now known as weak-emission lines TTSs (hereafter, WTTSs). These results mark a turning-point in the study of T Tauri stars and from 1990 on, the paradigm of the accretion disc becomes the framework in T Tauri stars' research. The late 1990's and the turn of the century is marked by the long awaited first direct images of circumstellar discs around T Tauri stars from the Hubble Space Telescope (see Fig. 1.1)and Adaptive Optics (e.g., Burrows et al. 1996).

The following sections provide an overview of today's understanding on YSOs, placing emphasis on the areas of most relevance for this thesis. For more complete discussions, the reader is referred to the literature, in particular to the proceedings of two recent conferences, Protostars & Planets V (Reipurth et al. 2007b) and IAU Symposium 243, Star-Disk Interaction in Young Stars (Bouvier & Appenzeller 2007), which gathered today's experts on the field and contain the most up-to-date discussions on the theory and observations of star formation in our Galaxy.

1.2.2 Pre-main-sequence stars

In the last 60 years, from when star formation studies began, much progress has been made to get to the point we are now. There is a general accepted view that stars form from giant molecular clouds that fragment into dense cores, which collapse resulting in protostars, the first stage of the evolution of a star towards the main-sequence. Larson (1969) did the first studies on the gravitational collapse of a stellar core, considering a gas cloud which is spherically symmetric, and has no rotation or magnetic fields. The collapse is triggered by an exterior factor and proceeds on the free-fall timescale. In 1987, Shu et al. (1987) introduced the inside-out-collapse scenario, generally used today to broadly explain the formation of a protostar. In this framework, the central parts of the core collapse faster than the outer layers, which collapse only when hit by an outward propagating expansion wave at the speed of sound. According to this model, a core is formed after a short time, which continues accreting from the surrounding material at a constant rate. Shu et al. (1987) described the formation of a star in four stages, shown as a, b, c, and d in Fig. 1.2. In the first stage, the clumps of dust and gas inside the molecular cloud collapse and give origin to slowly rotating cloud cores. The second stage takes place when the mass of the clumps exceeds a critical equilibrium limit and the dynamical collapse of the clump takes place in the inside-out fashion mention above, forming a central protostar with a surrounding accretion disc. At this stage, there is an optically thick and accreting disc, deeply embedded in an infalling envelope which feeds mass onto the central object, making this phase only visible at millimetre wavelengths. During the third stage, the star has already reached a high enough core temperature and ignites the fusion of deuterium, which is accreted from the envelope and transported to the centre of the star by convection. Simultaneously, a stellar wind driven by convection breaks up causing collimated jets and bipolar outflows. The last stage of the evolution is a young star (e.g., a T Tauri star) with a surrounding disc which will decay as the star evolves onto the main sequence. This represents, however, a very classical view of the collapse of a cloud. Present work has set aside the spherical symmetry condition, and added the effect of rotation and magnetic fields in clouds on the collapse. The consideration of these factors has a strong impact on the understanding of the dynamics of the infalling gas and the way matter flows onto the core (see Reipurth et al. 2007b, for recent discussions).

After a protostar is formed, it will undergo several evolutionary stages as it approaches the main-sequence. Several classifications schemes have been suggested for YSOs at their various evolutionary phases. Lada & Wilking (1984) studied the embedded population of the ρ Ophiuchus molecular cloud and, combining broad-band fluxes from 1 to 20 μm, determined the broad band spectral energy distribution (SED), i.e. $\log(\lambda\ F_\lambda)$ vs. $\log(\lambda)$ of several YSOs and concluded that the shapes of the SEDs can be used to distinguish different morphological classes. Based on the level of long wavelength excess with respect to a stellar photospheric emission, they identify three different classes which define an IR-excess or SED classification scheme: Class I, SED rising

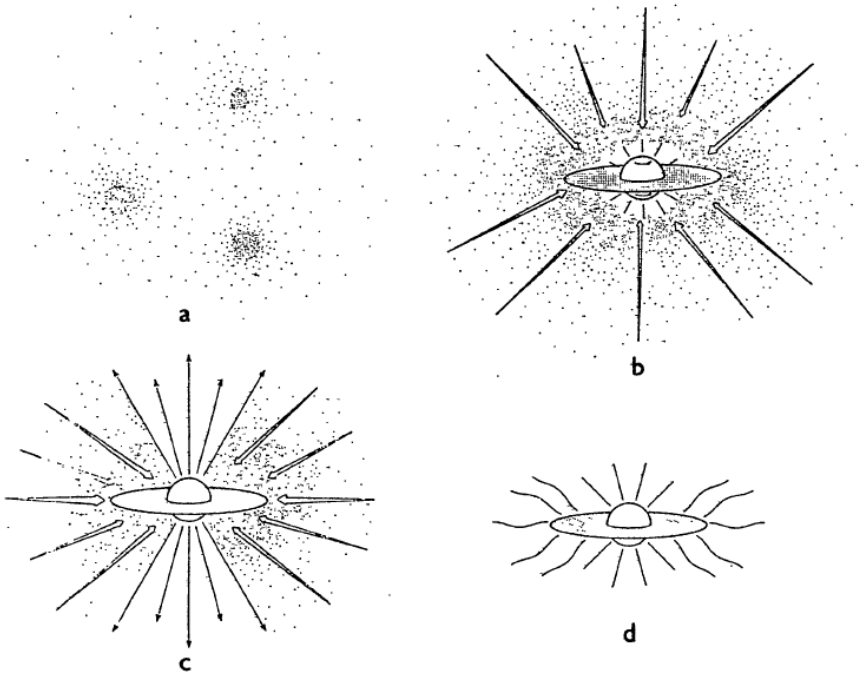

Figure 1.2: The four stages of star formation (Shu et al. 1987).

longward of 2 μm, Class II, flat or decreasing SED longward of 2 μm, and Class III, little or none IR-excess. Later, Lada (1987) provided a more quantitative criterion, defining a spectral index, given by:

$$\alpha = \frac{dlog(\lambda F_\lambda)}{dlog(\lambda)}, \tag{1.1}$$

where for Class I sources $0 < \alpha < +3$, for Class II $-2 < \alpha < 0$, and for Class III $-3 < \alpha < -2$. Andre et al. (1993) mapped the submillimeter continuum emission in the core ρ Oph A and found embedded sources which they classify as a new class of YSOs. These objects show a strong submillimeter emission and remain undetected at $\lambda < 10$ μm, indicating they have more circumstellar material than Class I objects. They propose to name them Class 0 sources. Figure 1.3 shows the SED for the different classes from 1 to 100 μm.

Morphologically, there is a parallel between the IR classification and the common designation of Classical T Tauri stars (CTTSs) and Weak T Tauri stars (WTTSs), explained as follows: Class I, low mass protostars surrounded by an infalling envelope with large IR-excess; Class II, young stars with accretion discs and a moderate IR-excess (as in CTTSs); and Class III, stars which no longer accrete matter from a circumstellar disc and show no IR-excess (as in WTTSs). Both nomenclatures are used throughout this thesis.

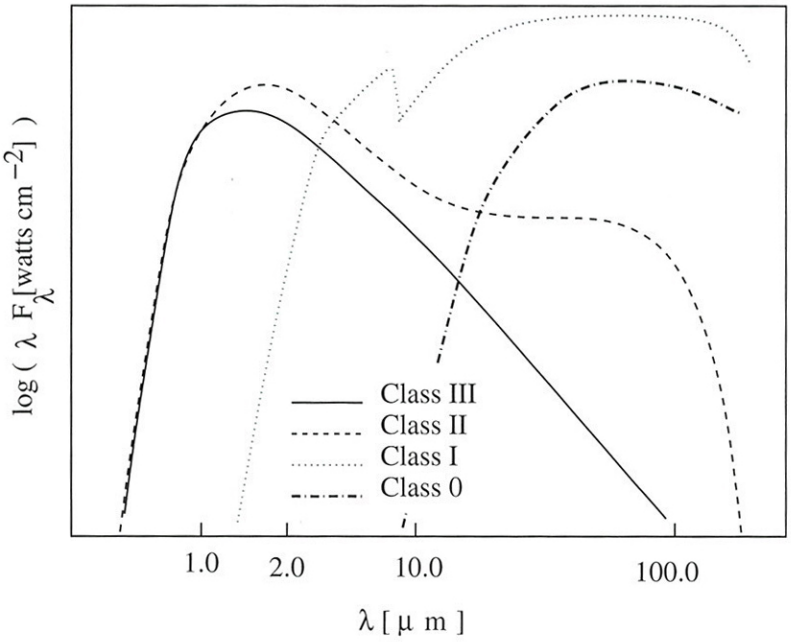

Figure 1.3: SED classification of PMS stars (Schulz 2005).

1.2.3 Accretion processes and magnetic activity in PMS stars

Classical T Tauri stars are surrounded by accretion discs from which they accrete a large amount of matter, while still contracting on their way to the main-sequence. Therefore, assuming angular momentum conservation, they should be spinning up as they evolve. But that is not the case, with observations showing that they are, in fact, slow rotators. Stars with masses from 0.4 $M_\odot$ to 1.5 $M_\odot$ show a bimodal distribution with peaks around ∼2 and ∼8 days in the Orion Nebula Cluster (ONC), and ∼1 and ∼4 days in NGC 2264 (Herbst et al. 2007), whereas the periods corresponding to the breakup velocity of these stars are ∼0.5 days (Stassun et al. 1999). Stars with masses less than 0.4 $M_\odot$ show a period distribution which ranges from a few hours up to 10 days, with slow rotators much rarer, and some brown dwarfs have even been observed to rotate at velocities close to the breakup period, which is ∼2 hours (Herbst et al. 2007). This means that a mechanism is needed to redistribute angular momentum during the collapse and early formation stages of these stars, but such a process has not yet been fully understood. This is one of the fundamental unsolved questions in star formation and is commonly called the *angular momentum problem*.

The best current idea for solving this problem is the occurrence of magnetically controlled accretion from the disc onto its parent star. The origins of the magnetic field in young stars are still largely debated. The most accepted idea is that magnetic fields are generated in a stellar dynamo on the interface between the radiative

and convective zone, and then buoy to the surface through the convective zone (e.g., Feigelson et al. 2003; Brun & Zahn 2006). These magnetic fields generate activity on the stellar surface, seen as cool spots (Donati et al. 2008). The existence of strong magnetic fields in T Tauri stars had already been suggested in the 1980's, for example, based on their strong X-ray emissions (e.g., Montmerle et al. 1983). These predictions were confirmed with the first measurements of surface magnetic fields of the order of 1-3 kG (e.g., Johns-Krull et al. 1999).

The magnetospheric accretion paradigm came to general acceptance in the 1990's (Koenigl 1991; Collier Cameron & Campbell 1993; Shu et al. 1994), and, in broad terms, suggests that the inner disc is truncated by a strong stellar magnetic field and the material is accreted onto the star along magnetic field lines. In formal terms, if the magnetic field of the star is sufficiently strong, the accretion of material (which needs to be ionised) will be governed by the stellar field when its ram pressure, defined as:

$$P_{ram} = 0.5\rho\nu^2, \tag{1.2}$$

where ρ is the density of the gas and ν the orbital velocity, equals the magnetic pressure, defined as:

$$P_B = \frac{B^2}{8\pi}, \tag{1.3}$$

where B is the magnetic field strength. This point is called the truncation radius and is expected to be placed at a distance of a few stellar radii from the star's surface (Camenzind 1990; Koenigl 1991). The material is then accreted in free fall from the inner disc onto the star along magnetic field lines (see Fig. 1.4). One of the most commonly used diagnostics of accretion in T Tauri stars is the presence of Hα in emission, which is believed to arise both from this accretion funnel and the accretion shock. An equivalent width of Hα emission $> 10\mathring{A}$ is interpreted as a signature of ongoing accretion, while smaller values are attributed simply to chromospheric activity. The magnetospheric accretion theories also suggest that when the star-disc system is in equilibrium, the Keplerian rotation rate of the disc at the truncation point will regulate the rotation of the central star (commonly known as disk locking theories, as proposed by Koenigl (1991)).

1.2.4 Initial Mass Function and Brown Dwarfs

In the last decades, observational evidence has shown that most of the stars form in groups (see, for example, the review by Lada & Lada 2003). However, many questions remain regarding which factors dictate the way star formation occurs in different regions of the Galaxy. For example, it is still not understood if triggered star formation, a process where the formation of massive stars in a region can trigger star formation in

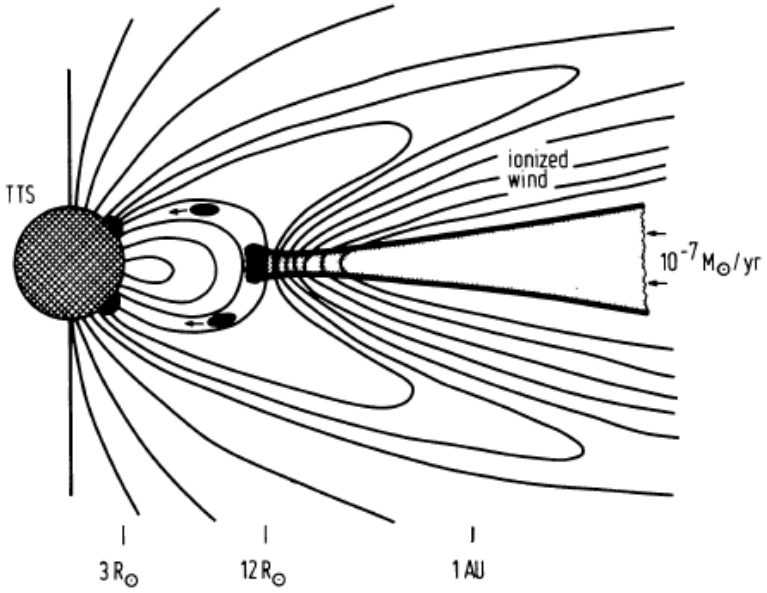

Figure 1.4: Magnetospheric accretion in a CTTS (figure from Camenzind (1990)).

a nearby molecular cloud, would produce different results from independent star formation, and which of these processes is capable of originating all the different flavours of open clusters that are observed today (see Elmegreen 2006, and the discussion papers therein). The initial mass function (IMF) is an empirical relation which describes the mass distribution of stars that form in a finite space, at a determined star formation event. Measuring the IMF as a function of environment (metallicity, cluster density, etc) is an important and much attempted goal of star formation (e.g. Bonnell et al. 2007, and references therein). The comparison of the IMF from different star forming regions would help answering some of the key questions, such as the timescale for star formation within a molecular cloud, or the role of the environment in determining the stellar masses. The extension of the IMF to the brown dwarf and planetary regime and the search for the end of the mass function would provide a new insight into the processes of formation of low-mass stars and brown dwarfs. Therefore, one of the prime goals of modern observations of star forming regions is to achieve completeness at the lower mass end, i.e., the brown dwarf regime.

Brown dwarfs (BDs) are defined as substellar objects, with masses below $\lesssim$75 M$_{Jup}$ (Chabrier & Baraffe 1997), which are unable to sustain hydrogen fusion in their cores. Brown dwarfs with masses $\gtrsim$12 M$_{Jup}$ go through a period of Deuterium fusion after which they become fainter as they cool down. Their existence was first predicted from theory (Kumar 1963; Hayashi & Nakano 1963) but it took almost 30 years until the discovery of the first brown dwarfs was made (Rebolo et al. 1995; Nakajima et al.

1995; Oppenheimer et al. 1995). Since then, many hundreds have been detected in large surveys, both in the field and in young stellar clusters, leading to the suggestion that they might even exist in equal number density to low-mass stars (Chabrier 2003). Young BDs are brighter and have warmer temperatures than older field dwarfs, making them easier to observe at early stages. BDs with masses below $\lesssim$12 M_{Jup} are usually called planetary-mass brown dwarfs and are too small even to burn Deuterium (Chabrier et al. 2000). The increasing number of detections of such objects (Lucas & Roche 2000; Zapatero Osorio et al. 2000; Najita et al. 2000) has challenged the existing scenarios for stellar and substellar formation. In fact, several questions remain unanswered relating to the formation process of BDs and it is still not understood whether they form in the same way as hydrogen-burning stars or not, and if the mechanisms that form BDs are different from those of planet formation.

There are four proposed mechanisms to explain the formation of BDs: turbulent fragmentation (Padoan & Nordlund 2002), disc fragmentation, dynamical ejection (Reipurth & Clarke 2001), and photo-erosion (Hester et al. 1996). As more observations of BD properties are done, the indications are that they are able to form in the same way as H-burning stars, i.e., through cloud fragmentation (Luhman et al. 2007). Since the above BDs scenarios are not mutually exclusive, they can still occur in conjunction with the more plausible mechanism of cloud fragmentation, though most likely in smaller numbers (Whitworth et al. 2007).

Although the formation process of BDs is still largely debated, their properties are now better known. The first spectroscopic studies have suggested that BDs probably undergo an analogous T Tauri phase, as in a young star (e.g., Luhman et al. 1997). In the recent years, large surveys have found that the presence of discs around BDs is just as common as in stars, and convincing evidence of ongoing accretion has been revealed by several diagnostics, such as the presence of asymmetric broad Balmer line profiles and continuum veiling (see Luhman et al. 2007, and references therein for a review). Using high resolution spectroscopy, a large number of spectra of BDs already exist, which show that accretion is detected through all BD masses. In addition, free-fall infall velocities have also been measured, suggesting that the magnetospheric accretion paradigm which has explained most of the observed characteristics in young stars can, most probably, be extended to the BD regime (Mohanty 2007).

1.3 Photometric variability in YSOs

Young stars have been known to be variable since Joy (1945) described the irregular behaviour of T Tauri stars. Photometric variability is thought to originate from several mechanisms related to magnetic fields, accretion discs, and circumstellar extinction (Herbst et al. 1994). Most of the variability studies have been done in the optical and

have been used as an excellent tool for characterising stellar and circumstellar environments of pre-main-sequence stars (e.g., Grankin et al. 2007, 2008) and brown dwarfs (e.g., Caballero et al. 2004; Scholz & Eislöffel 2005). Detailed studies to determine the physical causes of variability in T Tauri stars have been carried out, in the optical, for large samples (e.g., Herbst et al. 1994; Bouvier et al. 1995). These major studies identify the different causes of photometric variability of pre-main-sequence stars, which have been recently reviewed by Herbst et al. (2007) and can be summarised as follows:

- *Rotational modulation by cool starspots:* Cool starspots are known to exist both in CTTSs and WTTSs, and to cause variations in the stellar brightness. In comparison to cool spots, they are colder than the photosphere and arise from magnetic active regions, analogously to solar sunspots (Bouvier & Bertout 1989). The fractional area coverage is of the order of ∼30% (Bouvier et al. 1993; Herbst et al. 1994) which determines the maximum amplitude of ∼0.4 magnitudes in V (Carpenter et al. 2001; Herbst et al. 2002). Herbst et al. (1994) presented a classification scheme for optical variability, defining as type I variable stars with low, periodic, amplitude magnitude variations (a few tenths of a magnitude) caused by cool spots. Photometric variability studies of very low mass stars and brown dwarfs have identified similar behaviours (e.g., Scholz & Eislöffel 2005).

- *Rotational modulation by hot starspots:* Hot spots are interpreted as the impact points on the stellar surface from disc accretion through magnetic field lines (e.g., Calvet & Hartmann 1992). They cover a smaller fraction of the stellar surface but the high temperatures can cause larger amplitude variations, which in the near-IR regime can be as high as 0.2-0.4 magnitudes for the *JHK* bands, and between 0.05-0.12 in $J-H$ and $H-K$ colours (Carpenter et al. 2001). The timescales over which the variations persist are shorter compared to cool spots (e.g., Kenyon et al. 1994). In the Herbst et al. (1994) classification scheme, a type II variability class is assigned to objects showing larger amplitude variations (which can be irregular, II, or periodic, IIp), from short-lived hot spots.

- *Circumstellar Extinction:* Variations in extinction can originate from the intersection with the line-of-sight of infalling or orbiting material in the circumstellar environment. Circumstellar extinction variations will follow a reddening law if the grain size of the material is comparable to the interstellar grain size distribution (Skrutskie et al. 1996).

- *Accretion Discs:* Changes in the disc structure change the amount of light that is reprocessed by the disc, causing variability. The reasons for such a structural change are thought to be twofold, with both mechanisms depending fundamentally on the star's magnetic field and its relation with an accreting disc. One

possible scenario is that the variations are caused by changes in the accretion rate. The truncation radius of the accreting disc is, according to the magnetospheric accretion paradigm, dependent on the accretion rate and the magnetic field strength. As such, in presence of a variable magnetic field, the truncation radius would vary, causing changes in the accretion rate (e.g., Carpenter et al. 2001, and references therein). Another possibility is that the photometric variations are a final product of warping instabilities. The inner region of a disc, locked to its parent star, will undergo magnetic torques that induce warping and precession on the disc. Therefore, as the inner part of the disc warps and precesses, it gets exposed to different magnetic field strengths, which results in a variation in the truncation radius (Lai 1999).

- *Extreme variability:* Some young stars show large amplitude variations of several magnitudes in a short amount of time (∼few days). These can be irregular, but repeated, photometric variations (known as UXors), or a burst followed by a gradual, but steady, decrease in brightness (referred to as FU Ori-type). The reason behind these extreme variations is not yet known, but in the case of UXors the favoured theory is changes in the circumstellar extinction (Herbst & Shevchenko 1999), while FU Ori-type variations are thought to arise from a large increase in accretion caused by a large-scale disc instability (e.g., Reipurth et al. 2007a).

Most of these mechanisms have been widely studied through optical monitoring campaigns (see Grankin et al. 2007, 2008, and references therein). However, the mechanisms causing optical variability in YSOs are also thought to be responsible for the occurrence of photometric variations in the near-IR (Skrutskie et al. 1996), especially suitable for probing phenomena which take place in the circumstellar temperature regime (see Eiroa et al. 2002, and references therein). Furthermore, in most of the young clusters (few Myr old), much of the interesting population remains visibly obscured, and must be studied with IR observations. However, obtaining multi-epoch data over full star forming regions has been until recently impossible, with young clusters extending over degree scales on sky and IR cameras usually having fields of only arc minutes. This has changed with the Two Micron All Sky Survey (hereafter, 2MASS, Cutri et al. 2003), which uniformly scanned the entire sky in the near-IR using two automated 1.3 meter telescopes, allowing for the first time large area, though rather shallow, observations to be made, and near-IR variability studies to become possible (Carpenter et al. 2001, 2002). In a 2MASS JHK_s study centred near the Trapezium region of the Orion Nebula Cluster, where most star formation is thought to have occurred between 0.3 and 2 Myr ago (Ali & Depoy 1995; Hillenbrand 1997), Carpenter et al. (2001) found that approximately 45% of the young stars were variable. Furthermore, Kaas (1999) has shown that IR variability is a very useful tool for sorting the cluster population from the background field. For instance, it has the advantage of identifying young sources that do not show IR-excess or have small Hα

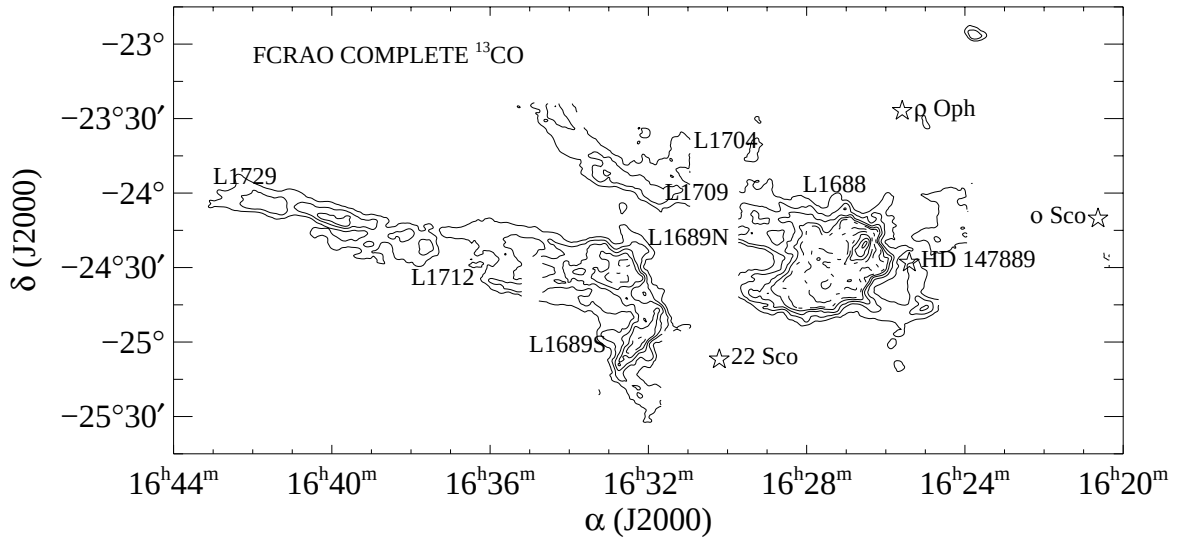

Figure 1.5: ^{13}CO integrated intensity maps of the ρ Ophiuchi region from the COMPLETE Survey of Star-forming Regions (Ridge et al. 2006)

emission, as is the case for weak-line T Tauri stars (WTTS), but are magnetically active (Grankin et al. 2008). The use of this relatively new technique should contribute significantly to obtaining a full census of the young objects in star formation regions, one of the most important goals of galactic star formation studies.

1.4 ρ Ophiuchi Molecular Cloud

At a distance of 119 $\pm$ 6 pc (Lombardi et al. 2008), the ρ Ophiuchi cloud core is one of the nearest star forming regions, and therefore widely studied (see review by Wilking et al. 2008, and references therein). Despite the proximity, few stars are optically observable due to the high visual extinction in the core, estimated to be 50-100 magnitudes (Wilking & Lada 1983). The ρ Ophiuchi cloud complex contains the main cloud, L1688, and two streams, L1709 to the northeast and L1689 to the southeast, which have been mapped in extinction by Cambrésy (1999) and more recently in ^{13}CO integrated intensity maps (see Fig. 1.5) by the COMPLETE Survey of Star-forming Regions (Ridge et al. 2006).

Vrba (1977) was the first to propose that star formation in the ρ Ophiuchi main cloud was related to that of the larger Sco-Cen OB association. This theory was later revisited by de Geus (1992) who studied the relation between large scale HI structures and the subgroups of the Sco-Cen association, showing evidence for the presence of a

slow shock in the Ophiuchus/Upper-Scorpius regions, which they claim is likely to have been caused by the collision of the expanding shell of one of the Sco-Cen subgroups and the original cloud of gas from Ophiuchus. The authors go on to suggest that the runaway star η Oph (Blaauw 1961) could be interpreted as being, in the past, part of a binary where the other companion's death as a supernova event $\sim$1 to 1.5 Myr ago, would have triggered the observed shell and ultimately star formation in Ophiuchus. This would be consistent with an age of $\sim$0.3 Myr which has been determined for the stars in the core of Ophiuchus (Greene & Meyer 1995; Luhman & Rieke 1999). However, independent spectroscopy studies from YSOs over a more dispersed region of the sky surrounding the ρ Ophiuchi's core (Bouvier & Appenzeller 1992; Martin et al. 1998; Wilking et al. 2005), derived a median age of 2 Myr for this more distributed population. Wilking et al. (2005) suggested this population formed contemporaneously with the low mass stars in the Upper Scorpius subgroup, where star formation is thought to have been triggered by an expanding shell from the Upper Centaurus Lupus OB subgroup.

In the last decade, ρ Ophiuchi has been intensively targeted by several new instruments, specially in the X-rays (Rosat, Chandra, XMM-Newton) and the IR (ISO, 2MASS, Spitzer, and now with the WFCAM). The result of the combination of the first studies of Ophiuchus with these new datasets from the most advanced instruments is a total population of $\sim$300 members of this star forming region, as recently compiled by Wilking et al. (2008) and which will be discussed in more detail in Sect. 3.2.

1.5 Aims and Outline

This thesis aims to advance our current knowledge of formation and evolution of young stellar objects. In particular, it will try to provide a coherent answer to the questions: How frequent is photometric variability in young stars? What are the underlying processes causing photometric variability and what can they tells us about the ongoing physics in individual pre-main-sequence stars and brown-dwarfs? What can we learn about disc environments from IR photometric variability, usually not accessible to optical surveys? And finally, can variability surveys be used to uncover new young stellar objects and provide a more complete census of star-forming regions?

To answer these questions, this dissertation uses data from one of today's most advanced IR imaging camera, the Wide Field Camera (WFCAM) at the United Kingdom Infrared Telescope (UKIRT) (Casali et al. 2007). The large field of view ($\sim$0.8 deg^2 in four exposures) of this instrument has made deep variability studies possible for the first time in the IR. Figure 1.6 compares an optical image of the ρ Ophiuchi cluster (Digital Sky Survey) to the IR image taken with the WFCAM in the K-band. Using the IR regime, is possible to penetrate into the cloud and study the embedded stel-

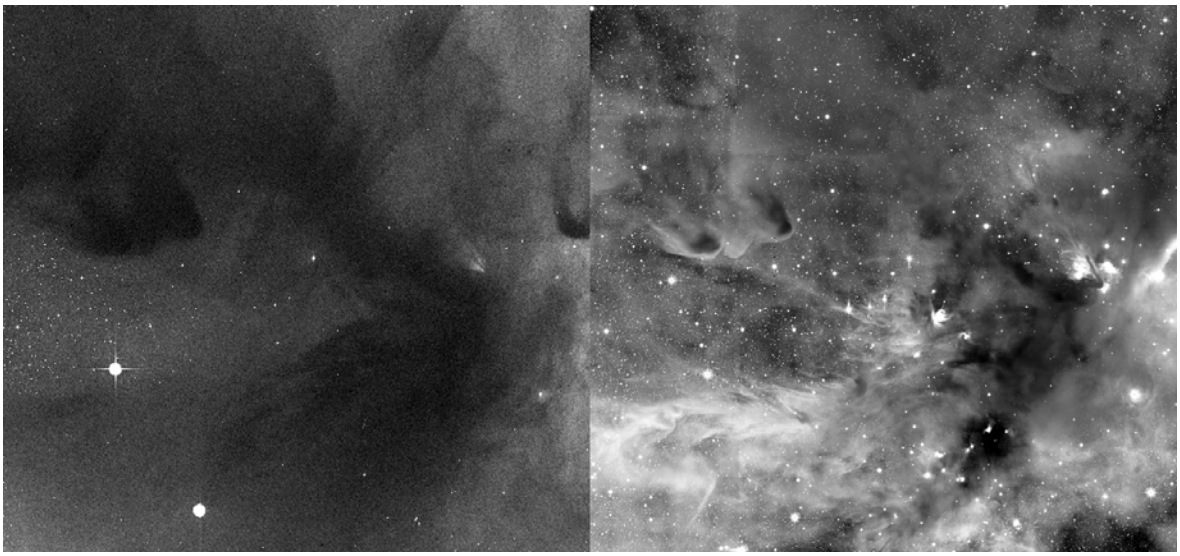

Figure 1.6: The image on the left shows an optical view of the ρ Ophiuchi cluster. The same area is shown on the right in infrared wavelength. Infrared observations can penetrate the obscuring cloud to reveal new details.

lar population of this cluster. This thesis presents the results of such a study, with multi-epoch H (1.63 μm) and K (2.20 μm) band observations of the ρ Ophiuchi cluster used to search for variability on timescales of days, months, and years. The study is enhanced by including recently released IRAC and MIPS/Spitzer data on ρ Ophiuchi (Evans et al. 2008). In Chapter 2, the observations and reductions for the large data sample are described. Chapter 3 explains the methods used in the search for variability together with the results of the analysis. These are discussed and explained in a physical context in an attempt to relate the variability behaviours observed to the possible physical causes. In Chapter 4, the spectroscopic follow-up that has been conducted with the low-resolution spectrograph *Son of Isaac* (SofI) at the New Technology Telescope (NTT), and the first results of the analysis and membership classification are presented. Chapter 5 presents the work conducted during the construction and commissioning of the new IR imaging camera of the European Southern Observatory (ESO), HAWK-I (High-Acuity Wide-field K-band Imager), where the author's contribution to the project is presented, as well as an up to date status of the instrument, now being offered to the community. Finally, Chapter 6, describes work in progress for a project which concerns the combination of all the WFCAM data into a single, very deep, near-IR image to look for very faint, low-mass members of ρ Ophiuchus. Conclusions and future prospects are given in Chapter 7.

Part of the results presented in this thesis have been published in the journal Astronomy & Astrophysics, (Alves de Oliveira & Casali 2008), but here the data reduction is presented in detail, recent data releases are used, and also a more extended analysis

of the dataset is provided. The spectroscopy data presented in this thesis will also be published in an article which is in preparation, more details are given in Chapter 4. The results presented in Chapter 5 are partially presented in Kissler-Patig et al. (2008b), but here put in the full context of the HAWK-I instrument science case and current use of the instrument. Unless clearly stated otherwise, all the work presented has been done by the author of this thesis, within a 3 year period (including the writing of this thesis).

Chapter 2

Photometric survey: observations and reductions

The core data for this thesis was obtained with a new near-IR imager, the Wide Field Camera (hereafter WFCAM) on the United Kingdom Infrared Telescope (UKIRT) (Casali et al. 2007), which started to operate in 2005, making this project one of the first scientific returns for the instrument. In this chapter, I will describe the observational equipment and methods used for the observations, as well as the associated sources of error. One of the biggest challenges in the treatment of the data, was to ensure catalogues which contained reliable photometry, and were not contaminated by artifacts. That allows the large dataset to be used in an automated way to search for intrinsic photometric variations in the brightness of stars.

2.1 Near-IR photometry: WFCAM/UKIRT

The WFCAM/UKIRT (Casali et al. 2007) is the survey instrument developed by the UK Astronomical Technology Centre (UK ATC) primarily for the UKIRT Infrared Deep Sky Survey (UKIDSS) (Lawrence et al. 2007). UKIRT is an infrared dedicated 3.8m classical cassegrain telescope and it has been operating on the summit of Mauna Kea, Hawaii, since 1979. At the moment, it operates both as a survey instrument, for the UKIDSS survey, and an open access telescope. The WFCAM is schedule for 60% of UKIRT time. It was mounted for the first time in the UKIRT telescope in October 2004 and after a commissioning phase it started to fully operate in May 2005.

WFCAM is a wide field imaging camera operating in the near infrared from 0.83 μm to 2.37 μm in up to eight filters, including *ZY JHK* (Hewett et al. 2006). The camera uses four Rockwell Hawaii-II 2048 x 2048 18 μm-pixel array detectors with a pixel scale of 0.4" which was chosen to maximize the survey speed. The Hawaii-II has four independent quadrants each of which is further divided into eight channels of 128 x 1024 pixels and rotated 90° with respect to its neighbour. The four detectors are arranged

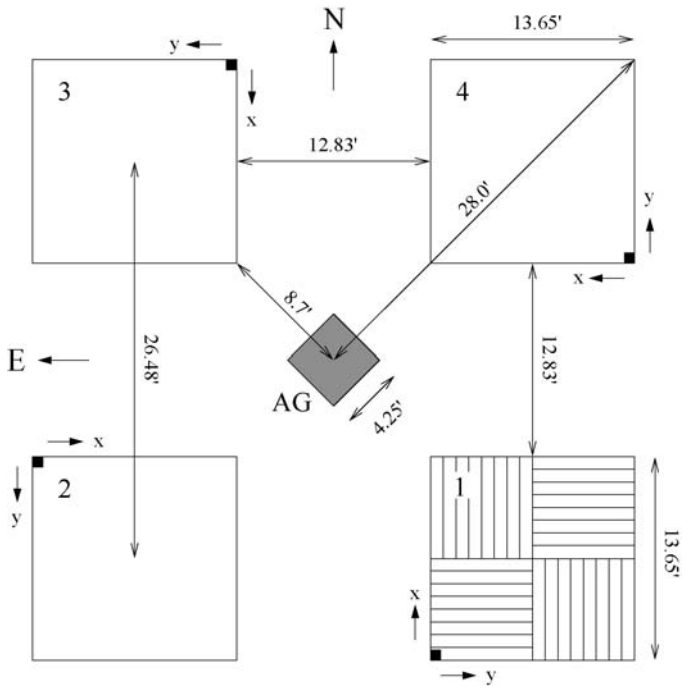

Figure 2.1: WFCAM focal plane. The four detectors are shown, with the autoguider placed at the centre of the focal plane. The detectors are separated by 94% of a detector width.

in a 2 x 2 pattern and are separated by 94% of a detector width, so four exposures are needed to survey a contiguous area of $\sim$0.8 deg^2. An autoguider CCD is located at the centre of the focal plane. The layout of the focal plane is shown in Fig. 2.1.

2.1.1 Observations of the ρ Ophiuchi Cluster

The WFCAM observations for this project were obtained via guaranteed time, awarded to the project scientist (M. Casali). The correlated double sampling (CDS) acquisition read mode was used in which an initial read is made after resetting a detector, followed by an exposure which is set according to the appropriate band, terminated with a final read. The difference between the two reads is then the output. All data were collected in H and K bands with an exposure time of 2s and 5s, respectively. Fourteen spatially offset (jittered) integrations were taken per telescope pointing in each filter, each with 8 exposures. These sum up to a total exposure time of $\sim$9.3 minutes in H, and $\sim$5.6 minutes in K. The use of this observing strategy is common when dealing with IR detectors, where long exposures are split into a sequence of many shorter ones with different spatial offsets, which will then be flatfielded, shifted, and co-added to produce the final image. This is done to remove the effects of bad pixels (common in IR detectors) and also to avoid saturation by the sky background which is much

Table 2.1: Coordinates of the observations.

Pointing	RA	Dec.
1	16 27 20.0	−24 19 20
2	16 27 20.0	−24 32 34
3	16 28 18.2	−24 29 00
4	16 28 18.2	−24 15 48

Table 2.2: Log of the observations.

UT date	May	June	July
2005	11, 18, 21, 29	04, 07, 14	...
2006	24, 28[a]	03, 14, 23	04, 10

[a]Observations taken only for H band.

brighter than, for example, in the optical.

The nominal region consists of four pointings which produce a final tile of $\sim$0.8 deg^2. Table 2.1 shows the central position (right ascension and declination) for each of the four pointings (see Fig. 2.2). The scheduling of the observations was primarily dictated by the fact that ρ Ophiuchi can only be observed in the summer period (both in the North and South hemisphere). As mentioned in the previous chapter, variability in young stars is seen to occur in various timescales, so the planning of the observations was done in a way which would allow the examination of variability on different timescales from days to years. A roughly random sequence of epochs was chosen to do this, partly determined by telescope scheduling constraints. Table 2.2 provides a list of the nights in which the observations occurred. The same region in the sky was observed in a total of 14 nights, and the dates when the observations were taken made possible to study near-IR photometric variability characteristics on times scales of $\sim$1 - 30 days, $\sim$2 - 3 months, and $\sim$1 year.

2.1.2 Errors Associated with Observations

Given the expected very low amplitudes of variation in young stars, a few tenths or less of a magnitude in the near-IR (Carpenter et al. 2001), it is important to be aware of common problems intrinsic to the instrument and type of observations, which might introduce errors of this order. To a large extent, many of these problems were eliminated by the software pipeline during reduction and calibration. However, others do persist giving rise to false detections which show up in the catalogues. Although they represent a small fraction of the dataset, they need to be filtered out (see Sect. 2.1.3) since only a small fraction of point source detections are expected to be variable.

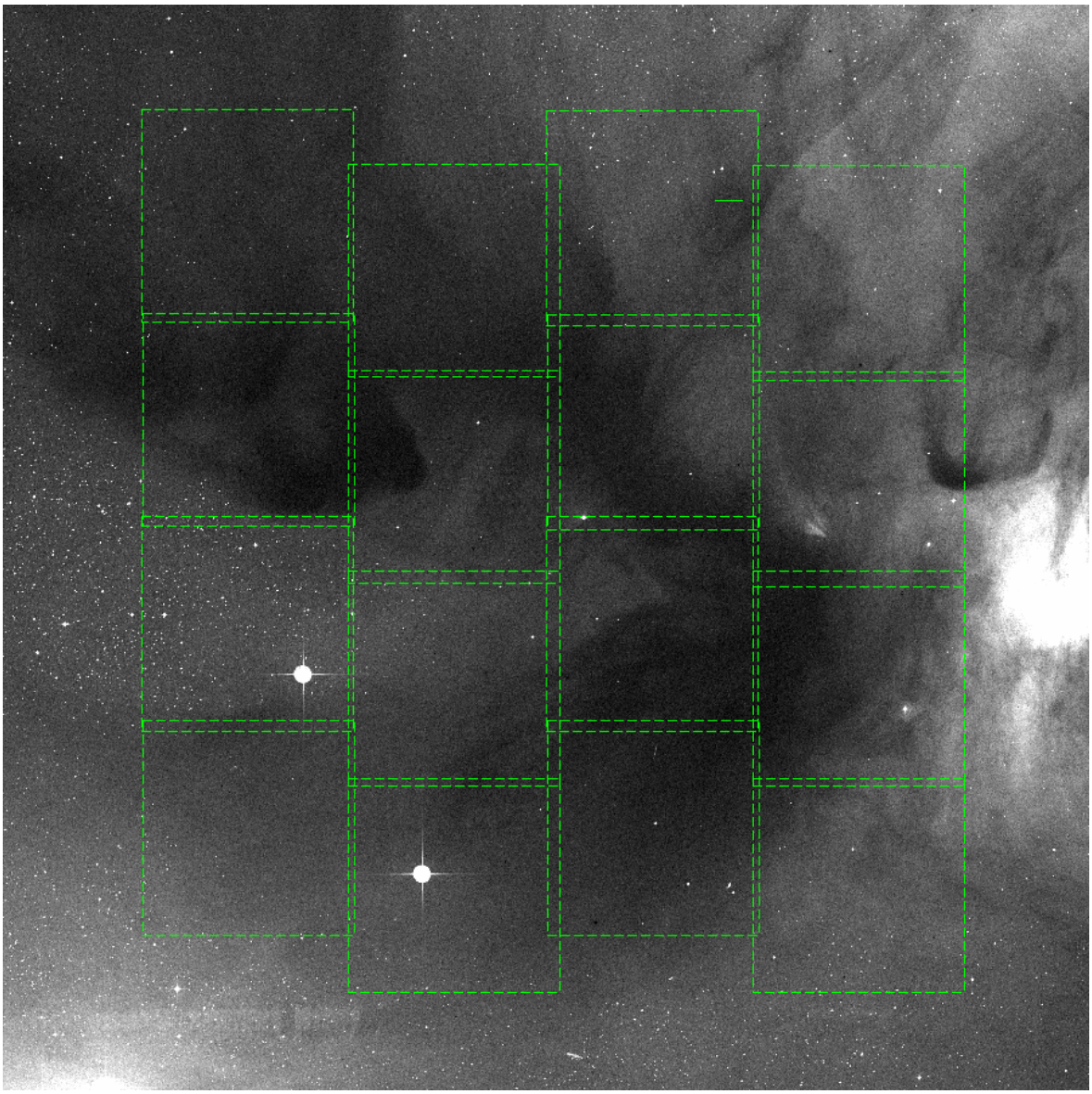

Figure 2.2: WFCAM coverage of the ρ Ophiuchi Cluster. The WFCAM field of view is seen overlaid on an optical image of the Ophiuchus molecular cloud (Digital Sky Survey). The dark cloud region where star formation is occurring can clearly be seen. Coordinates of each pointing are given in Table 2.1. The nomimal area covered with 4 pointings is $\sim$0.8 deg^2.

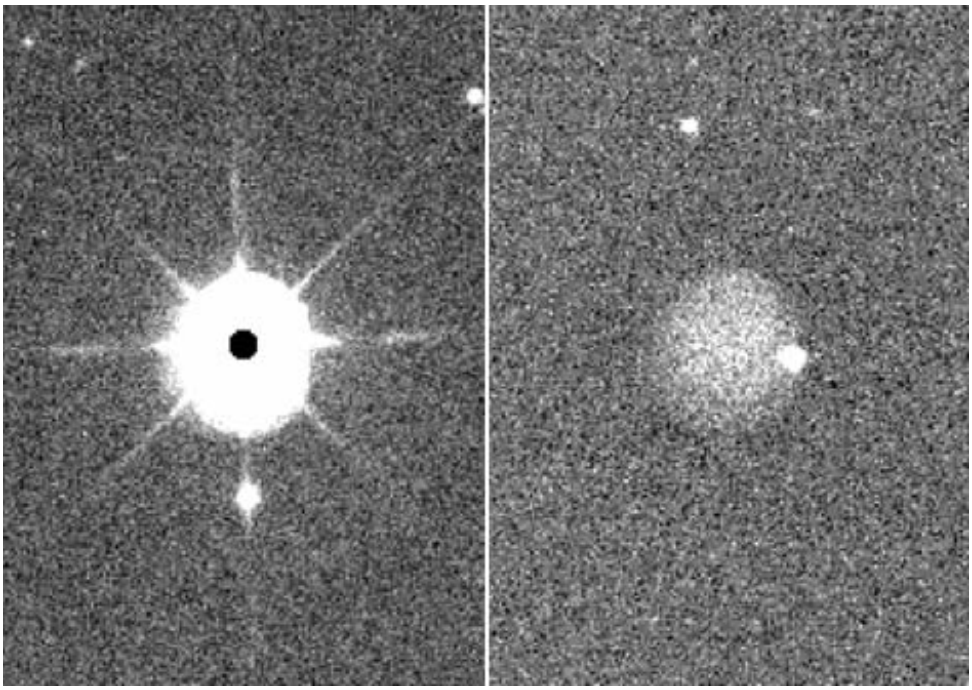

Figure 2.3: Example of *persistence* (Irwin et al. 2008), an artifact that is common to IR detectors and present in the WFCAM images. The image on the left-hand-side shows a 10s H-band exposure of a bright (6th magnitude), saturated star, whereas on the image on the right-hand-side is an exposure of a different part of the sky taken 15s later which shows a false source, caused by the previous image.

One of the causes of artifacts is persistence, which occurs when the charge from a bright source is not completely removed after a detector reset, causing the appearance of a false source in the following exposure (see Fig. 2.3). The brightness of the persistence image depends on the source count rate, filter and number of resets and its size is typically that of the saturated part of the parental image. Another form of persistence occurs for the first frame after a filter change because the detector is exposed to unfiltered light and saturates.

Another problem caused by bright sources is that of cross-talk between the detector channels within a quadrant, which produces a sequence of spurious images in some or all the other 7 channels. These images always appear offset across the channel width by an integer multiple of 128 pixels, and the number of appearances depends on the number of counts of the bright star. These spurious sources appear in the same location relative to the bright star for all the filters and as such they show up as real entries in the catalogue. They are due to capacitive coupling between channel circuits on the detector chip, hence they appear as the derivative of the parent image. A diagram explaining this effect is shown in Fig. 2.4.

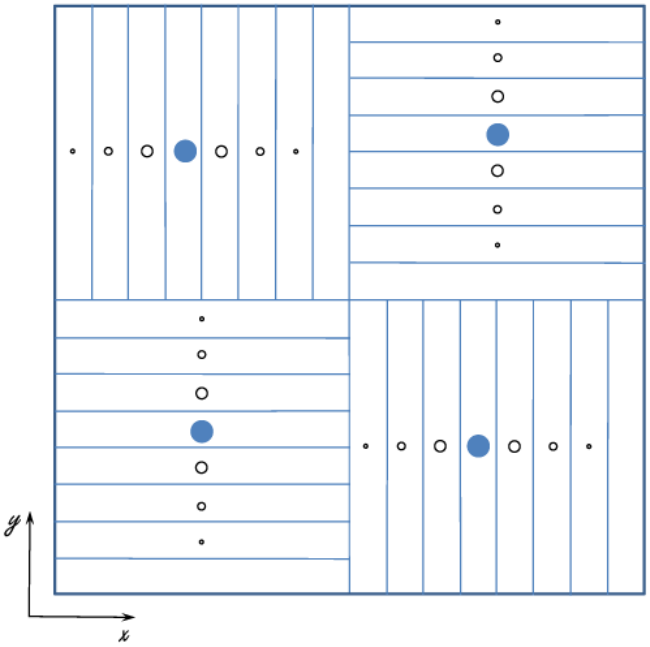

Figure 2.4: Artifacts in WFCAM images: cross-talk. Bright stars cause cross-talk between detector channels which appear in the images as the derivative of the parent image.

Bright sources also cause the appearance of a diffraction pattern, which shows up as eight spikes around the bright star (Fig. 2.5). Four diffraction spikes arise from the spider holding the telescope secondary mirror, and four from the spider holding the focal plane in the instrument which is rotated 45° with respect to the secondary mirror spider. Spurious sources occur in lines along these diffraction spikes, and the detection algorithm often identifies these as real sources which then are included in the catalogue (see Sect. 2.1.3). Furthermore, stars which fall in the spikes or in the surrounding area are likely not to have reliable photometry.

Finally, cosmic rays that hit the detector during the observations will also appear in the detections catalogues. This effect did not have to be accounted for since with time-series photometry these detections are automatically eliminated once several nights are merged, given the very low probability that such an event occurs exactly in the same detector pixels. However, it could still affect the photometry of a star for a single night, for which a final eye-inspection of the images is always desirable, and has been performed.

WFCAM observers have also reported other artifacts in the images. In some frames the counts for some channel may be offset high or low by a few counts. This effect happens preferentially for shorter wavelength filters given the lower sky counts. The offset

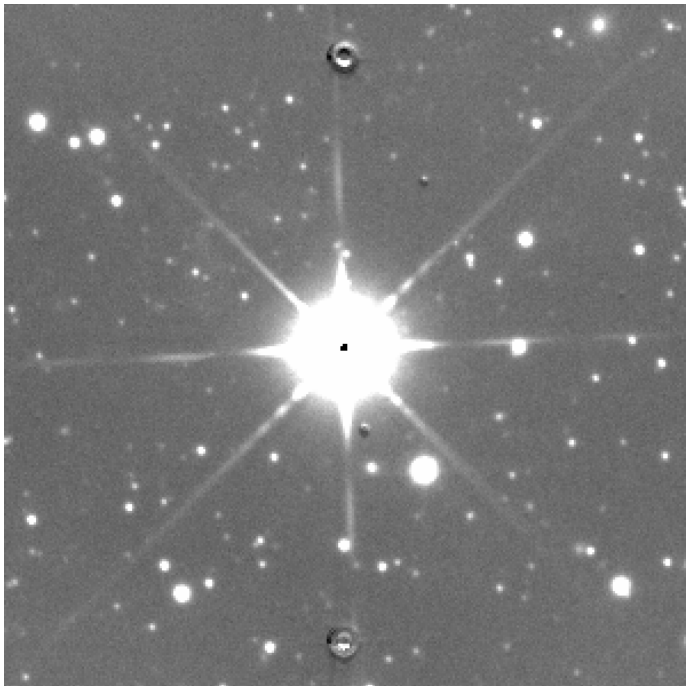

Figure 2.5: WFCAM images show a diffraction pattern for bright stars. Spurious source detection occurs in the lines along the eight spikes. In the top and bottom part of the image, the cross-talk effect can be seen, which shows up as *donnut-shape* artifact.

can vary from one frame to the next which means it does not get removed by subtraction of a dark frame. In the worst cases, the bias offsets confuse the object detection algorithm resulting in a large number of spurious sources in the channel. Other undesirable effects are the bright moon ghosts, false images which appear when the moon is shinning directly onto the field lens near the top of the telescope. The appearance of the ghosts depends on the angle of inclination of the moon relative to the optical axis. However, none of these effects has been seen in the WFCAM data for this thesis project.

Some of the sources of error presented can be eliminated, or their effects in the data minimized, during the observations, and also by performing careful maintenance of the instrumentation. However, others are intrinsic to the instrument and type of observations and can only be handled *a posteriori* in the catalogue. The next section will give an insight into the reduction process and also presents the criteria applied afterwards in order to remove as much as possible the spurious entries from the final source list and ensure the reliability of the dataset for this project.

2.1.3 Reductions

WFCAM data are processed and archived by the VISTA Data Flow System Project, a collaboration between Queen Mary University of London, the Institute of Astronomy of the University of Cambridge and the Institute for Astronomy of the University of Edinburgh (Irwin et al. 2008). The pipeline flat-fields the data, subtracts the counts from the background sky, detects and parameterises objects, and performs the photometric and astrometric calibrations. The products from the pipeline are a set of reduced uncalibrated individual exposures, and photometrically and astrometrically calibrated stacked frames, as well as catalogues of sources detected in the frames and ingested into the WFCAM Science Archive, described by Hambly et al. (2008). Below follows a brief explanation of the pipeline processes and the calibrations, as well as a listing of the steps taken afterwards to 'clean' the catalogue from spurious sources.

Pipeline Processing

In the pipeline, data files are divided into three categories: science frames, twilight flatfields and darks. The first pipeline step is to create a master dark which is then subtracted from all the frames. The main effect of dark subtraction is the removal of the majority of the "reset anomaly", an additive component related to the decaying capacitative behaviour of the detector and the time delay between the reset and the first read. In this step also hot pixels are removed. Next, the master twilight flat is applied for the respective filter. The final step is to make a stack or leavestack frame by weighted averaging. The weights are obtained from the confidence map which is derived mainly from the flatfield, with a zero confidence given to dead pixels, pixels with poor sensitivity and pixels with unpredictable levels. Once this process has been completed, a source extraction routine is run (Irwin 1985) in which sources are defined when four or more connected pixels all lie more than 1.5σ above the local background sky level. A global background algorithm is used to track the varying sky level over each frame. For each detected object a set of parameters is measured, for example, the celestial coordinates in the World Coordinate System (WCS), the flux measured for different apertures, a flag indicating the most probable morphological classification (point source versus extended source), among others.

Post-pipeline: Removal of Artifacts

The pipeline catalogue has many false detections and problems as outlined in Sect. 2.1.2. A routine was written in IDL[1] to implement an algorithm which finds and removes spurious sources and implements the necessary constraints to ensure a reliable final source list. Figure 2.6 shows a $\sim$100 x 100 arcsec^2 cut of a WFCAM image of ρ Ophiuchus,

[1]IDL (Interactive Data Language) is a programming language ideal for processing large amounts of data.

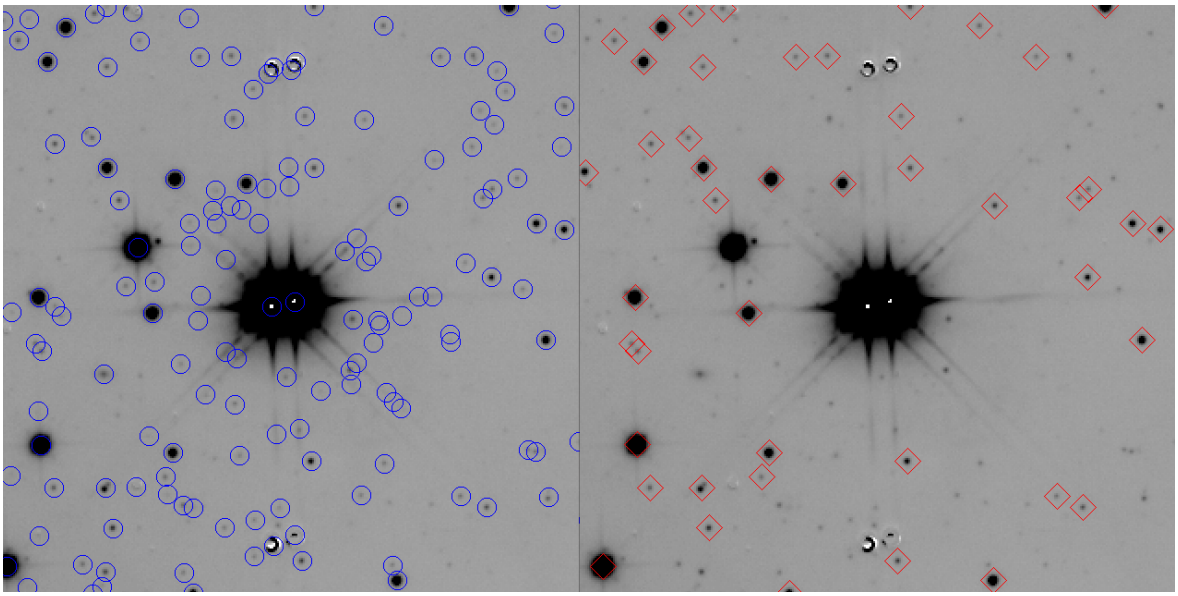

Figure 2.6: Removal of artifacts in WFCAM images. The figure shows a ∼100 x 100 arcsec^2 cut of a WFCAM image of ρ Ophiuchi. On the image on the left-hand-side, the original detections catalogue is overlaid showing many false detections. On the right-hand-side, the final catalogue after the algorithm has been implemented is overlaid on the image, showing the removal of artifacts.

where the original detections catalogue is shown (left-hand-side) in comparison to the final catalogue (right-hand-side), after the algorithm to remove artifacts has been applied, showing that the instrumental artifacts mentioned above have been efficiently removed in an automated way. The main features of the algorithm are briefly explained below.

- Overlapping regions and detector edges: the algorithm accounted for sources in the overlapping regions between detectors which have multiple entries in the catalogue, keeping the parameters of the source with the largest distance to the detector edge, since the electronic noise increases towards the detector edges. Furthermore, sources that lay within the jitter offset of the frame boundary have missing information, since not all component images are present in the final stack. In the regions where the detectors overlap, a safety margin of 20 pixels was applied, and no source detections that fell in this region were included in the final catalogues. For sources located on the outer field edges of the full mosaic, since there is no overlap with other frames, a more conservative margin of 100 pixels was applied, since the shifts from the reference position are usually <30 arcsec, i.e. ∼75 pixels.

- Magnitude limits: sets a cut-off limit at the brighter end (magnitudes 11.0 and

Table 2.3: Photometric accuracy.

Magnitude	Photometric Accuracy	
	H	K
10-11	...	0.01
11-12	0.01	0.01
12-13	0.01	0.01
13-14	0.01	0.01
14-15	0.01	0.01
15-16	0.01	0.02
16-17	0.02	0.05
17-18	0.04	0.07
18-19	0.05	...

10.0 for H and K, respectively) due to saturation. At the fainter end, the limiting magnitudes of the images were measured using a number count histogram. The magnitudes of all the objects were sorted into a histogram. The peak value of the histogram, where the number counts start to turn over, was used as a rough measure of the limiting magnitude of the image. In the WFCAM data, magnitudes 19.0 and 18.0 for H and K, respectively, mark the completeness limits which are above the 10σ level (see Table 2.3 for the average errors).

- Object classification: objects flagged by the pipeline as 'star' were kept, while source detections flagged as 'galaxy' were rejected. However, for source detections with magnitudes brighter than $H<18.0$ and $K<17.0$, objects which were classified as galaxies but showed a difference <0.1 in magnitude between different apertures were included. The motivation was to include some nebulous YSOs misclassified as galaxies, while setting the criteria strictly enough to avoid galaxy contamination.

- Cross-talk: electronic cross-talk occurs between the detector channels within a quadrant. It produces a sequence of spurious images in some or all the other 7 channels. The algorithm removed sources located at up to seven multiples of 128 pixels from bright stars (see Sect. 2.1.2), which is the maximum number of remaining channels that can be affected within a quadrant.

- Diffraction patterns: sources in the surroundings of saturated stars were removed since their photometry is not reliable (see Sect. 2.1.2). The radius of rejection was adjusted according to the brightness of the star. However, since most of the bright stars for which this effect occurs are saturated in the WFCAM images, their magnitudes could not be used in defining the influence radii of the diffraction spikes. Therefore, the WFCAM catalogues were merged with 2MASS catalogues from the All-Sky Survey (Cutri et al. 2003), which saturates at much brighter

magnitudes than WFCAM using a matching radius of 1". A visual inspection of the images was done to derive the approximate extent of the diffraction spikes per magnitude range of the bright stars. According to this evaluation, the rejection radii were defined as 20, 30, and 36 pixels for stars with magnitudes (from the 2MASS catalogues) of $9 < H < 11$ or $8 < K < 10$, $7.5 < H < 9$ or $6.5 < K < 8$, and $H < 7.5$ or $K < 6.5$, respectively.

Furthermore, the K band images from the observations made on 28 May 2006 were discarded since they were of lower quality due to technical problems.

The source catalogues for each night were merged for the two years separately. Sources were matched by requiring their position to be within an angular separation of 1.0", since the normal position errors found range from 0.1" to 0.8". It was further required that each source have at least four epochs with detections in each filter. This criterion was implemented in order to reduce the probability of false transient detections and to reduce the effects of close double stars which are not resolved in all the nights, depending on seeing conditions. In total, ∼16 000 sources were considered detected across the two years of observations.

The photometric calibration of WFCAM data is critical for a variability study and was done with 2MASS stars in the observed frames as part of the nominal pipeline reduction. However, some of these stars could be variable, which would have an impact on the calibration. Furthermore, for regions in the sky with high extinction, as is the case for the central core of ρ Ophiuchi, the number of available 2MASS stars is reduced, which limits the photometric accuracy. Lastly, photometric offsets can also arise from small problems in flatfielding and sky subtraction from night to night. For these reasons, the internal accuracy of the photometry was further improved by a procedure to remove any offsets between nights. This was done separately per detector and for each of the four sky pointings. Stars with magnitudes between 12.0 and 16.0 for K-band and 13.0 to 17.0 in H-band were used for the calculations, assuming that their median magnitudes do not change in time. This method should be reliable because the vast majority of the thousands of sources used in the calculation are background stars. Even if some of these are variables they will of course be uncorrelated, and the median should be robust to very high precision. The final offset for one detector at a given sky pointing was taken to be the average value of the differences in magnitude between the several nights and a reference night. This offset value, up to 0.03 magnitudes, was then removed from all the sources detected in that particular detector and sky pointing.

2.1.4 Observations of the Orion Nebula Cluster

WFCAM observations of the Orion Nebula Cluster (ONC) were also obtained via guaranteed time, in the same manner as the Ophiuchus data, i.e., H and K bands with

Table 2.4: Coordinates of the observations.

Pointing	RA	Dec.
1	05 35 47.0	−05 17 58
2	05 34 53.7	−05 17 58
3	05 34 53.7	−05 31 14
4	05 35 47.0	−05 31 14

Table 2.5: Log of the ONC observations.

UT date	October	November	December	January
2005	27	13, 14, 30	04, 10, 30	...
2006	...	24, 28	07, 22	...
2007	...	...	...	13, 21

an exposure time of 2s and 5s, respectively (8 exposures per integration, each with 14 jitters). The observed region consists of four exposures, for which the central position (right ascension and declination) are shown in Table 2.4 (see Fig. 2.7). Table 2.5 provides a list of the nights in which the observations occurred. The observations of the ONC amount to a total of 13 nights.

Several problems arose, however, in the reduction of these images. The ONC star forming regions have large amounts of extended reflection nebulosity. The main problem is that the current WFCAM pipeline reduction employs a sky frame derived from the median filtering of the jittered images. This effectively removes low spatial frequency nebular structure, but leaves high spatial frequency nebulosity on scales smaller than the jitter scale (typically <30 arcsec), still compromising any attempt to extract reliable photometry in such a complex region. The solution is to reduce the images using good skyframes taken during the same nights when the observations have been conducted. However, this could not be handled, up to now, in an automated way by the pipeline. Once this problem is solved, this dataset will be used for a variability study analogous to the one presented in this thesis for the ONC, and also in a joint project with the Institute for Astronomy at the University of Hawaii to construct the deepest colour-colour diagram ever of the ONC. However, the Orion data will not be discussed further in this thesis.

2.2 Mid-IR photometry: IRAC and MIPS/Spitzer

The Spitzer Space Telescope[2] was launched into space in 2003 and is the final mission of NASA's Great Observatories Program, which has already launched other three space

[2]http://www.spitzer.caltech.edu/

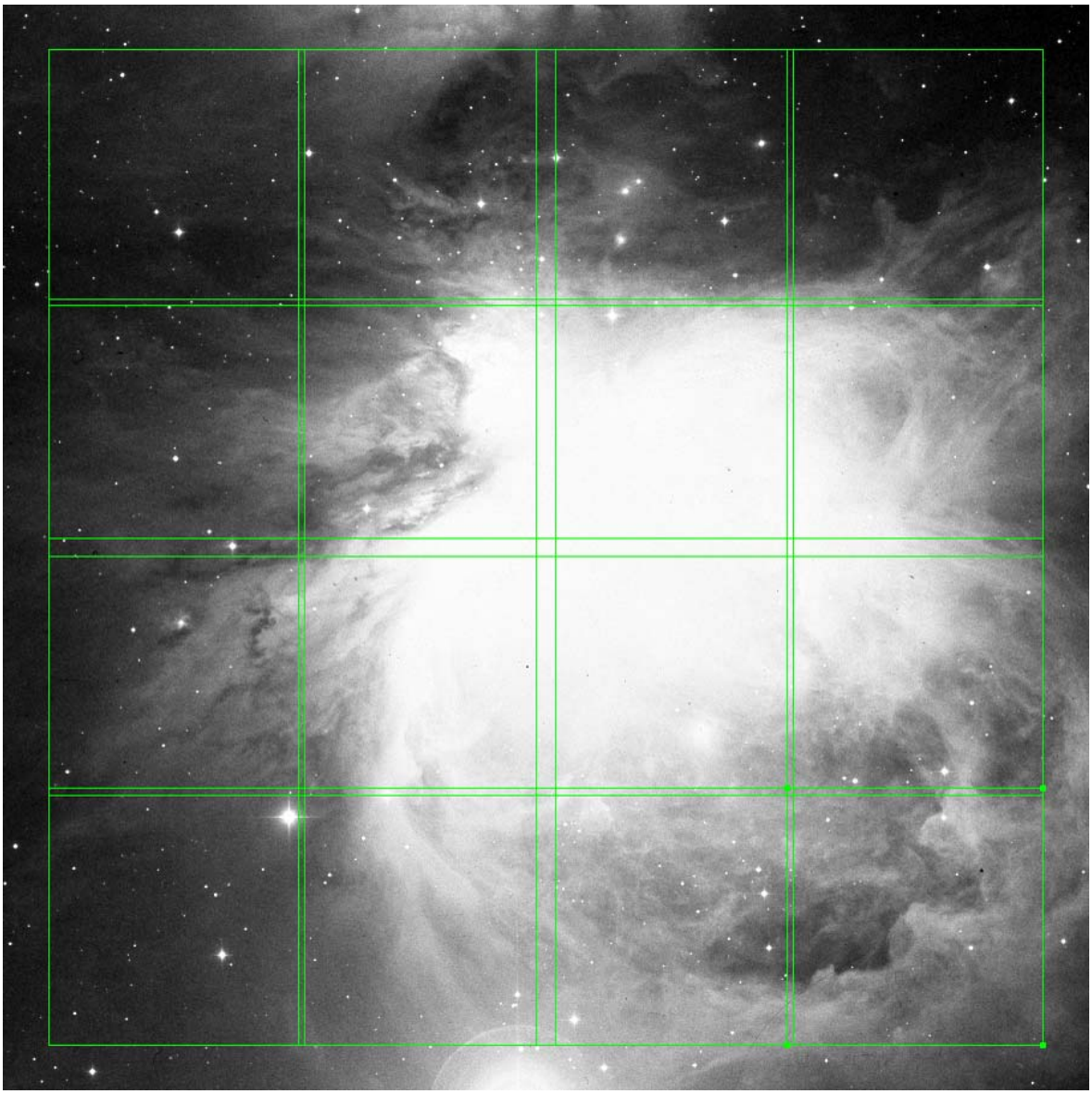

Figure 2.7: WFCAM field of view, overlaid in an optical image of the Orion Nebula Cluster (Digital Sky Survey).

telescopes, namely the Hubble Space Telescope (HST), the Compton Gamma-Ray Observatory (CGRO), and the Chandra X-Ray Observatory(CXO). It is equipped with three instruments, the Infrared Array Camera (IRAC) operating from 3.6 to 8 μm (Fazio et al. 1998), the Multiband Imaging Photometer (MIPS) operating from 24 to 160 μm (Engelbracht et al. 2000), and the Infrared Spectrograph (IRS) operating from 5.3 to 40 μm (Houck et al. 2000). Spitzer is a 0.85 meter telescope, and the largest IR space telescope to date. The telescope is cooled to cryogenic temperatures (-273 °C) and placed in an heliocentric orbit chosen to be far enough away from the Earth to allow the telescope to cool more efficiently, saving large amounts of coolant, and reducing the cost of the mission (Gallagher et al. 2003).

2.2.1 c2d enhanced products

Part of Spitzer's observing time is reserved for the Spitzer Legacy Science Program, which contains a few large science projects with the objective of creating substantial databases for different research fields, which are made available to the public immediately after the data processing and validation have been done by the Spitzer Science Centre (SSC). One of the Legacy programs is "From Molecular Cores to Planet-forming Disks" lead by N. Evans (Evans et al. 2003), commonly refereed to as "Cores to Disks" (c2d), which uses 400 hours of IRAC and MIPS observations to study the star and planet formation at different evolutionary phases. ρ Ophiuchi is one of the five nearby molecular clouds observed in this program, and the region surveyed is shown in Fig. 2.8.

To complement the WFCAM study, Spitzer data from the c2d Legacy program have been included in the analysis. The Ophiuchus molecular cloud has been mapped with IRAC (Fazio et al. 2004) in the 3.6, 4.5, 5.8 and 8.0 μm bands, over a region of 8.0 deg^2, which encompasses the entire WFCAM field. The area mapped with MIPS extends over 13.8 deg^2 of the Ophiuchus cloud and overlaps with the IRAC survey (Padgett et al. 2008) (see Fig. 2.9). The final delivery of IRAC and MIPS data from c2d Legacy team was made available in late 2007 (Evans et al. 2008). Alves de Oliveira & Casali (2008) made use of an earlier version of these data products (third data delivery, DR3, Evans et al. 2005), but in this thesis the recommendations from the c2d team are taken, and the new products from the final delivery are used in the analysis. Several improvements in the delivered data have been reported by Evans et al. (2008), such as photometric corrections for IRAC data, deeper level of extracted sources in the MIPS observations, and the inclusion of 70 μm data.

Spitzer counterparts were obtained from the c2d IRAC and MIPS point-source catalogues using a search radius of 2". To ensure a reliable sample, only non-extended sources are considered, as estimated by the source extraction, and the flags for the quality of detection provided in the catalogues, which are assigned based on the signal-to-noise of the detection, are taken into account. Only detections with quality flag A

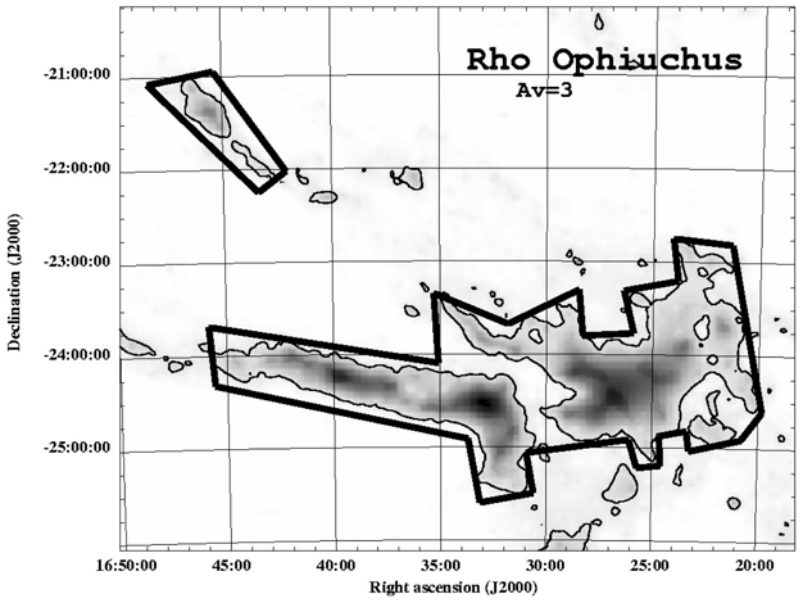

Figure 2.8: c2d observations of ρ Ophiuchus are marked out (Evans et al. 2003) and surround the $A_V = 3$ contours from Cambrésy (1999).

Figure 2.9: Spitzer image of the ρ Ophiuchus molecular cloud combining IRAC and MIPS data (RA from ∼16:20:00 to 16:35:00, and Dec. from -23:00:00 to -25:00:00). Blue colour shows light at 3.6 μm, green at 8 μm, and red at 24 μm. The extended nebula is caused by its dust being heated by nearby bright young stars. Credits: NASA / JPL-Caltech.

(S/N $\geq$ 7), B (S/N $\geq$ 5), or C (S/N $\geq$ 3) are considered. Spitzer fluxes were converted to magnitudes using the IRAC zero-magnitude flux densities of (Reach et al. 2005) and the MIPS zero-points from (Rieke et al. 2008), in the following manner:

$$IRAC\ 1\ (3.6\ \mu\ m) : [3.6]_{mag} = -2.5 * log_{10}\frac{280.9}{Flux_{3.6}} \tag{2.1}$$

$$IRAC\ 2\ (4.5\ \mu\ m) : [4.5]_{mag} = -2.5 * log_{10}\frac{179.7}{Flux_{4.5}} \tag{2.2}$$

$$IRAC\ 3\ (5.8\ \mu\ m) : [5.8]_{mag} = -2.5 * log_{10}\frac{115.0}{Flux_{5.8}} \tag{2.3}$$

$$IRAC\ 4\ (8.0\ \mu\ m) : [8.0]_{mag} = -2.5 * log_{10}\frac{64.13}{Flux_{8.0}} \tag{2.4}$$

$$MIPS\ 1\ (24.0\ \mu\ m) : [24]_{mag} = -2.5 * log_{10}\frac{7.17}{Flux_{24}} \tag{2.5}$$

$$MIPS\ 2\ (70.0\ \mu\ m) : [24]_{mag} = -2.5 * log_{10}\frac{0.778}{Flux_{70}} \tag{2.6}$$

where the magnitude zero points are given in units of Jy, which should also be the units of the flux. The Spitzer catalogues will be used in combination with the near-IR WFCAM data to provide a more complete picture of young stellar objects in the IR regime.

2.3 Chapter summary

The ρ Ophiuchi cluster has been monitored with the WFCAM over a total of 14 epochs in the H and K-band. The limiting magnitudes range from $11 < H < 19$ and $10 < K < 18$, and the area surveyed encompasses the cluster's main core and its surroundings over a $\sim$0.8 deg^2 area on sky. The WFCAM pipeline has delivered reduced catalogues with the photometry for all sources, but a further treatment of the data was needed to remove artifacts which arise both from the instrument, and the type of observations. In total, $\sim$16000 stars have been detected over the two years of observations, and these photometric reliable catalogues will be used in the following chapters to study the young stellar population of the Ophiuchus cluster. Additionally, recently released data from the Spitzer Space Telescope on the Ophiuchus cluster will be included in the analysis, providing photometric information in the mid-IR, namely in the 3.6, 4.5, 5.8, 8.0, 24, and 70 μm bands.

Chapter 3

Variable pre-main-sequence stars in Rho Oph

The WFCAM catalogues contain ∼16000 stars with calibrated and reliable H and K photometry in ρ Ophiuchus, encompassing an area of ∼0.8 deg^2. All stars have been observed in a total of 8 to 14 epochs over a period of two years. For the purpose of my thesis, I am interested primarily in using this large dataset of near-IR photometry to search for variable objects in this region, which should mainly contain pre-main-sequence stars, known to be variable due to magnetic activity on their surface, or phenomena related to their circumstellar discs. The goals of the variability survey are twofold. Firstly, I will address the question of how frequent variability is in young stars, within the detection limits. Secondly, I will study the properties of the variability and relate them to physical processes which can explain the observed changes in brightness. In parallel, I will also study the variable objects which have not been previously associated with the ρ Ophiuchi young population, and investigate if they are consistent with being members of this star forming region. This project is only one of the possible applications of these catalogues, which have the potential to produce a large variety of science.

In this chapter, I will detail the results of the variability survey, presenting the methods to identify variable objects, the analysis of their properties, the evidence for association membership, and the possible causes of the variability.

3.1 List of near-IR variable stars

A variable star is one which displays photometric characteristics incompatible with photometric errors. The large sample being analysed required the use of statistical tools which could quantitatively estimate the probability that the detected photometric variations are intrinsic to the star or its circumstellar material.

The first tool used to detect variability was the reduced chi-square $\chi^2(\chi^2_\nu)$ of the magnitudes. If it is assumed that the systematic errors of the photometric measurements are negligible, then the measured magnitude values are only subject to small random errors, and the limiting distribution is expected to be, in this case, approximated by a Gaussian curve centred on the true value of the magnitude of a star. The χ^2 test can then provide a measure of how consistent the observed distribution is with this adopted theoretical distribution. This is better done if the χ^2 that is computed is compared to the number of degrees of freedom (ν), which is defined as the number of observation points minus the number of parameters computed from the data and used in the calculation, which in this case will be 1. This reduced chi-square (χ^2/ν) is a more precise measurement, and the $\chi^2(\chi^2_\nu)$ of the magnitudes is computed as

$$\chi^2_\nu = \frac{1}{\nu}\sum_{i=1}^{N}\frac{(mag_i - m\bar{a}g)^2}{\sigma_i^2}, \tag{3.1}$$

where ν is the number of degrees of freedom, N is the number of measurements, and σ_i is the photometric uncertainty. In this case, the statistic represents the probability that the variations in magnitude observed for a given star result mainly from *Gaussian* noise. Therefore, the reduced chi-square index entirely relies on the assumption that the noise is Gaussian, which is only approximately the case in any real set of observations in which there is variable seeing, bad pixels, detector imperfections, etc. It is also very susceptible to outlier points and does not make use of correlated changes in multiband photometry, further limiting its use.

The second tool used takes advantage of the temporal coherence of the star's light curve and also the correlation across H and K bands, allowing for true signals to be extracted from within the noise. The cross-correlation index (CCI) relies on simple correlation coefficients statistics and was first proposed for use in the search of variable stars by Welch & Stetson (1993). This method, which assumes that photometric errors for two different photometry lists should be uncorrelated, is effective as long as the difference in time between observations in each frame pair (at a given epoch) is small compared with the variation period. The index is defined as:

$$CCI = \sqrt{\frac{1}{N(N-1)}}\sum_{i=1}^{N}\left(\frac{mag_i^H - m\bar{a}g}{\sigma_{H,i}}\right)\left(\frac{mag_i^K - m\bar{a}g}{\sigma_{K,i}}\right), \tag{3.2}$$

where N is the number of measurements and $\sigma_{H,i}$, $\sigma_{K,i}$ are the photometric uncertainties.

A third index (CI_H, CI_K) was computed for each band separately which takes advantage of the temporal coherence of the light curve and can be used to detect long

term variations in a single band. It is defined as

$$CI_K = \sqrt{\frac{1}{N(N-1)}} \sum_{i=1}^{N} \left(\frac{mag_i^K - \bar{mag}}{\sigma_{K,i}} \right) \left(\frac{mag_{i+1}^K - \bar{mag}}{\sigma_{K,i+1}} \right), \tag{3.3}$$

for K band, and similarly for the H band.

For each star, the χ^2_ν, CCI, CI_H and CI_K, were computed for each year separately. A star was classified as variable when it met one of the following criteria:

- $\chi^2_\nu > 17.3$ in one or two bands, meaning only 1 to 2 (to be conservative) false detections in the total sample are expected. The two-tailed probability for a χ^2 distribution with 1 degree of freedom and a χ^2 value > 17.3 is $\sim$0.0064%, which for our sample of $\sim$16000 stars represents 1 to 2 stars.

- CCI, CI_H or $CI_K > 2.0$. Numerical simulations have been used to study the behaviour of the correlation indices, using the software program *Mathcad*[1]. First, the WFCAM catalogue was divided into magnitude bins of 1 magnitude width, i.e., K magnitude $\in$ [10;11[,[11;12[, ... [17;18], and for each star, its average magnitude and standard deviation was calculated over all the nights (usually 7 nights per year). After, the average magnitude and standard deviation of all the stars is calculated per bin. In the simulations, random magnitude values are generated (7, as in the number of nights of observations) for a star using a random normal distribution which has the mean magnitude and standard deviation of a particular magnitude bin. Then the CCI, CI_H or CI_K of the generated magnitudes are calculated per bin, for $\sim$16000 stars, the approximate size of the sample. The procedure is repeated for all magnitude bins. The distribution of values for the three correlation indexes due to random chance over 7 epochs is found to be very similar for all the magnitude bins, and is symmetric about zero, with a maximum value of 1.9. Figure 3.1 shows the CCI, CI_H or CI_K of the stars in the WFCAM catalogues as a function of magnitude. Non-variable stars produce a probability distribution centred about zero due to noise, as expected from the simulations, while true variables show positive values of the CCI greater than 2 (to be conservative). All the correlation indices showed a similar behaviour. The width of the distribution of non-variable stars depends on the total number of epochs used in the calculation of the correlation indices, and so the threshold was scaled accordingly (CCI, CI_H or $CI_K > 2$, 2.16, 2.37, 2.65 for a star with detections in 7, 6, 5, or 4 epochs, respectively).

The application of these criteria led to a raw list of 235 variables. These were visually examined and 59 objects were rejected, primarily because they turned out to be close double stars (Fig. 3.2) which fell inside the aperture, showing fluctuations in magnitude which originated from differences in seeing across the different epochs.

[1]Mathcad is a software used for scientific calculations.

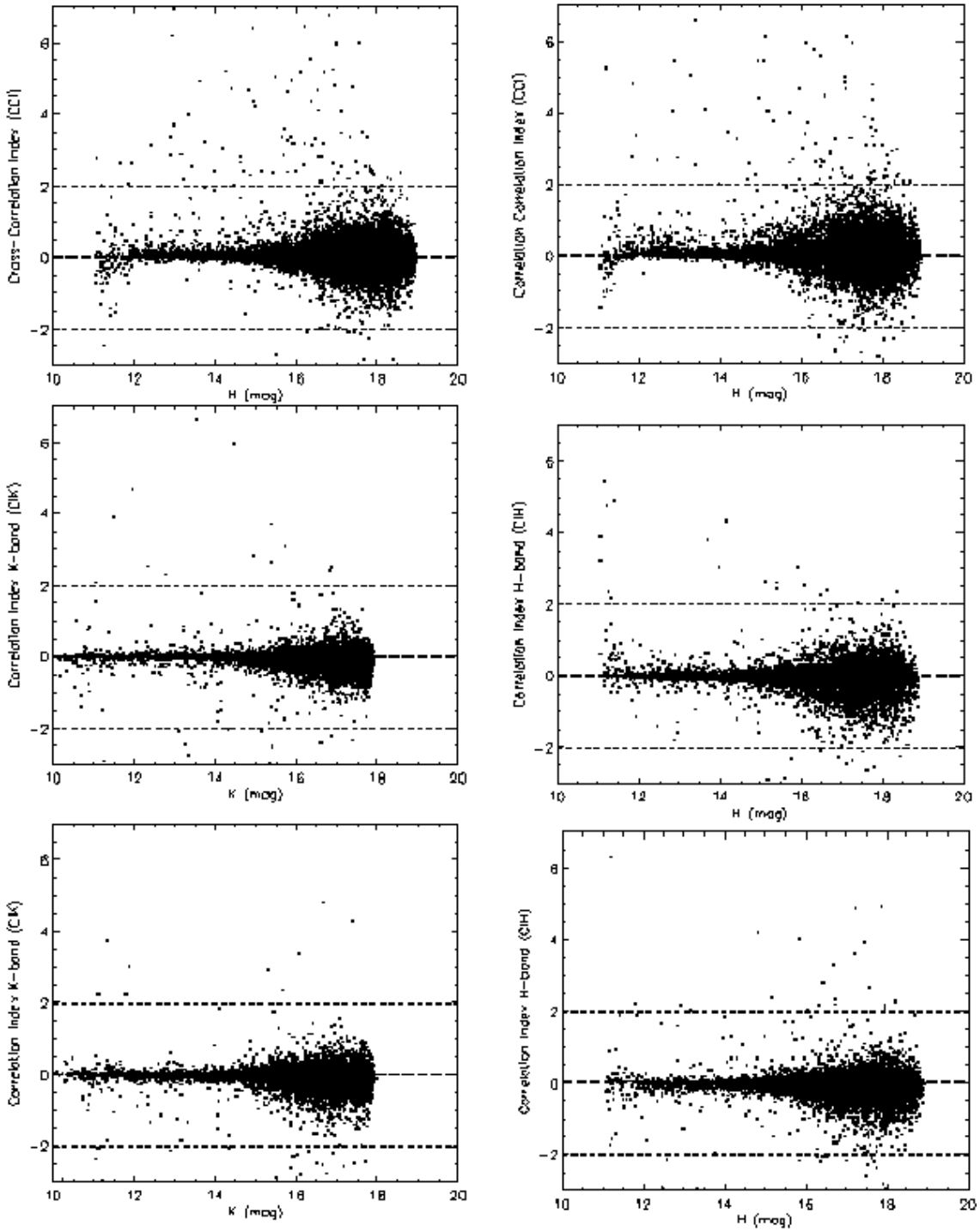

Figure 3.1: Cross correlation indexes (CCI, CI_H or CI_K). Non-variable stars produce a probability distribution centred about zero due to noise, while true variables show positive values greater than 2.

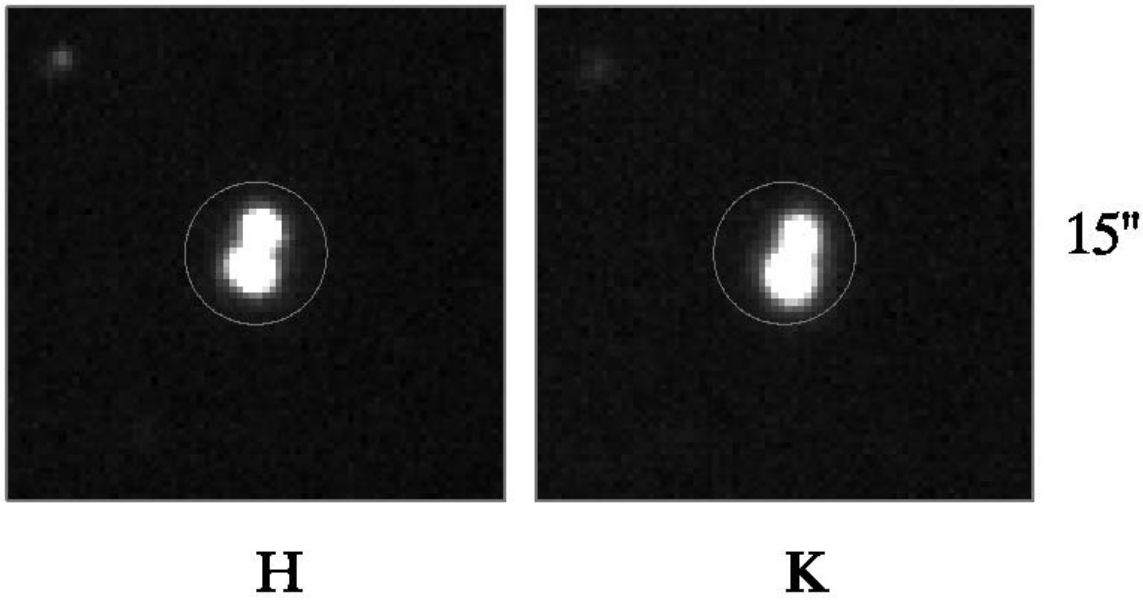

Figure 3.2: Example of close double stars which are considered *false* variables, since the magnitude variation that is seen in the light curves, most probably originates from the difference in seeing across the different nights.

Furthermore, faint objects (K>15.5) which showed variability characteristics consistent with the properties of active field M dwarfs were also removed, since they are more likely to be affected by field contamination. Active low mass M-dwarf (dMe) stars have strong surface magnetic fields (Johns-Krull & Valenti 1996) and show significant levels of coronal activity with maximum amplitude variations in the optical of $\lesssim$0.5 magnitudes (Bondar' 2002). Assuming the same value of amplitude variation for IR variability (to be conservative), a simple starspot model (Vrba et al. 1986, see Sect. 3.8) predicts a maximum colour variation $H-K$ of 0.15 magnitudes. All variables fainter than 15.5 in K–band, magnitude amplitude variations less than 0.5 and colour variations less than 0.15, with a 3σ confidence, were therefore not considered in the final list of candidate members of ρ Ophiuchi since they were consistent with being active M dwarfs. This sample could, however, contain genuine cluster members, and so a table with the main properties has been retained and is shown in Table 3.1.

The final list of variables in ρ Ophiuchi contains 137 variable stars. Table 3.3 shows the photometric properties for each variable star, such as the coordinates, the average H and K magnitudes, the peak-to-peak amplitude for H, K, and $H-K$, the slope in the variability colour-magnitude diagram (Sect. 3.4), evidence for IR-excess as determined from IRAC/MIPS/WFCAM colour-colour diagrams (Sect. 3.5), several variability flags (Sect. 3.8), and references for the known members of ρ Ophiuchi (Sect. 3.2).

Table 3.1: List of variables objects with variability characteristics consistent with active field M dwarfs. The list could still contain young very low mass objects, possibly members of Ophiuchus.

AOC designation	$<H>$ (mag)	$<K>$ (mag)	ΔH (mag)	ΔK (mag)	$\Delta(H\text{-}K)$ (mag)
J162554.64-244112.8	18.20	17.70	0.51	0.33	0.52
J162556.76-243001.1	17.88	16.30	0.22	0.23	0.21
J162609.95-240046.7	17.22	16.84	0.10	0.27	0.32
J162611.05-241208.8	17.66	17.18	0.19	0.40	0.37
J162612.86-241244.1	17.71	17.01	0.22	0.29	0.16
J162619.42-243233.8	18.38	16.98	0.35	0.31	0.32
J162621.54-241242.5	18.61	17.80	0.60	0.32	0.48
J162623.33-242351.4	18.09	16.47	0.57	0.30	0.52
J162631.14-241208.5	16.91	15.65	0.12	0.11	0.12
J162647.88-240946.8	16.42	15.64	0.27	0.26	0.16
J162700.96-241230.6	18.38	17.72	0.40	0.30	0.48
J162705.45-240519.9	17.02	16.43	0.20	0.15	0.13
J162749.40-242919.3	17.82	16.61	0.36	0.20	0.41
J162749.80-243950.1	16.94	16.02	0.39	0.28	0.18
J162750.41-244042.7	17.36	16.43	0.27	0.07	0.26
J162800.15-241222.8	18.35	17.25	0.58	0.16	0.53
J162801.81-241305.0	17.32	16.44	0.25	0.12	0.33
J162803.22-240536.7	16.18	15.63	0.32	0.20	0.15
J162814.41-244546.2	16.88	16.49	0.21	0.18	0.08
J162818.95-241319.1	17.31	16.68	0.20	0.26	0.15
J162840.66-243148.3	17.72	17.22	0.42	0.32	0.35
J162841.89-242705.6	16.33	16.02	0.18	0.20	0.16
J162844.20-240115.1	17.75	17.21	0.32	0.28	0.33
J162846.90-240212.9	16.82	16.46	0.08	0.32	0.28
J162852.34-242849.1	17.63	17.37	0.25	0.25	0.34
J162858.30-243544.2	17.50	16.60	0.22	0.17	0.08
J162902.71-242837.7	16.12	15.78	0.21	0.13	0.21
J162905.65-242314.9	17.79	17.50	0.22	0.20	0.36
J162911.02-242240.0	17.88	17.50	0.32	0.20	0.22
J162919.04-241038.8	17.72	17.15	0.27	0.24	0.22
J162920.93-241936.8	16.36	15.90	0.14	0.11	0.11
J162929.44-243426.3	18.00	17.65	0.57	0.43	0.59
J162930.59-241907.8	18.21	17.68	0.42	0.43	0.28
J162933.26-243359.0	17.96	17.42	0.47	0.27	0.59
J162937.02-243035.2	16.75	16.40	0.13	0.19	0.10
J162939.40-242309.4	17.19	16.82	0.30	0.19	0.21
J162943.28-243056.4	17.96	17.57	0.54	0.52	0.38
J162943.49-243102.7	16.67	16.45	0.22	0.18	0.23
J162945.00-243421.7	17.71	17.39	0.46	0.33	0.28

3.2 Known Population of the Ophiuchus Molecular Cloud

Many imaging and spectroscopic studies have been done on the Ophiuchus molecular cloud from the X-ray regime to the submillimeter, resulting in a known population of ∼300 members of this cluster (Wilking et al. 2008). ρ Ophiuchi was one of the first star forming regions to be observed in X-rays with the *Einstein* space telescope (Montmerle et al. 1983), and since then many more YSOs have been uncovered with X-ray surveys. Following the technological advances that open the possibility for better X-ray satellites, the number of YSOs with X-ray detections has increased in proportion to the increasing sensitivity. At the present day, approximately one third of the known population of Ophiuchus has been detected in X-rays in surveys using *ROSAT* (Casanova et al. 1995; Martin et al. 1998; Grosso et al. 2000), *ASCA* (Kamata et al. 1997), *Chandra* (Imanishi et al. 2001; Gagné et al. 2004), and *XMM-Newton* (Ozawa et al. 2005). The results from these surveys and their implications for this study will be discussed in more detailed in Sect. 3.6. Also in the near-IR, a significant improvement in near-IR arrays has made it possible to go from shallow surveys, over small areas on sky (e.g., Vrba et al. 1975; Elias 1978), to much deeper studies which provided a better understanding of the extension of the cloud and also contributed to finding hundreds of obscured young objects (e.g., Greene & Young 1992; Comeron et al. 1993; Strom et al. 1995; Barsony et al. 1997; Allen et al. 2002). The full coverage of the cloud in the near-IR has been done with the all-sky 2MASS survey (Cutri et al. 2003). However, only with the advent of WFCAM and this thesis, has a large area (∼1°) of the Ophiuchus cluster been surveyed uniformly deep in the near-IR regime (Alves de Oliveira & Casali 2008). In the mid- and far-IR domain, more suitable to detect emission from circumstellar dust in discs or envelopes, but also to penetrate the high extinction in the cloud's core, the first studies were done with *IRAS* (Wilking et al. 1989; Wilking 1992). However, during the last decade, the launch of *ISO*, the Infrared Space Observatory, has brought a significant improvement both in sensitivity and spatial resolution. A large survey of Ophiuchus was done by Bontemps et al. (2001) using ISOCAM, which identified more than 100 YSOs in the mid-IR. Finally, the Spitzer Space Telescope was launched in 2003 (see Sect. 2.2) and represents a large increase in sensitivity of hundreds, in comparison to ISO. The Ophiuchus cloud was one of the instrument's targets (e.g., Padgett et al. 2008), and this thesis makes use for the first time of part of these data, now made public (see Sect. 3.5). Finally, also at longer wavelengths important studies have been performed in Ophiuchus in the millimeter and submillimeter regime, where the cold dust of YSOs can be studied. For completeness, the main recent surveys conducted in the Ophiuchus cloud at longer wavelengths should be mentioned, namely, in the mm continuum, with IRAM/MPIfR (Motte et al. 1998), JCMT/SCUBA (Wilson et al. 1999; Johnstone et al. 2000), and SEST/SIMBA (Stanke et al. 2006), which have resulted in an approximately complete census of Class 0 and Class I YSOs in Ophiuchus (Wilking et al. 2008).

The WFCAM catalogue was merged with the previously known members of ρ Ophiuchi, and WFCAM counter-parts were found for 128 previously known members. Of the sources not successfully matched, many are present in source tables of other surveys in the literature, but they did not posses characteristics which enable them to be classified as young cloud members rather than background stars or galaxies by their authors. A significant fraction of the ρ Ophiuchi population is not recovered simply because the objects are too bright, and therefore heavily saturated in the WFCAM images. Also the very extended objects are not present in the final catalogues since, to avoid galaxy contamination, this type of object was rejected. From the 128 known members with WFCAM counter-parts, 45% are variable stars, according to the previous definitions. In the sections that follow, variable stars which have been confirmed as members of the cloud by these other studies are referred to as *members*. Variables which have not been confirmed as members are referred to as *candidate members*.

In a survey of the Trapezium region of the Orion Nebula Cluster (ONC, at a distance of $\sim$400 pc), done by Carpenter et al. (2001) with 2MASS, the authors examine the fraction of stars in their area coverage and withing their photometric limits, exhibiting near-IR variability. They find $\sim$45% of the cloud members with $K < 11.0$ to be variable. However, for cloud members with K magnitudes > 12.0, only $\sim$14% show variability. They investigate the possibility that the fainter cloud members could be intrinsically less variable, but conclude that this result is only due to an increase in photometric noise at the fainter limits, which restricts the detection of variability. The WFCAM data limits extend to $\sim$3 magnitudes fainter than the magnitudes of the currently known members of Ophiuchus (K<15). The WFCAM data provides excellent photometry at this wavelengths, with average errors $\sim$0.01 magnitudes up to $K\sim$15.0 (see Table 2.3). Therefore, the magnitude range of the known variable members (10.0<K<15.0), has uniform levels of photometric noise and can be used to evaluate this question, i.e., to investigate the fraction of young stars (previously confirmed) showing near-IR variability. Fig. 3.3 shows the histogram of the number of members of the Ophiuchus population per magnitude bin (dotted line), and overplotted are the number of these members which were detected in the WFCAM catalogues (dashed line), and the ones that show near-IR variability (solid line). It is observed that the fraction of variable stars as a function of magnitude closely resembles that of the cluster's stellar population detected in the WFCAM catalogues, which in turn reflects the distribution of the whole Ophiuchus population. Therefore, it can be concluded that the frequency of variable member stars does not depend on magnitudes.

3.3 Magnitudes and colours of the variable stars

The colours and magnitudes of the variable stars are important clues in investigating the youth and masses of these objects. Several spectroscopic studies have been made

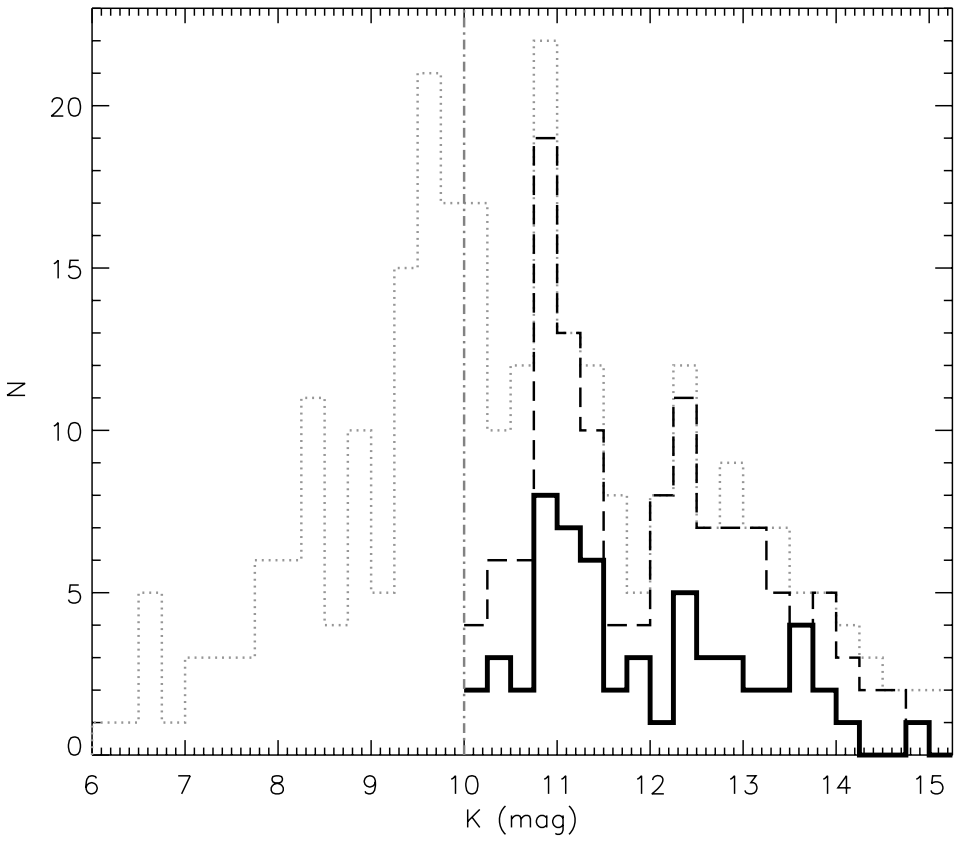

Figure 3.3: Histogram of the total number of members of Ophiuchus (dotted line), the number of members present in the WFCAM catalogues (dashed line), and the number of members which show near-IR variability (solid line), as function of the K magnitude. The vertical line at K=10.0 shows the saturation point of the WFCAM dataset.

of the ρ Ophiuchi cluster from which an age has been derived. Using optical spectroscopy, Bouvier & Appenzeller (1992) have obtained spectral types for ∼30 young objects scattered over the cluster's centre and surroundings, and derive ages which range from 1 to 10 Myr. Also using optical spectroscopy for several X-ray sources associated with the cluster, Martin et al. (1998) found evidence for older pre-main-sequence stars surrounding the cluster's core, where they derive a younger age. More recently, an extensive Hα survey by was done by Wilking et al. (2005) using a multi-object spectrograph. The authors collected spectra for 139 objects distributed over a large area of ∼1.3deg^2, including the area surrounding the cloud. They derived a median age of 2.1 Myr, with some members up to 3 Myr, for more widely distributed members, which they claim to be identical of that of low mass stars in the Upper Scorpius subgroup, and also significantly older than the ages of the pre-main-sequence stars at the very centre of the cluster. Finally, using near-IR spectroscopy, (Greene & Meyer 1995; Luhman & Rieke 1999) have found the age of objects in the core of ρ Ophiuchi to be 0.3 Myr.

The colour-magnitude diagram, K vs. H-K, shown in Fig. 3.4, displays the average magnitude and colour of the variable members of ρ Ophiuchi (open squares) and the candidate members (filled circles). The curves in the diagram show the model evolutionary tracks of the Lyon group (Baraffe et al. 1998; Chabrier et al. 2000; Baraffe et al. 2003) for a cluster at a distance of 119 pc (Lombardi et al. 2008). The solid curve shows the theoretical 1 Myr isochrone, as a reference age, for low mass stars ranging from 0.5 $M_\odot$ down to 0.003 $M_\odot$ ($\sim 3 M_{Jup}$). The isochrone is a combination of the NextGen and the DUSTY isochrones (Baraffe et al. 1998; Chabrier et al. 2000). The dashed and dotted curves show the COND isochrones (Baraffe et al. 2003) for 1 and 5 Myr, respectively, down to $\sim 3 M_{Jup}$. The lines parallel to the reddening vector (Rieke & Lebofsky 1985) mark the separation between stars, brown dwarfs (M<0.075 $M_\odot$) and planetary mass candidates (M<0.012 $M_\odot$) for the different isochrones. All evolutionary tracks presented are based on stellar interior physics and *non-grey* atmosphere models. The main differences between them arises from the treatment of dust. The 'NextGen' isochrones are based in dust-free atmosphere models and represent the evolutionary models from 1 $M_\odot$ down to the hydrogen burning minimum mass (Baraffe et al. 1998). The 'DUSTY' models include the formation of dust in the equation of state, and the scattering and absorption of dust in the radiative transfer equation, and are more suitable for the study of very low-mass stars and brown dwarfs, with $T_{eff} \lesssim 2800$ K (Chabrier et al. 2000). The 'COND' models neglect dust opacity in the radiative transfer equation and are more appropriate to the study of cool brown dwarfs, with $T_{eff} \lesssim 1300$ K (Baraffe et al. 2003). In Fig. 3.4, the models indicate that the brighter candidates are above the hydrogen burning limit, but the faint sources would extend to very low masses. If an age of 1 Myr is considered, the faintest variable objects would have just a few Jupiter masses. However, when an older age is considered (dotted line), the objects would become more massive. Wilking et al. (2005) found a distributed population in Ophiuchus which is significantly older than that in the more highly extincted cloud core, with ages up to 3 Myr, so it is plausible that part of the variable objects are older than the core population. Although the CMD gives a good indication of the approximate masses of the variable objects, a spectroscopic follow-up is needed to investigate their nature.

3.4 Characteristics of the variability

The timescales of variability which can be studied with this dataset can be divided into two groups: intermediate and long time scales. The first applies to the stars which only show variability in one of the two years of observations, and are likely to represent physical phenomena which have a maximum duration of a few months. The long term variables are stars that show variability behaviour across both years, which could be caused either by a single mechanism or be the result of repeated shorter term vari-

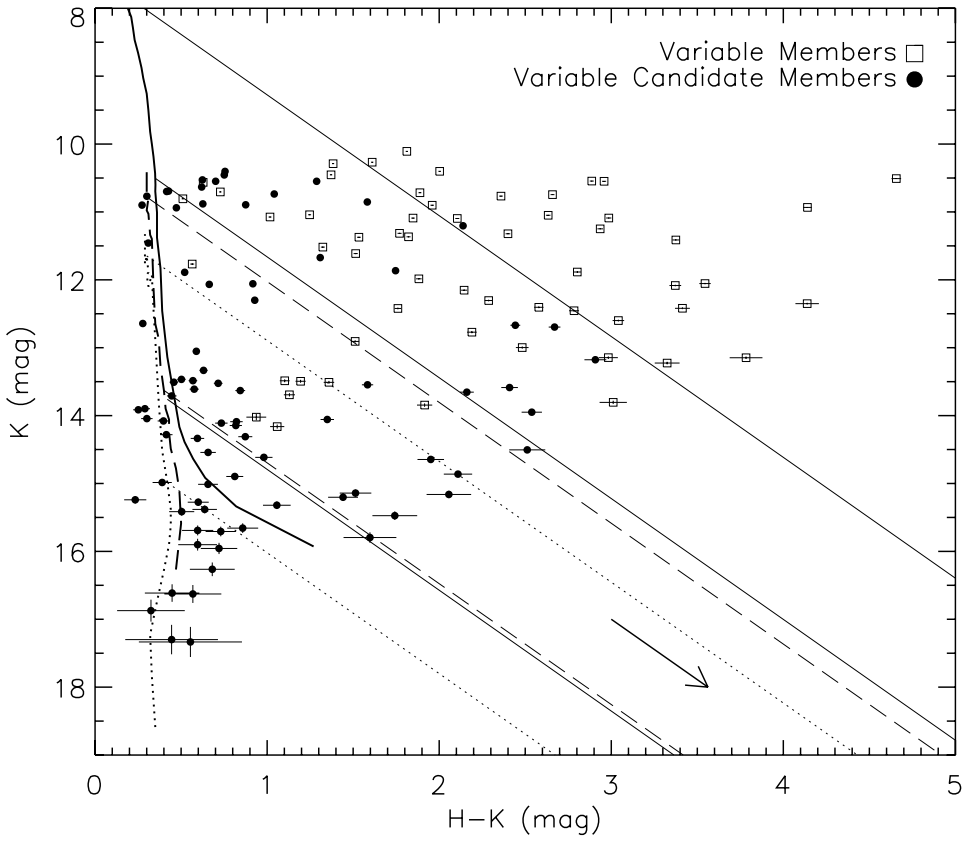

Figure 3.4: Colour-magnitude diagram for variable members (open squares) and variable candidate members (filled circles) of ρ Ophiuchi. Isochrones at 119 pc from the Lyon group are shown: vertical solid line is a combination of the NextGen and Dusty isochrones at 1 Myr, dashed and dotted lines are the COND isochrones for 1 Myr and 3 Myr, respectively. Lines parallel to the A_K=1 mag reddening vector (Rieke & Lebofsky 1985) mark the separation between stars and brown dwarfs, and planetary mass candidates for the different isochrones.

ability phenomena. In the list of member variables, 75% of the stars show variability over the two years, while 25% appear to be variable only in the first or second year. The values for the candidate members are slightly different, where 53% of the objects are variable in both years and the remaining 47% show variability in only one of the years of observations. Figure 3.5 is an example of a candidate member of ρ Ophiuchi, which shows no significant variations in the first year but large variations in the second year. Given the sparse cadence of the observations, a search for periods has not been attempted.

The amplitude of the variations was measured as the peak-to-peak fluctuation in magnitudes and colour, for each year separately and also for the combined data. Figure 3.6 shows histograms of the peak-to-peak magnitude amplitude for all the variable

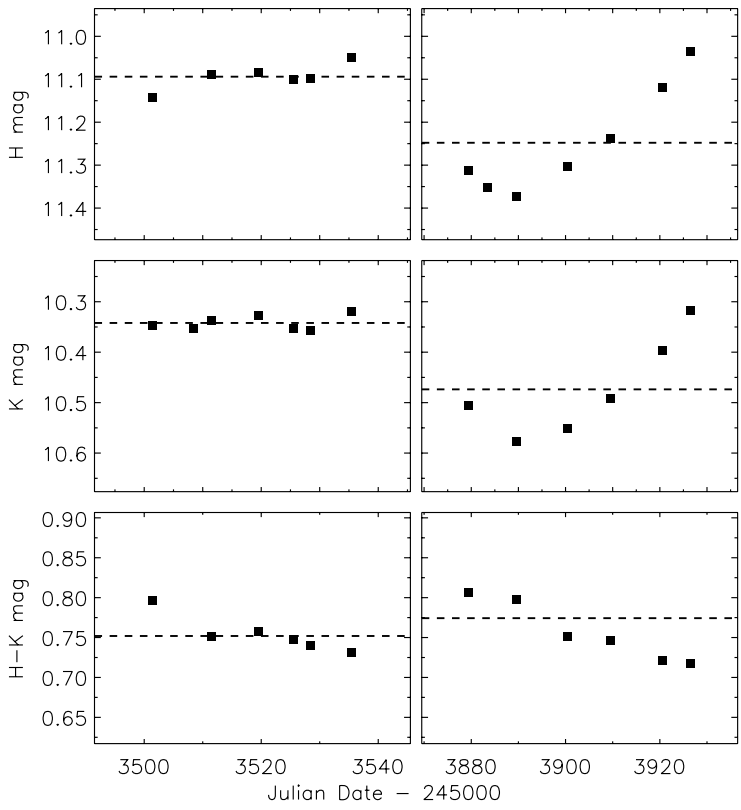

Figure 3.5: AOC J162814.77-242322.5; variable candidate member star with no significant variations in the first year and large variations in the second year. The panels show the H, K, $H-K$ light curves. The left panels show the data points from 2005 May-June, and the right panels the photometry from 2006 May-July. The dashed lines show the mean values.

stars, members and candidate members. They show a peaked distribution, with most of the amplitude values ranging from 0.01 to 0.8 magnitudes. Table 3.2 shows the mean and maximum values of the amplitudes for the members and candidate members. When the variation is measured across the two years, the average amplitude for the variable members is of the order of a few tenths of a magnitude. One extreme object, AOC J162636.81-241900.2, has been excluded from the calculations of Table 3.2 (see Sect. 3.8). The candidate member variables show mean K, H, and $H-K$ amplitudes of the same order as the variable members within 2σ. There is no statistical evidence that members and candidate members represent different populations.

Most of the variable objects show a variation in $H-K$ colour, which is on average 0.1 magnitudes but can be as large as 1 magnitude (see Fig. 3.7). In some cases, this variation is correlated with the change in brightness, and can be an important indicator of the underlying causes of variability (Carpenter et al. 2001). This behaviour is illus-

Table 3.2: Amplitudes of the Variability

		Year 1		Year 2		Years 1 and 2		
	Band	Mean	Max.	Mean	Max.	Mean	$\sigma/\sqrt{n-1}$	Max.
Variable Members	H	0.18	0.82	0.19	0.88	0.27	0.03	0.97
	K	0.15	0.62	0.14	0.56	0.21	0.02	0.62
	$H-K$	0.09	0.36	0.08	0.36	0.14	0.02	0.52
Variable Candidates	H	0.17	0.82	0.16	0.66	0.22	0.02	0.82
	K	0.13	0.61	0.13	0.61	0.18	0.02	0.65
	$H-K$	0.15	0.97	0.12	0.70	0.18	0.02	0.97

trated in Fig. 3.8, where the variations in the K-band are linearly correlated with the changes in colour. The slopes in the colour-magnitude diagram K vs. $H-K$ were computed using the linear regression method for objects which showed a highly significant linear correlation between change in colour and brightness, i.e. with $< 1\%$ probability that uncorrelated variables would yield a correlation coefficient at least as high as the assumed threshold. 36% of all the variables, members and candidate members, satisfy the linear correlation criterion and the respective slopes are listed in Table 3.3. The angle convention used by Carpenter et al. (2001) was adopted, where a slope angle of 0° represents a positive $H-K$ colour change without a variation in K magnitude, and increases clockwise. Figure 3.9 is the histogram of the derived slopes which shows a binomial distribution with 16 objects having positive slopes, colour becoming redder as they fade, and 33 showing negative slopes, colour becomes bluer as the star gets fainter. These distinct behaviours can be associated with physical processes and will be discussed later in this chapter (see Sect. 3.8).

3.5 Infrared excesses

Many young stars show infrared emission which originates from dusty envelopes and circumstellar discs surrounding the central object. Lada & Wilking (1984), based on the level of long wavelength excess with respect to a stellar photosphere emission, identified three different classes which define an IR-excess or SED classification scheme: Class I, low mass protostars surrounded by an infalling envelope with large IR-excess; Class II, young stars with accretion discs and a moderate IR-excess (as classical T Tauri stars, CTTSs); and Class III, stars which no longer accrete matter from a circumstellar disc and show no IR-excess (as weak-line T Tauri stars, WTTSs). The IRAC data from Spitzer allows the study of these objects in the mid-IR, where the excess contribution from discs and envelopes is predominant. The IRAC colour-colour diagram ([3.6]−[4.5] vs. [5.8]−[8.0]) was presented as a tool to separate young stars of different classes (Allen et al. 2004; Megeath et al. 2004), and was already used in the study of other star forming regions as, for example, Taurus (Hartmann et al. 2005;

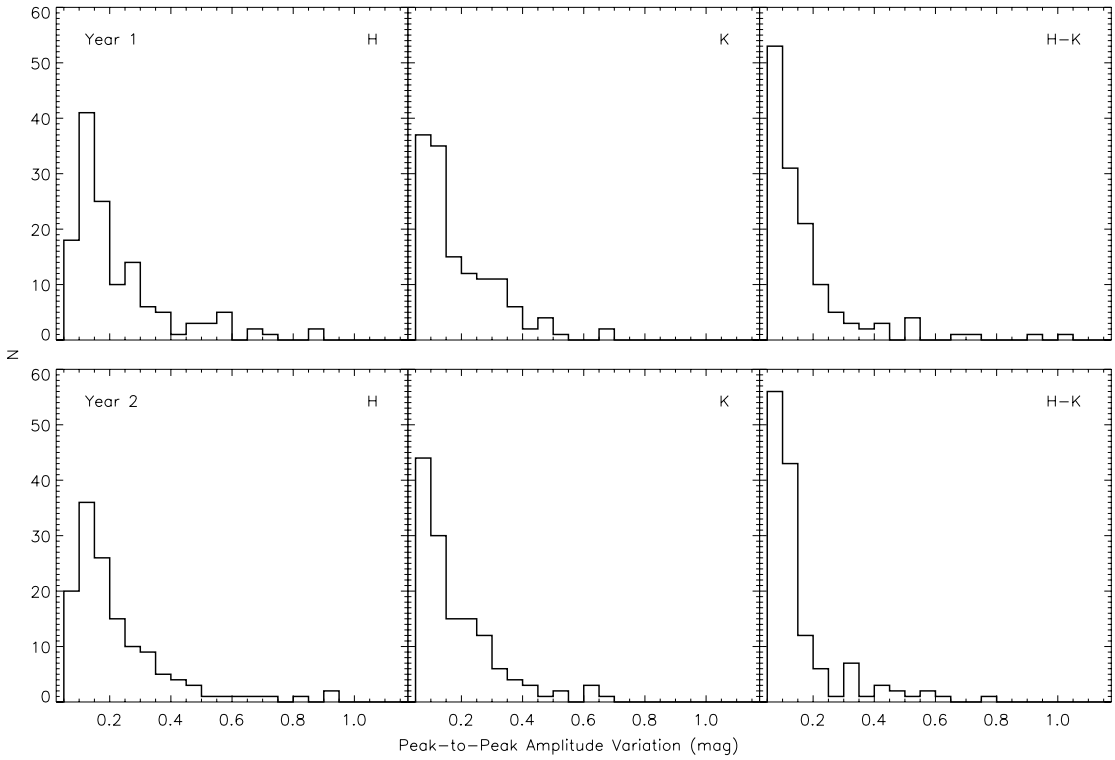

Figure 3.6: Histograms of the peak-to-peak magnitude amplitude of the variations in H, K and H-K. The top panels show the histograms for year 1 and the bottom panels for year 2.

Luhman et al. 2006), Serpens (Harvey et al. 2007), or Chamaeleon II (Porras et al. 2007).

The majority of population of ρ Ophiuchi has been classified into SED classes. Bontemps et al. (2001) used ISOCAM mid-IR bands (6.7 and 15.3 μm) to detect and classify 212 sources. Using ground-base mid-IR observations, Barsony et al. (2005) confirmed those results. Also in the X-ray regime, Chandra and XMM-Newton observations (Imanishi et al. 2001; Gagné et al. 2004; Ozawa et al. 2005) have contributed to the classification. The variability catalogue contains 47 variable members of ρ Ophiuchi which were classified in these studies into Class I, II, or III. Figure 3.10 shows the IRAC colour-colour diagram for all variable objects with detections in the four bands, where the top diagram displays ρ Ophiuchi members and the bottom diagram the candidate members. The variable members are displayed according to the SED class assigned in the literature, i.e., Class I (open squares), Class II (crosses), and Class III (open triangles). The extinction vector is from Flaherty et al. (2007). For comparison, a sample of objects has been chosen from a region of the sky away from the central cloud with little extinction which should mainly contain field stars.

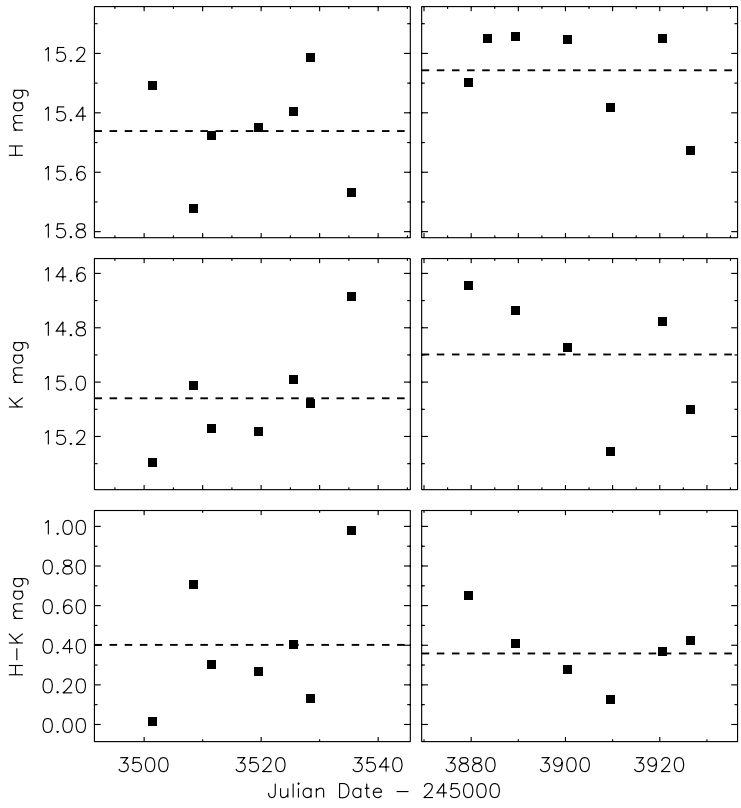

Figure 3.7: AOC J162814.73-242846.6; variable star with large variations in magnitude as well as in colour.

The objects tend to cluster around three main regions of the diagram. Centred in the origin, [3.6]−[4.5],[5.8]−[8.0]=(0,0), are sources which have colours consistent with stellar photospheres and have no intrinsic IR-excess. These can be foreground and background stars, but also Class III stars which do not have significant circumstellar dust. In this region of the colour-colour plane, it is not possible to differentiate between young stars and contaminants. However, as it can be seen in the top panel of the diagram, many of these objects are confirmed young members of ρ Ophiuchi both from mid-IR and X-ray studies. Another preferred region for objects in the diagram is located within the box defined by Allen et al. (2004) which represents the colours expected from models of discs around young, low-mass stars. In fact, many of the Class II objects classified by Bontemps et al. (2001) lie within that range. However, some sources previously identified as Class II do not fall within the predicted limits. These objects have colours inconsistent with Class II sources (higher [3.6]-[4.5] colours than Class II but lower [5.8]−[8.0] colours than Class I) and were previously classified as candidate flat spectrum objects. Their location in this diagram does not confirm them as transition objects between Class I and II (Bontemps et al. 2001) since they can be explained as reddened Class II sources. Finally, from models of infalling envelopes,

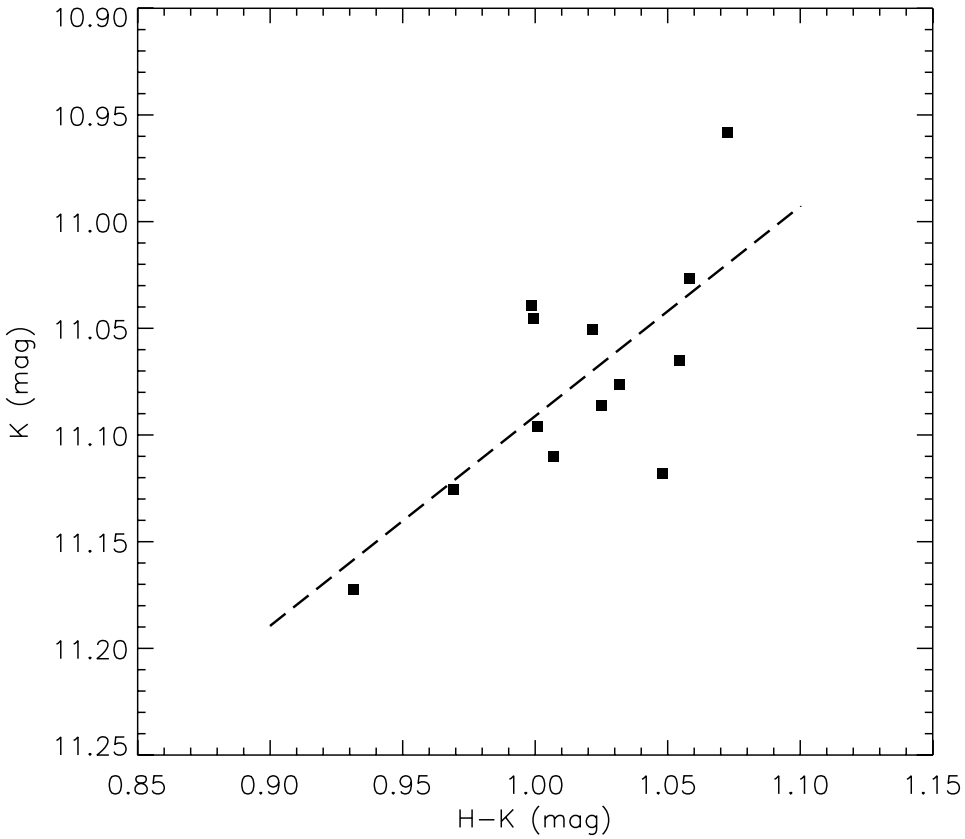

Figure 3.8: AOC J162812.72-241135.8; variable star with linearly correlated changes in $H-K$ colour and brightness in K band. Its colour gets bluer as the star gets fainter. The dashed line shows the linear fit.

Allen et al. (2004) predicts the colours of Class I sources to have ([3.6]−[4.5]) > 0.8 and/or ([5.8]−[8.0]) > 1.1, which agrees well with the two Class I objects identified with ISOCAM (Bontemps et al. 2001). Likewise, one of the sources classified with ISOCAM as Class III lies on the Class I/reddened Class II region of the colour-colour diagram. In the ISOCAM paper, this source was classified as Class III because it is located within the CS contours of the cloud, as defined by Liseau et al. (1995). According to the IRAC diagram, its previous classification is incorrect.

From the 80 candidate members, 54 are detected in all IRAC bands and plotted in the bottom panel of Fig. 3.10 (filled circles). Ten variable members are also detected in the four bands but have no assigned SED class and therefore are included (open diamonds). According to the criteria described above, they can be divided into Class I (1 object), Class II (15 objects). The remaining objects are located in the Class III region of the diagram. For the confirmed members, they can be classified as Class III (5 objects). The variable candidate members, cannot be assigned a SED class, since that region of the diagram is also populated by foreground and background stars.

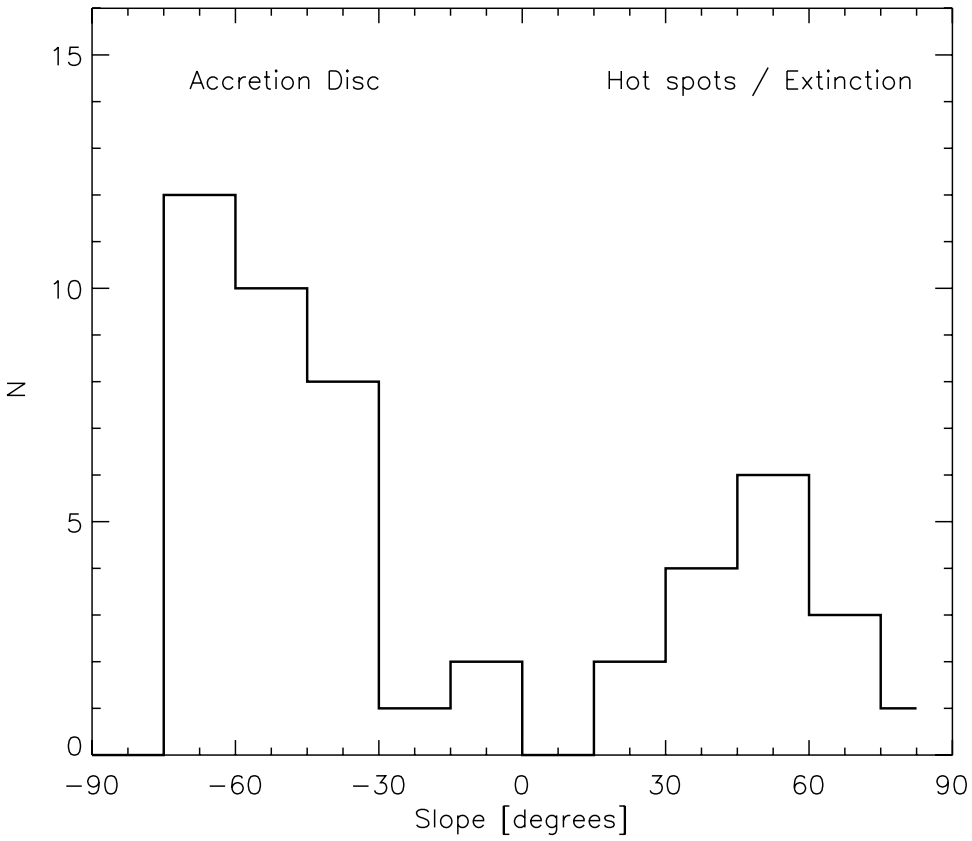

Figure 3.9: Histogram of the derived slopes in the K vs. $H-K$ diagram. The slope can be used as a tool to distinguish the physical mechanisms behind the observed variations (Sect. 3.8).

The number of variables with detections in the 4.5 μm IRAC/Spitzer band is higher than for longer wavelengths, since this band has a higher sensitivity. Figure 3.11 shows the $H-K$ vs. $K-[4.5]$ colour-colour diagram for all variable objects with detections in the IRAC/Spitzer 4.5 μm band, where again the top diagram displays the members of ρ Ophiuchi and the bottom diagram the candidate members. The variable members are displayed according to their SED class from the literature (same convention as in Fig. 3.10). The reddening vector is from Flaherty et al. (2007) and the dash line follows the same reddening law. The top panel of Fig. 3.11 shows a clean break between Class I/II and Class III stars (i.e., stars with and without circumstellar dust emission) for $K-[4.5]>1$ and $H-K>0.5$. The only two exceptions are from the same two objects mentioned in the previous colour-colour magnitude, which showed an excess in the mid-IR too high to be in agreement with their classification (as Class III) from the literature. Applying this criterion to the variable candidate members (bottom panel), 7 candidate members can be classified as ClassI/II, and 8 as possible Class III. Furthermore, for objects present in both diagrams, the SED classes are in agreement.

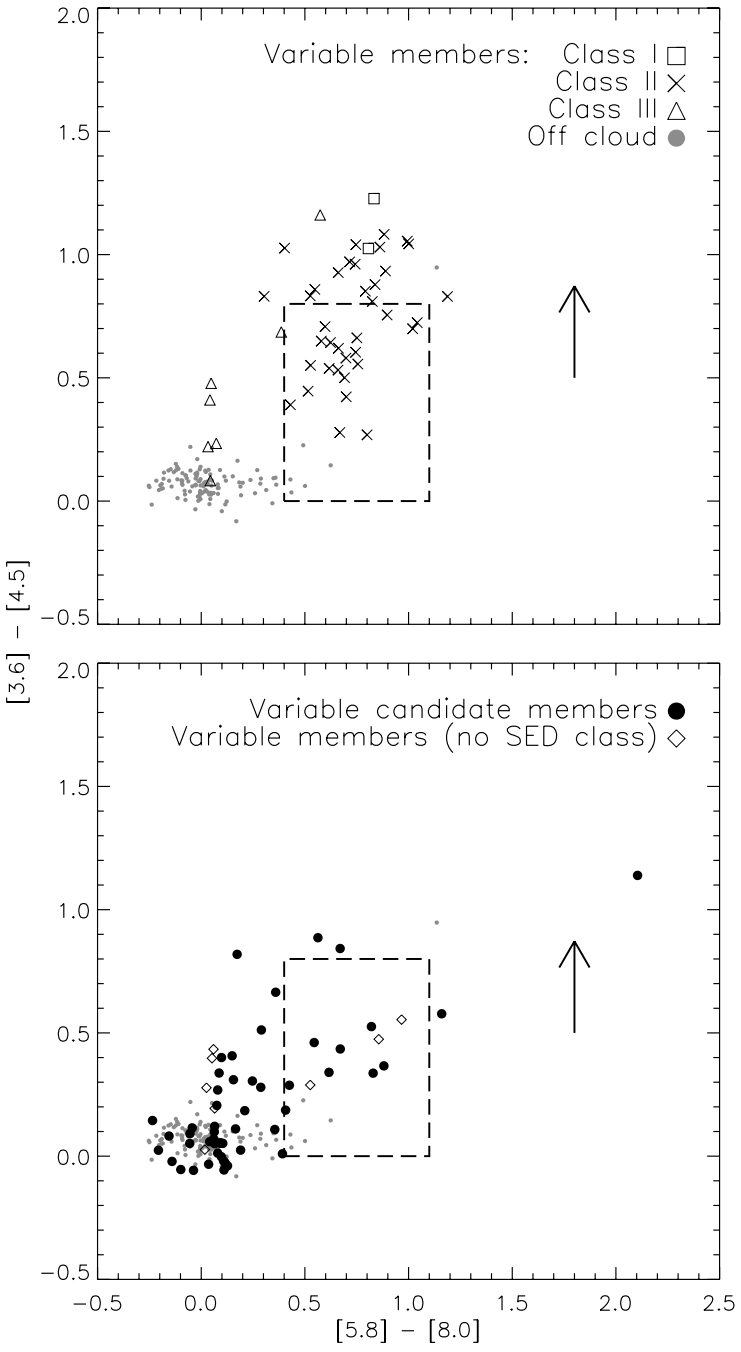

Figure 3.10: IRAC colour-colour diagram for variable members (top panel) and candidate members (bottom panel). Arrow represents the A_k=4 extinction vector for ρ Ophiuchi (Flaherty et al. 2007).

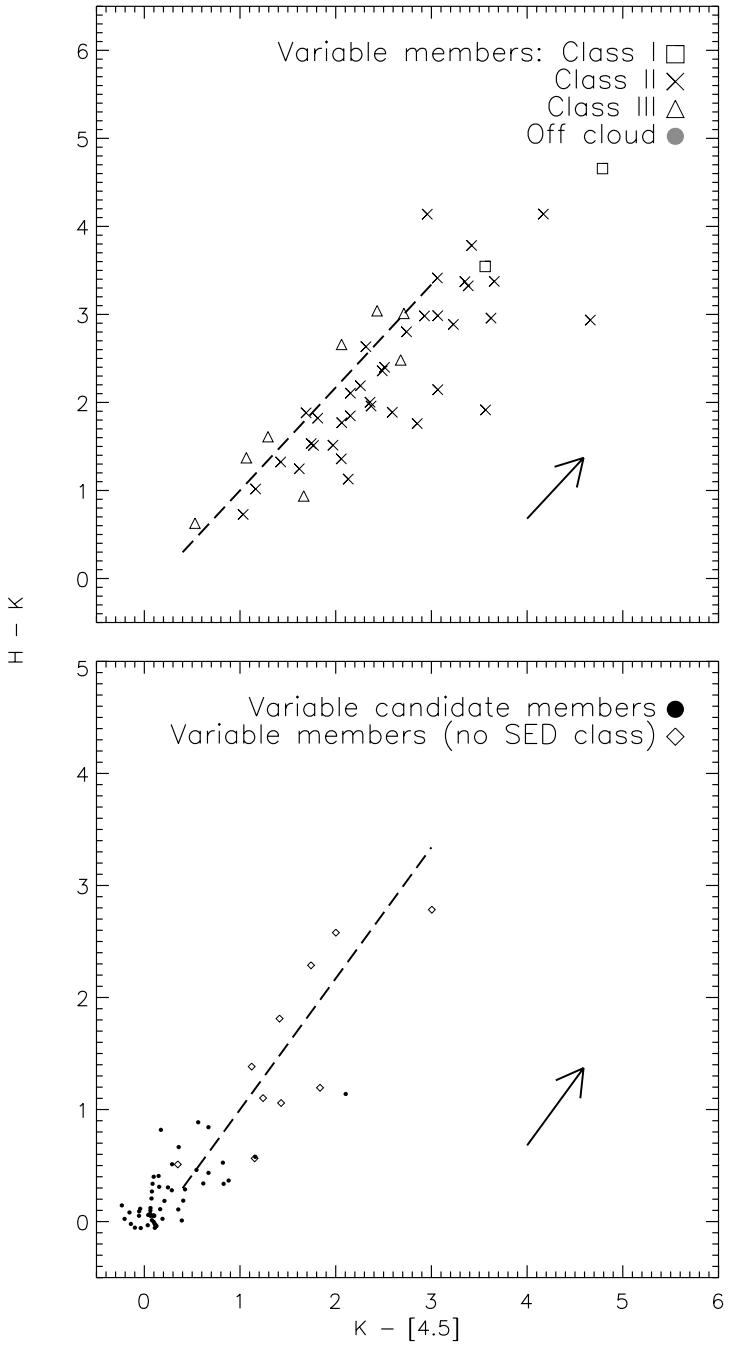

Figure 3.11: WFCAM/IRAC colour-colour diagram. Arrow represents the A_V=10 extinction vector for ρ Ophiuchi (Flaherty et al. 2007).

Another useful tool to look for IR excess (a sign of youth), is to combine near-IR data from WFCAM with the MIPS/Spitzer to study the magnitude-colour diagram K_s vs. K_s-[24] (Fig. 3.12). This diagram has been used to separate YSOs with IR excess from stars in several Spitzer papers (e.g. Rebull et al. 2007; Padgett et al. 2008). The sensitivity of the 24 μm band is more limited in relation to the IRAC bands, and not all of our sources have detections in this band. From the variable members, 48 have reliable photometry and their position in the K_s vs. K_s-[24] diagram is shown in Fig. 3.12 using the same convention for the symbols as in Fig. 3.10, which represent their SED class from the literature. In this diagram, stellar photospheres are clustered around $K_s-[24]$ μm$\sim$0, and sources with $K_s-[24]\sim2$ show a strong IR excess. The reddening vector is from Flaherty et al. (2007) and represents an A_K of 5 magnitudes. Following Greene et al. (1994) mid-IR classification scheme (based on the α index), an indication of the type of objects in question can be obtained. According to this classification (see also Rebull et al. 2007), objects with $K_s-[24]$ μm > 8.31 are Class I objects, $6.75 < K_s-[24]$ μm < 8.31 are flat-spectrum objects, $3.37 < K_s-[24]$ μm < 6.75 are Class II objects, and $K_s-[24]$ μm < 3.37 are Class III. All, except 2, of the variable members that have detections in the [24] μm MIPS band show an IR excess, and these are classified according to their position in the diagram, i.e. Class I (6 objects), Flat spectrum (18 objects), Class II (16 objects), Class III (2 objects). The candidate members, but also members without a SED classification, are displayed in the lower panel of Fig. 3.12, and according to the above discussion can be classified as Class I (2 objects), Flat spectrum (4 objects), Class II (14 objects), and possible Class III (6 objects).

Finally, 6 of the known variable members of Ophiuchus have photometry in the 70 μm MIPS band. Fig. 3.13 shows the [24] vs. [24]-[70] colour-magnitude diagram for these objects. Objects with colours close to 0 indicate a stellar photosphere, but in this region there should be few or any stars with a bare stellar photosphere which are bright enough to be detected in the shallow survey of MIPS (Padgett et al. 2008). The diagram shows that the position of the objects is consistent with them being very young and not extragalactic sources, whose colours would fall in the region inside the dashed box. This has been shown by Padgett et al. (2008), who compared the colours of YSOs in the MIPS data with those of the SWIRE ELAIS N1 extragalactic field, finding that the extragalactic sources are fainter than YSOs in the 24 μm band and have also redder colours.

It has been shown that the combination of WFCAM with IRAC and MIPS data, is an efficient way to detect IR excess emission characteristic of YSOs. Since the above colour-magnitude and colour-colour diagrams are affected by errors, a definitive SED classification for each source is not provided. Instead, variable members and candidates are simply classified as having an indication of IR excess or not. This information is sufficient to look for correlations between the variability observed and the possible physical causes behind it, and the presence or not of IR excess (see Sect. 3.9). In total, approximately half of our total list of variable stars (48%) show IR-excess (Table 3.3).

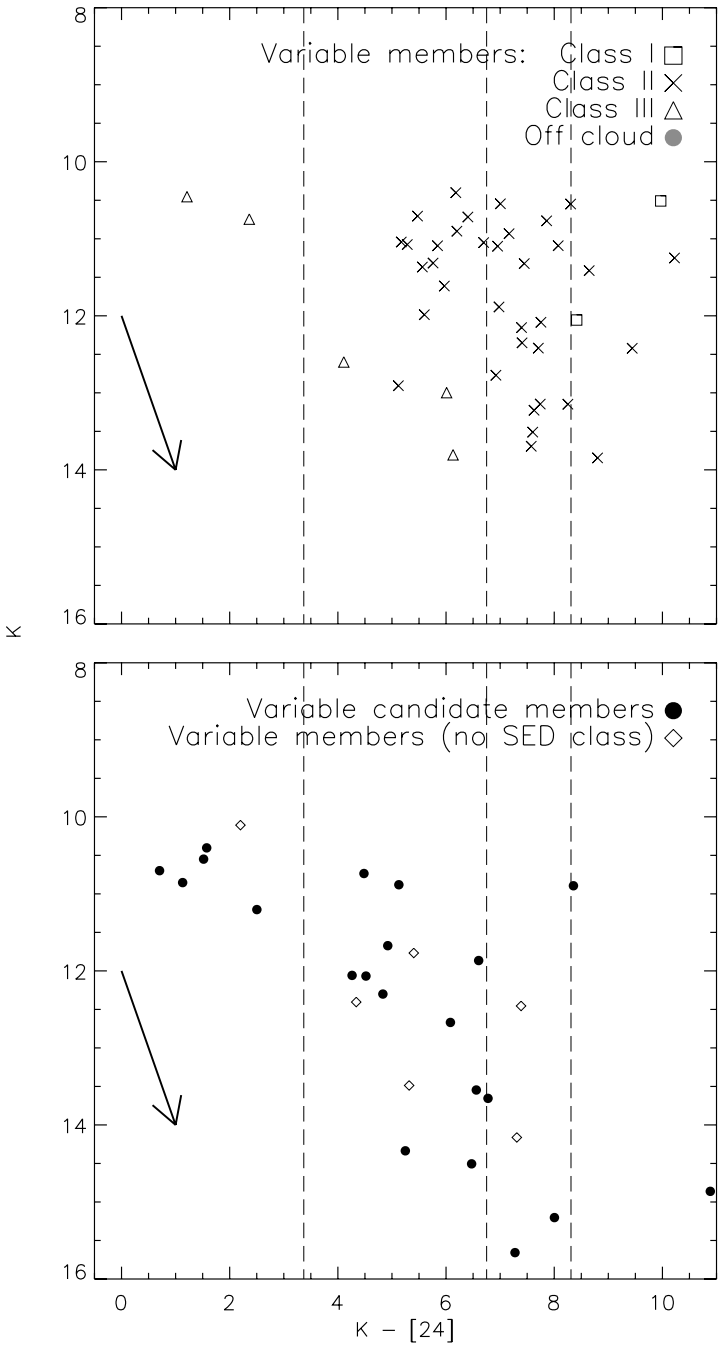

Figure 3.12: WFCAM/UKIRT and MIPS/Spitzer colour-magnitude diagram. The reddening vector is from Flaherty et al. (2007) and represents an A_K of 5 magnitudes. Objects with K_s-[24] > 8.31 are Class I objects, $6.75 < K_s$-[24] < 8.31 are flat-spectrum objects, $3.37 < K_s$-[24] < 6.75 are Class II objects, and K_s-[24] < 3.37 are Class III (Greene et al. 1994).

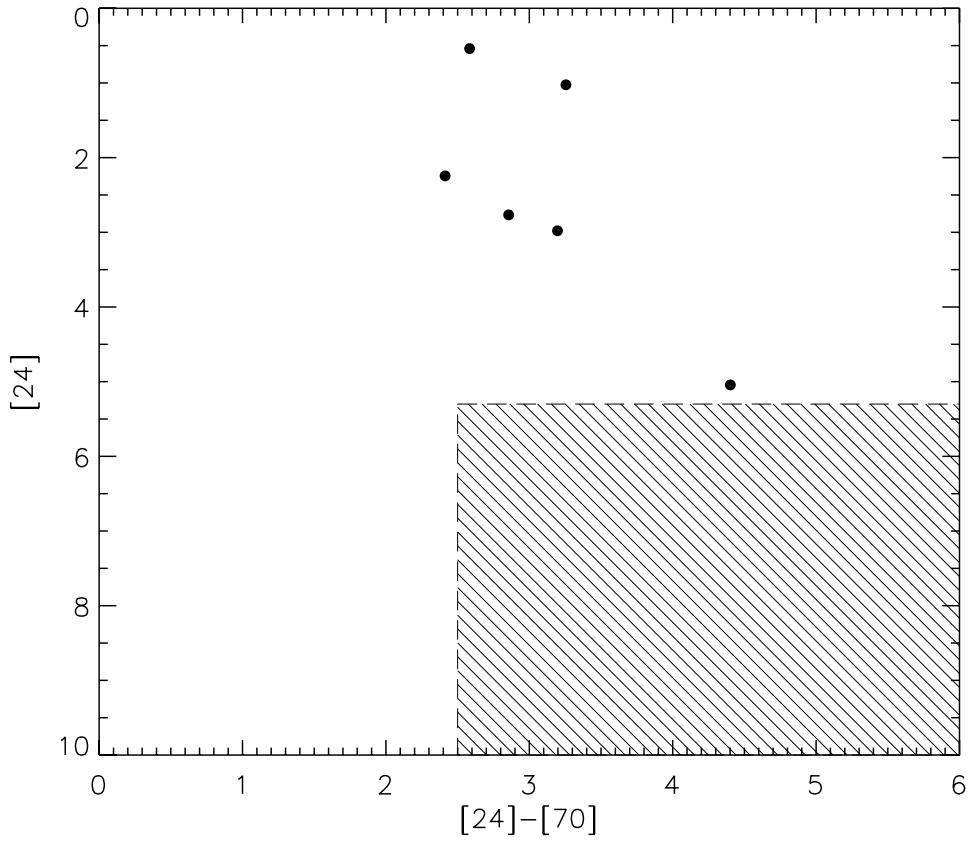

Figure 3.13: MIPS/Spitzer colour-colour diagram for the Ophiuchus members with detections at 70 μm. The dashed box delineates the colours from the comparison region from the extragalactic SWIRE field, used by Padgett et al. (2008) to separate YSOs from extragalactic sources.

3.6 X-ray variability

Strong magnetic fields are known to exist in T Tauri stars for about two decades now, when X-ray emission was for the first time detected in these stars (Feigelson & Decampli 1981; Montmerle et al. 1983). The X-ray emission in pre-main-sequence stars is $\sim 10^4$ times higher than that of the present-day Sun (e.g., Feigelson & Montmerle 1999). But while magnetic activity in main-sequence stars is relatively well understood, and can be described by a strong rotation-activity relationship (e.g., Pizzolato et al. 2003), not much is known regarding the origins of X-ray production in young stars. In particular, the role of accretion in X-ray production is still unclear, since on one side, energetic shocks associated with accretion could enhance X-ray production (e.g., Schmitt et al. 2005), but on the other hand, Preibisch et al. (2005) have suggested that the mass-loading of magnetic field lines can inhibit X-ray production in accreting systems.

Young stellar objects have been known to be highly variable in X-rays, so it is likely that the variable sources detected in this IR study have also shown variability behaviour in previous X-ray studies of the Ophiuchus molecular cloud (Montmerle et al. 1983). The coexistence of X-ray emission and photometric variability in young objects has already been observed. For example, Stassun et al. (2006, 2007) have conducted a simultaneous optical and X-ray variability study of the Orion Nebula Cluster to search for time-correlated variability, in a effort to disentangle the roles of magnetic and accretion activity in the production of X-rays. The authors have analysed over 800 pre-main-sequence stars' optical and X-ray light curves and find that the two forms of variability are not time-correlated (with very few exceptions, <0.5%), and show that the two are not causally related (see Fig. 3.14). Furthermore, their study shows that accretion is not a significant source of X-ray production in pre-main-sequence stars. The same result has also been found with an analogous survey of the Taurus region by Audard et al. (2007). Stassun et al. (2007) find that the strongest correlate of optical variability is X-ray luminosity, a relation they find to hold independently of the stars in their sample being accretors and non-accretors. The authors propose a possible scenario that would explain this correlation, suggesting that the primary source of X-ray production in PMS stars is a solar-analogue magnetic activity directly related to the spots on the star's surface, which would also be responsible for the observed variability both in the optical and X-ray. The fact that the variability is not correlated in time is interpreted as a scenario where the optical spots represent the footpoints of complex magnetic topologies that heat a solar-analogue coronae, responsible for most of the X-ray emission. This scenario has also been suggested by Jardine et al. (2006), who find that the dipole field model cannot explain all the different X-ray emission measurements from young stellar objects from recent deep X-ray surveys, and more complex configurations are needed. These are characterised by coronal gas that is confined to compact loops covering a large fraction of the stellar surface. This topology would produce coronal emission with a low X-ray luminosity due to its compact size (see Fig. 3.15), and the footprints of the multipolar field correspondently produce small spots, approximately uniformly distributed in the stellar surface, resulting in a low amplitude variation in the optical. The opposite is true for a more extended dipolar field where the coronal emission would produce higher X-ray luminosity and the small number of spots (the footprints) would be more asymmetrical distributed resulting in stronger optical variability.

As described in Sect. 3.2, ρ Ophiuchi has been the target of several X-ray surveys and many of the sources in our list of variable objects with confirmed membership have been detected in X-rays both with Chandra and XMM-Newton, namely by Imanishi et al. (2001), Gagné et al. (2004), and Ozawa et al. (2005), who have carried out in their studies a search for X-ray variability. Imanishi et al. (2001) used Chandra with an exposure time of 100ks, and detected ∼100 X-ray sources at a detection limit of 10^{28} ergs^{-1}. The authors consider a star as having flaring activity if it satisfies one of the two following criteria: (1) a constant flux hypothesis for the light curve

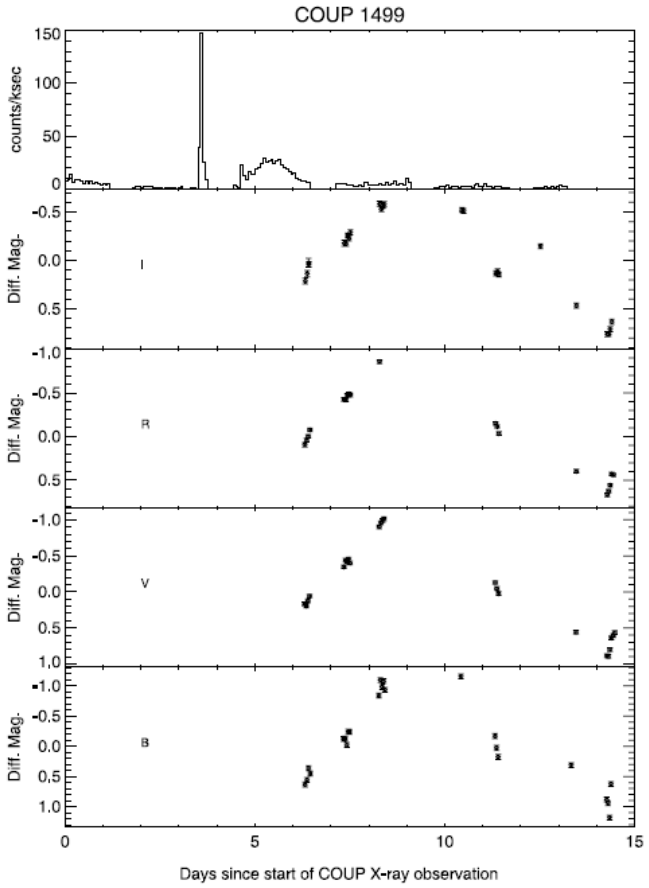

Figure 3.14: Light curves showing simultaneous optical and X-ray variability. Light curves for object COUP 1499 (Stassun et al. 2006) are shown, which is highly variable both in the optical and X-ray, but do not show any correlation in time.

is rejected using the chi-square fitting technique, (2) the X-ray flux increases and/or decreases by more than double the preceding/following flux with a timescale smaller than a few times 10^4s. From the sample of objects where they detect flares, 7 are also variable stars in our study. Also using *Chandra*, Gagné et al. (2004) observed a contiguous region in the sky to that of Imanishi et al. (2001) with an exposure time of 96ks, and detected 87 X-ray sources with approximately the same detection limit. The authors use the Kolmogorov- Smirnov (KS) statistic to look for variability, finding that all objects with KS>1 show light-curve variability, and stars with KS>2 undergo flaring activity. From their sample of X-ray variable objects, 10 overlap with our IR variables. Finally, in a more shallow survey done by Ozawa et al. (2005) using XMM-Newton, with an exposure time of 33ks, 11 flares were detected, one of them in a young star which is also found in our list of variables. In total, 17 from our variable members with X-ray detections show flaring activity or variable X-ray emission, and they will be addressed in Sect. 3.9.

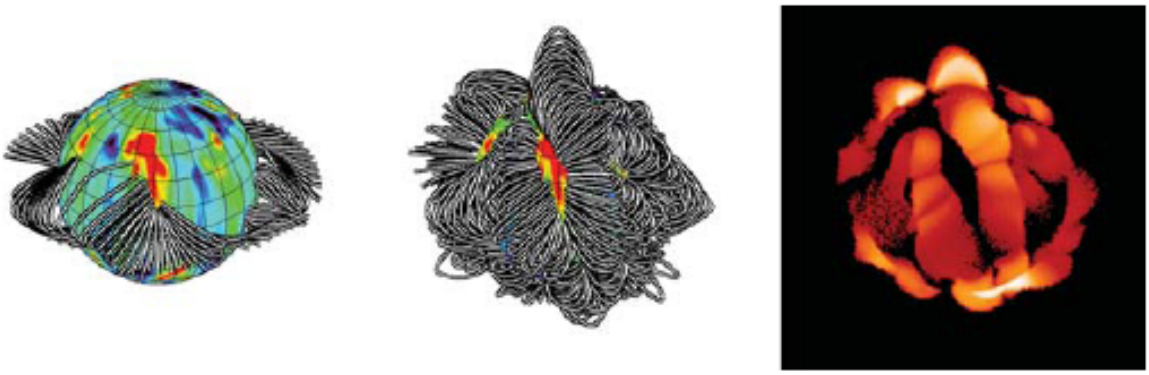

Figure 3.15: Model of a complex coronal structure (Jardine et al. 2006). From the left-hand side to the right, the panels show magnetic field lines which connect to the inner edge of an accretion disc (not shown) and can support an accretion flow, closed field lines containing X-ray emitting gas, and the corresponding X-ray coronal structure for this scenario.

3.7 Membership

The nature of the candidate member population is very important, since it determines the reliability of variability as an indicator of youth. In principle, some or all of the candidate members could be background objects – either variable stars within our own galaxy or extragalactic variable objects, principally Active Galactic Nuclei (AGN). An inspection of Fig. 3.16, however, shows that this is unlikely to be the case. The candidate members do not appear to be distributed in the same way as the majority of background point sources against which the clouds can be seen – they are noticeably absent from the regions of lowest extinction for example, and appear to be more clustered. To put this on a quantitative basis the 2-D Kolmogorov-Smirnov (K-S) test as outlined by Peacock (1983) was applied to candidate member and full point-source detection (non-variable) samples – the latter clearly dominated by the background population of stars and galaxies. The test is approximately distribution-free, which means the probability that the two samples are from the same population can be estimated. For 80 candidate member objects, a Z statistic of 1.99 was determined against the background distribution. Peacock (1983) gives a formula for calculating the significance level, which shows that there is an 2% chance that the two are from the same population. This is an upper limit since, for reasons already discussed, the variable candidate members lie outside the regions of high extinction, as do the background sources. This introduces an unavoidable spatial bias, making the two distributions look similar. The K-S test suggests the two populations come from different distributions. Of course this is for

the candidate population as a whole – there is still the possibility that a subset are due to contamination from background variable objects.

AGN are a potentially important source of contamination given the faint magnitude limits of the sample. The $K = 18.0$ limit amounts to 0.08 mJy at 3.6 μm assuming an SED median index of -1.2 (Buchanan et al. 2006). Treister et al. (2006) use a Spitzer survey of the GOODS field to estimate AGN number density versus flux in the IRAC bands. Their data show that this flux limit should result in approximately 300 AGN detections per sq. degree. However, central to understanding contamination by AGN is the distribution and magnitude of extinction in ρ Ophiuchi. Kenyon et al. (1998), in a study of the reddening law, find that in the clear areas well outside the molecular gas contours in areas of least extinction, the $H-K$ colour in most sources has only a small excess over intrinsic values – of order 0.2 in $H-K$. A similar excess is found in these data, corresponding to a visual extinction of 3-4 magnitudes. However, over much of the field the extinction is much higher. Therefore, for a proper evaluation, the number counts of K-band point sources was used to calculate K band extinction in a grid of 10 x 10 squares over the observed field. This was then used with the AGN cumulative flux distribution (Treister et al. 2006) to give the integrated number of AGN expected over the WFCAM field of view. After integrating over the extinction distribution a total of 33 AGN should be present in the ρ Ophiuchi field to the K band detection limit of 18.0. How many of these will be detected as variable? With the steep AGN cumulative flux distribution, more than 95% of the AGNs will lie in the faintest two magnitude bins, where the typical photometric error of the sample is 0.05-0.1 magnitudes. Simulations with the 2-band cross-correlation index show that a clear variability detection with this index requires an amplitude of at least > 0.13 magnitudes in this case. Enya et al. (2002) show that the fraction of AGN with long-term IR variability larger than this is $\sim$28% or 9 objects in the ρ Ophiuchi field, compared to the candidate-member sample of 80. So while a precise number is difficult to calculate, it is likely that a small (but still non-negligible) fraction of the variable candidate-members can be explained as AGN.

Another potential source of contamination is a population of background variable stars. The galactic model of Wainscoat et al. (1992) was used as a useful tool in investigating this. Even though discrepancies between observations and this model exist, it is certainly accurate enough (factor of 2) for the purposes here. Schultheis et al. (2000) conducted an unbiased survey of a region in the galactic bulge, and found 720 sources variable in J and K band, representing 0.2% of the source detections in the region. These were mainly long-period variables – AGB stars at or beyond the tip of the RGB. A similar fraction of variables in the ρ Ophiuchi field (16 000 sources) would predict 24 variables. However, the stellar populations are very different in the two fields. The bulge field is dominated by giants and includes many AGB stars; in fact the galactic model predicts a number of AGB stars comparable to the total number of variables detected in the Schultheis et al. (2000) study. But the high galactic latitude of the

ρ Ophiuchi field (+16.7) completely changes the result. Far fewer giants are expected, since the line of sight moves rapidly above the plane and bulge, so that the counts become dominated by the faint end of the dwarf luminosity function. At this latitude, the model predicts < 1 AGB star/long-period variable in the whole field of view. It seems clear that the ρ Ophiuchi variable sample should be completely uncontaminated by these objects.

It should be noted that in discussing the membership of any individual source, its location in the field is important, since any significant amount of extinction lowers the probability of background contamination substantially compared to the numbers calculated above.

Finally, the contamination of the variable candidates list by active M dwarfs is the most difficult to quantify. For variable stars fainter than $K\sim$15.5, objects which showed variability consistent with active M dwarfs have been excluded (see Sect. 3.1). The list of variable candidate members could still contain active M dwarfs brighter than that limit. In regions of high extinction (50 to 100 A_V), only foreground dwarfs could be detected as variables. The Besançon Galactic stellar population model[2] (Robin et al. 2003) predicts $\sim$10 M dwarfs/deg^2 in the foreground of the Ophiuchus region. Bochanski et al. (2005) have investigated the distribution of magnetically active M dwarfs in the solar neighborhood, up to a distance of $\sim$100 pc, and within the 2MASS magnitude limits ($K_s\lesssim$15). They find that out of their sample of 574 M dwarfs, a fraction of 27% are variable. Taking these results into account, it is likely that the contamination by foreground active M dwarfs is very small, of the order of $\sim$3 stars in a list of 80 candidate members. However, the number of M dwarfs dramatically increases in regions away from high extinction, and it becomes impossible to make an accurate estimate. Therefore, the properties of the variability are used, in analogy to Sec. 3.1, to point out which stars have variability consistent with active M dwarfs, together with no indication of IR-excess, or association with the known stellar population of the cluster. These amount to 30 stars, out of the 80 variable candidate members, which represents a fraction of possible contamination of $\sim$37.5%.

3.8 Understanding the Variability

The characteristics of the variability observed in young stars in ρ Ophiuchi are very diverse, spanning large ranges in magnitude, colour and timescale. Furthermore, given the limited information and finite measurement errors, it is not possible to conclude with certainty which physical mechanism is causing variability in each star. In fact, in many cases the variability observed in a particular star could be caused by a variety of mechanisms. So the following approach was used. Known or plausible physical

[2]The Besançon models are available on-line at bison.obsbesancon.fr/modele

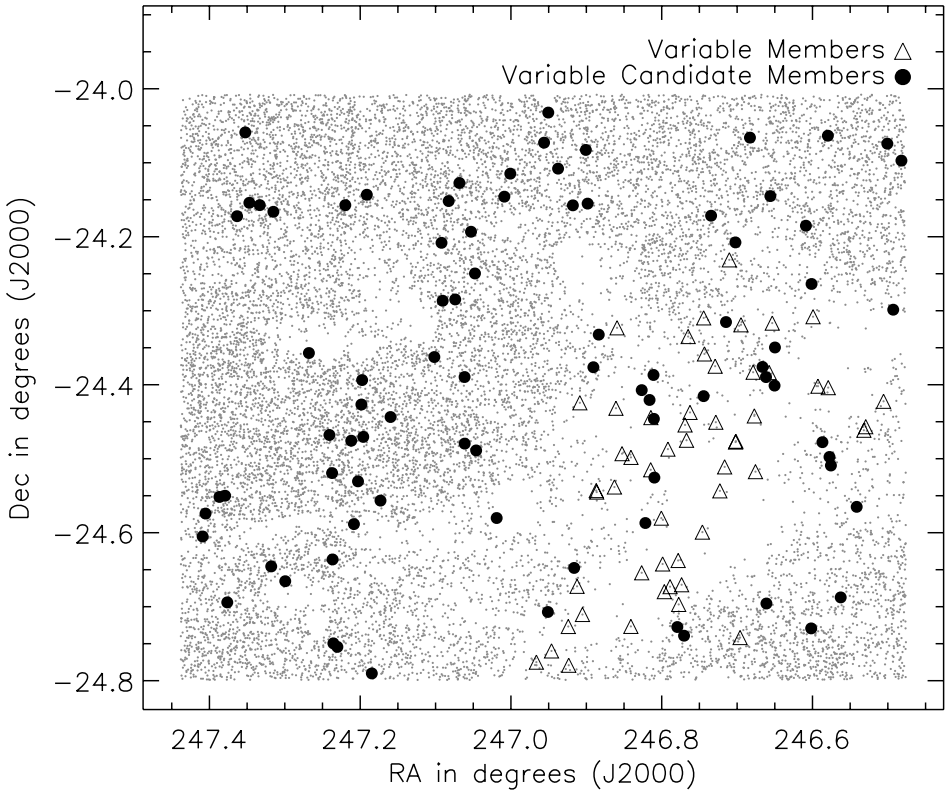

Figure 3.16: Spatial distribution for variable members of ρ Ophiuchi and variable candidates, with respect to all detected objects in the field.

mechanisms were considered in turn as the cause of variability in each star. Mechanisms which were considered plausible according to certain criteria were then listed in Table 3.3 for each star. In this way, an overall idea of whether the variability can be explained by conventional mechanisms, is obtained. A summary of the mechanisms, criteria and conclusions is as follows.

Rotational modulation by cool starspots

Cool starspots modulate the observed magnitude of a star, since as the star rotates the fractional spot coverage facing the observer is changed. They have temperatures that are colder than the star's photosphere (∼2000 K, e.g., Fernandez & Eiroa 1996) and arise from magnetic active regions, analogously to solar sunspots (Bouvier & Bertout 1989). In the classification scheme of Herbst et al. (1994), which is based on optical variability studies, stars which show low, periodic, amplitude magnitude variations (a few tenths of a magnitude) caused by cool spots are defined as type I. In a review of the rotation properties of young low mass stars and brown dwarfs, Herbst et al.

(2007) summarised the results from several variability surveys and concluded that the light modulations due to cool spots are present throughout a large mass range, including the substellar regime. This has been shown in photometric variability studies of very low mass stars and brown dwarfs that have identified similar behaviours (e.g., Scholz & Eislöffel 2005).

Detailed studies of several CTTSs and WTTSs have been done in the optical (Bouvier et al. 1993, 1995; Herbst et al. 1994), and for typical variability caused by cool spots in PMS stars, a fractional area coverage has been derived from the observed amplitudes of the order of 20% for a maximum amplitude of 0.4 mag (Herbst et al. 2002). Carpenter et al. (2001) have studied the characteristic amplitudes of variation caused by cool spots in the IR regime and derived a range of expected amplitudes based on the parameters inferred from optical studies. This can be done using a starspot model (Vrba et al. 1986) where the spot and the star are characterised by a single-temperature blackbody (with the respective temperatures), and the spot fractional coverage is taken into account. Carpenter et al. (2001) find that the expected amplitude colour variations produced by cool spots cannot exceed 0.05 magnitudes both in $J-H$ and $H-K$ colours. In the ρ Ophiuchi variable population, stars with amplitudes in H and $K < 0.4$ magnitudes and $H-K$ colour variations < 0.05 magnitudes therefore show variations consistent with the existence of cool spots , as defined by the above parameters, and are classified as CS (cool spots; see Col. 7, Table 3.3). Fig. 3.17 shows a star with variability characteristics consistent with cool spots. These amount to 18% of the variable members and 21% of the candidate members. Late-type field stars with magnetic activity could, however, still contaminate the group of candidate member variables (Sect. 3.7).

Rotational modulation by hot starspots

In analogy to the variability caused by cool starspots, hot spots cause magnitude variations in a star due to its rotation, which causes the spot area to move in and out from the visible part of the star. Hot spots have higher temperatures than the stellar photosphere ($\sim$8000 K, Carpenter et al. 2001) and are interpreted as the impact points on the stellar surface from disc accretion through magnetic field lines (e.g., Calvet & Hartmann 1992). Observationally, the main differences in variability caused by hot starspots, in relation to cool spots, are the amplitudes of the photometric fluctuations (larger colour variations are observed) and the timescales over which it persists, usually shorter than for cool spots (e.g., Kenyon et al. 1994). In the Herbst et al. (1994) classification scheme, objects showing larger amplitude variations (which can be irregular or periodic), from short-lived hot spots are called type II. Although the fraction of the stellar surface that hot spots cover is smaller than in cool spots, the high temperatures can cause larger amplitude variations.

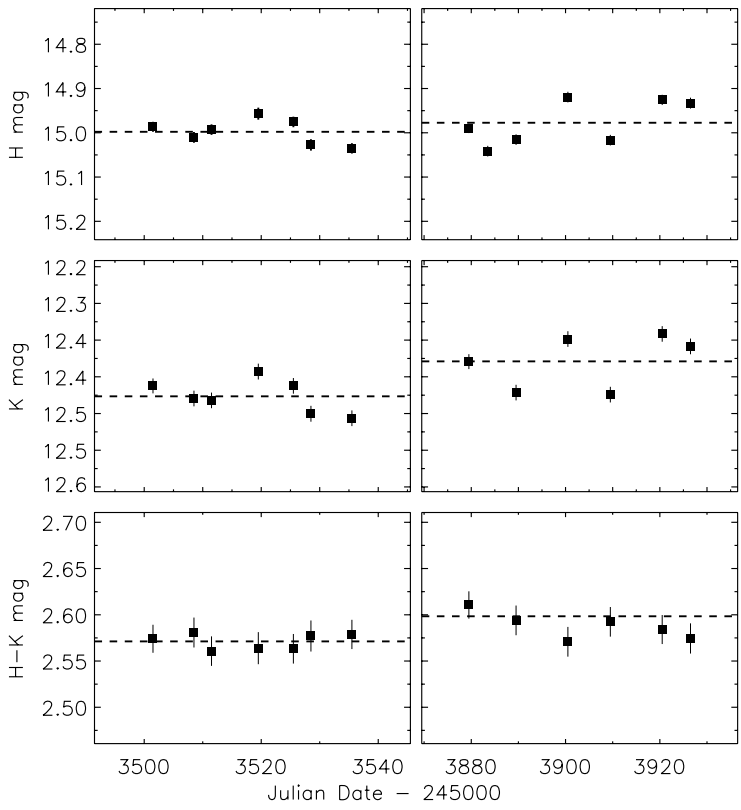

Figure 3.17: AOC J162724.63-242935.5; star with variability characteristics consistent with cool spots. The variability is seen across both years, in what looks like a periodic behaviour. The amplitude for the H and K band is of the order of ~ 0.12, and the changes in $H-K$ colour are < 0.05.

Using the same starspot models as explained above, Carpenter et al. (2001) derived for the near-IR regime the expected magnitude variations, which can be as high as 0.2-0.4 magnitudes for the *JHK* bands, and between 0.05-0.12 in the $J-H$ and $H-K$ colours. Given that the colour variations are substantial, Carpenter et al. (2001) use the information from the correlated colour and magnitude changes (see Sect. 3.4) to analyse the behaviour produced by hot spots. The predicted slope from hot spot models has high, positive values, although given the simplicity of their models, it is not possible to identify a specific range. Variable stars with amplitudes in H and $K < 0.4$ magnitudes, H and K colour variations between $\sim$0.05-0.12 magnitudes, and a positive slope in the colour-magnitude diagram (if a slope was determined) are classified as HS (hot spots). Hot spots can explain variability in 28% of the variable members and 30% of the candidate members. Figure 3.5 shown in Sect. 3.4, shows an example of a star with a variability behaviour that can be explained by rotational modulation by hot spots. The star shows no change in brightness during the first year of observations, but has large magnitude amplitude variations in the $\sim$2 months of the observations

during the second year (~ 0.34 in the H band, ~ 0.26 in the K band, and ~ 0.09 in $H-K$ colour). Also, the star's colour is redder when the star is fainter (i.e., has a positive slope in the K vs. $H-K$ colour-magnitude diagram).

Circumstellar Extinction

Variations in extinction can originate from the intersection with the line-of-sight of infalling or orbiting material in the circumstellar environment (Skrutskie et al. 1996). Circumstellar extinction variations will follow a reddening law if the grain size of the material is comparable to the interstellar grain size distribution (Skrutskie et al. 1996). The interstellar reddening law $\mathrm{E}(H-K)/A_K = 0.56$ was adopted from Rieke & Lebofsky (1985). In the K vs. $H-K$ diagram, this means that extinction variations can explain photometric slopes of $\sim 60°$, with the object being redder when it is faint. The histogram of the colour-magnitude slopes (Fig. 3.8) peaks at $45°-60°$, showing that variations in extinction can explain most of the observed positive slopes. Variable stars with positive slopes between 45° and 60° are classified as E (extinction). These represent 5% of the variable members and 4% of the variable candidate members.

Accretion Discs

Changes in the disc structure caused by mechanisms such as thermal instabilities, variable magnetic fields or warping instability can lead to near-IR variations on short timescales (see Carpenter et al. 2001, and references therein). Using simple disc models to study the consequences expected from geometric variations in a circumstellar disc, Carpenter et al. (2001) find that the observed negative slope in the colour-magnitude correlation (Fig. 3.8) can be explained by changes in the inner disc structure. This scenario has also been suggested by Eiroa et al. (2002). Furthermore, such a variability behaviour has never been observed in optical studies (Bouvier 2008, private communication), which also supports the hypothesis that the changes observed originate in a region disclosed only at IR wavelengths, such as the inner disc region. In a recent study of the classical T Tauri star AA Tau, Bouvier et al. (2007) used a long time series of high resolution spectra and simultaneous broad-band photometry to investigate the accretion and outflow dynamics on this nearly edge-on star. The authors find that the periodic light variations observed are due to the occultation of the central star by a magnetically-warped corrotating inner disk edge. This scenario could explain the variability observed in the IR in the cases where the star's colours become bluer when the star gets fainter. As the warped inner disc region moves out of the observers line-of-sight, the star-disc system becomes fainter in the IR since less light is being absorbed and reprocessed by the circumstellar disc. Discs radiate strongly at longer wavelengths, so when the warped inner disc region rotates out of the observed fraction of the star, the stellar colours become bluer, approaching its intrinsic colours.

Variable stars for which a negative colour-magnitude slope was found, where the star is bluer when faint, are classified as AD (accretion disc variations). In ρ Ophiuchi, 24% of the variable members and 25% of the variable candidate members have a negative slope, as defined in Sect. 3.4. However, if the colour variations are too small, the derived slopes could still be affected by photometric errors. Therefore, stars are only classified as having accretion disc variations if they show variations in colour with a 3σ confidence and derived slopes with inclinations <-10°. Only 16 variable stars satisfy these strict criteria and they will be discussed in Sect. 3.9.

Extreme variability

Although very rarely observed, another possible cause of variability related to accretion discs, is an FU Orionis type outburst. FU Orionis are a small class of young stellar objects which undergo large outbursts, during which their luminosity increases by several magnitudes, thought to have origin in phenomena related to a rapidly rotating inner accretion disc (e.g., Reipurth et al. 2007a, and references therein). AOC J162636.81-241900.2 (Fig. 3.18) has been previously classified as a member of ρ Ophiuchi. Its light curve reveals a brightening of several magnitudes (3.5 magnitudes in the K-band) in approximately one year, in what could be a FU Orionis type burst. However, a minimum in H and K magnitudes of 13.93 and 12.31, respectively, have previously been reported by Barsony et al. (1998), meaning this object could instead be an EXor, which are stars that undergo a maximum in magnitude once every few years, thought to be caused by the massive infall of circumstellar material onto the central star (see Herbig 2008, and references therein). A spectroscopy study of this variable member (classified as EV) is needed to better understand its nature.

Unexplained variability

There are 30% of the members and 28% of the candidate members which do not fit into any of the criteria defined above. Among the members, all have colours consistent with having IR-excess. However the majority does not show a linear correlation in the colour-magnitude variability diagram. The most likely explanation is that several physical processes are taking place simultaneously, and the variability observed is the combination of all the intervenients. This scenario is further supported by the fact that 4 of these variable members show a positive slope which is either too shallow or to steep to be explained by changes in extinction, and colours inconsistent with hot spots rotational modulation. The same is true for the only candidate member with a determined, positive slope, which has also been classified as Class II, but does not fit into the variability categories. All the other candidate members with unexplained variability did not show a linear correlation in the colour-magnitude variability diagram, and not all have IRAC/Spitzer detections. The other characteristic which is valid for these objects, both members and candidate members, is that the mean H and K amplitude

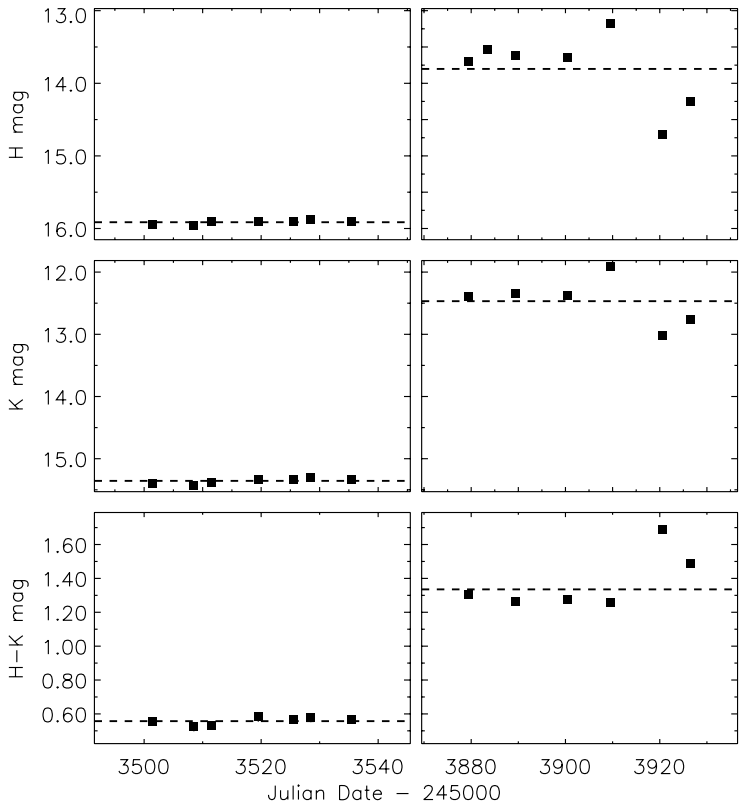

Figure 3.18: AOC J162636.81-241900.2; variable member with a brightening of several magnitudes in both H and K bands.

magnitudes, as well as the $H-K$ colour variations, are twice as large as the ones seen among other variables. Although this is in conformity with the scenario just described, it also opens the possibility that more extreme variability behaviours are, after all, common among young stars. Only targeted photometric and spectroscopic monitoring of variable stars of different types, looking for a correlation between colours, magnitudes, and spectral features would help in isolating the important physical mechanisms.

3.9 Variability properties and their relation with stellar parameters

Having established the main characteristics of the near-IR variability observed in the list of variables and analysing the possible physical origins, it is important to discuss how these relate to other stellar parameters such as the presence of an IR-excess, or the previous detection of X-ray variability in these stars.

From the 137 variable stars detected, 112 are present in the Spitzer catalogues. In Sect. 3.5, it has been shown that the combination of near- and mid-IR is an excellent tool to identify IR-excesses in young stars, which are an indication of the presence of a surrounding accretion disc. Accretion-related phenomena are observed not only in CTTSs, but also at the substellar regime. Analogously to CTTSs, very low mass stars and brown dwarfs also show accretion-related activity such as jets, variations in the continuum flux, and strong, variable line-emission (Mohanty et al. 2005; Scholz & Eislöffel 2005; Whelan et al. 2005).

A relation between the amplitude of the variations and the presence of IR-excess has been studied. Fig. 3.19 shows the peak-to-peak amplitude of the variability for the H-band versus K-band, for all the variable objects with detections in the Spitzer catalogues which showed an IR-excess (filled circles) or not (open squares). There are two main differences between the two groups. First, for the stars which did not show any IR-excess, the amplitudes of the variation do not exceed <0.4 magnitudes in both bands. This is consistent with the idea that cool spots alone can explain the variations seen in these stars, for which indication of circumstellar material has not been found. On the other hand, stars which have shown an IR-excess have amplitudes that can reach up to 1.0 magnitudes. This is more easily shown in Fig. 3.20, where it can be seen that as the H-band amplitudes increase, the corresponding near-IR colours are redder and also the fraction of stars with IR-excess increases. This trend suggests that the presence or absence of an accretion disc could be the main factor in dictating the observed amplitude of the photometric variations. Furthermore, the same relation as been observed between WTTSs and CTTSs in the near-IR study of the Orion Nebula Cluster by Carpenter et al. (2001). Finally, the second striking difference between the two groups in Fig. 3.19, is that most of the stars with IR-excess show a displacement in relation to the group with no IR excess, since for any ΔK, stars with IR-excess often show a higher ΔH than stars without IR-excess. This is in agreement with the existence of hot spots as the cause of variability in stars that show IR-excess, since it provides evidence for the spot temperature. As explained in the previous section, both hot and cool spots lead to amplitude modulation, which is larger at shorter wavelengths. However, given that the temperature of the hot spot is much higher, the increase in amplitude is steeper than for cool spots, which is what is observed in Fig. 3.19. This is easily explained if it is assumed that the star and spot can be described as a single-temperature blackbody. Then, the higher the temperature, the steeper the Planck curve becomes, affecting more shorter than long wavelengths. However, some of the sources in this diagram do not fall into either of these two groups, which seem to be well described by cool and hot spots, and instead show larger variations at the longer wavelengths. The majority of these sources have variability consistent with changes in an accretion disc, which ties well into the scenario described in the previous section.

In Sect. 3.6, 17 from the variable members have been found to have X-ray detections and to show flaring activity or variable X-ray emission. If IR-excess is used as

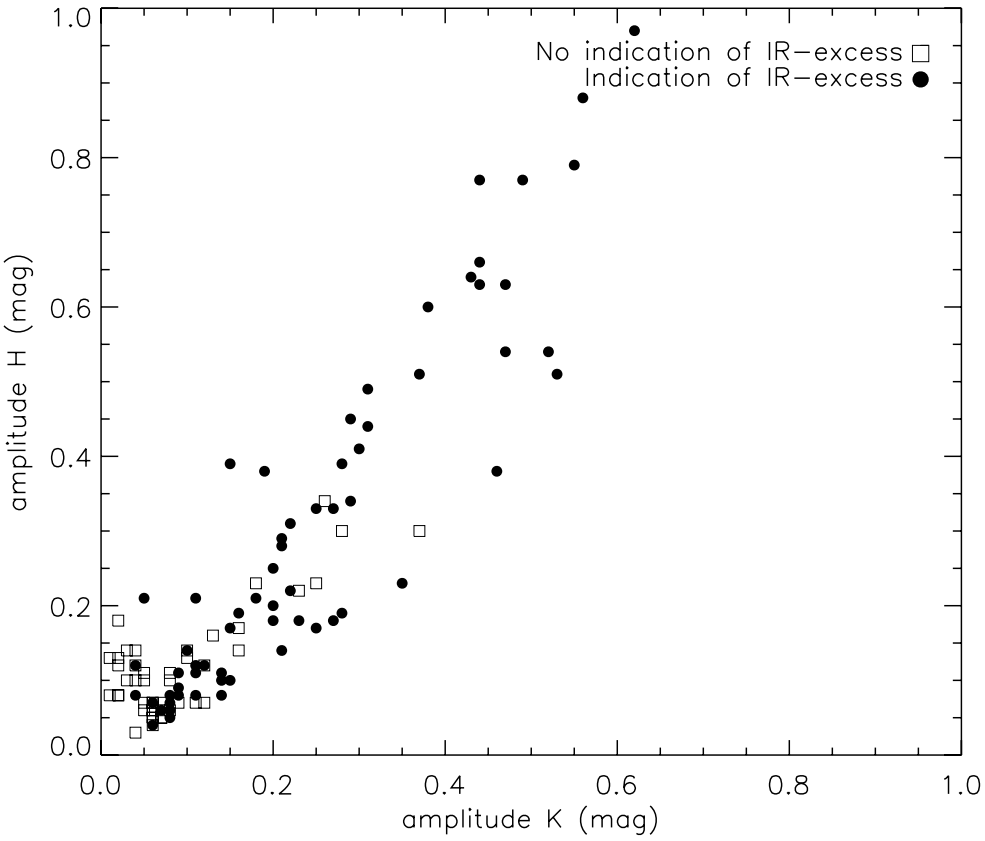

Figure 3.19: H-band versus K-band amplitudes of variability for stars which show an indication of IR-excess (filled circles) and stars that do not have an IR-excess (open squares).

a signature for the presence of an accretion disc, a rough comparison between X-ray activity and accretion can be made. However, some of these variable stars with X-ray variability show IR-excess, while others do not, and there is no clear relation between the two properties. This result agrees with the study of Stassun et al. (2007), where the authors claim they did not find a statistically significant difference in the level of X-ray variability among the accretors as compared to the non-accretors.

Finally, it is important to address the results for the variability properties in brown dwarfs. There are ∼22 brown dwarfs confirmed in ρ Ophiuchi (Wilking et al. 1997; Luhman & Rieke 1999; Cushing et al. 2000; Natta et al. 2002; Wilking et al. 2008) and all of them have counter-parts in the WFCAM catalogues. However, only 5 brown dwarfs are found to be variable according to the criteria used and detection limits. From these, 4 have low amplitudes both in H and K ($<$0.2) and only one shows high variability with amplitudes $\gtrsim$ 0.5. Caballero et al. (2004) studied photometric variability of 28 young brown dwarfs candidates in σ Orionis (∼3 Myr old) in the I-band and found amplitude variations ranging from less than 0.01 up to ∼0.4 magnitudes.

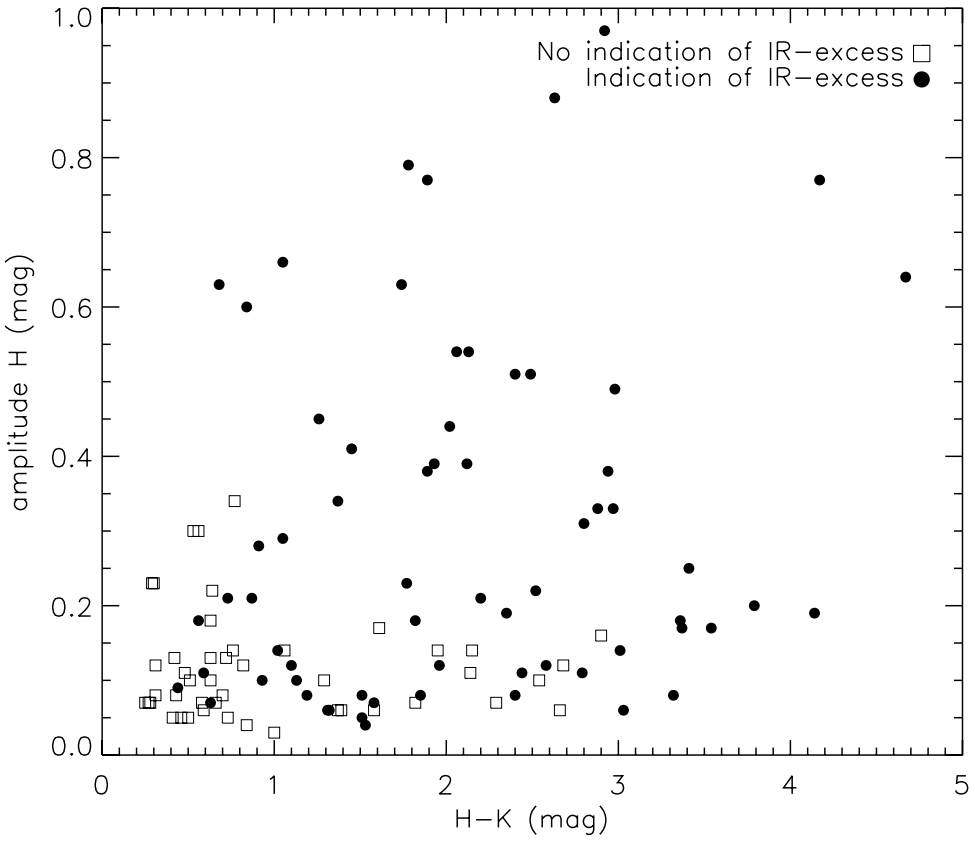

Figure 3.20: H-band amplitude versus H-K colour for stars which show an indication of IR-excess (filled circles) and stars that do not have an IR-excess (open squares). It can be seen that as the H-band amplitudes increase, the near-IR colours become redder and the fraction of stars with IR-excess increases.

It thus seems likely that the reason why all of the known brown dwarfs in Ophiuchus have not been detected as variables is sensitivity. However, the fact that these 5 BDs were found to be variables is extremely important, since it makes them good targets for a more detailed study and a search for periodic behaviour. In the substellar regime, the average period is seen to decrease with decreasing masses, extending down to the breakup period, the limit of the rotational velocity (Scholz & Eislöffel 2005). Stellar evolution is altered in presence of extremely fast rotation, for which the study of these objects is fundamental for evolutionary models of brown dwarfs (Herbst et al. 2007).

3.10 Chapter conclusions

A multi-epoch, very deep near-IR survey was conducted in the Ophiuchus molecular cloud with the WFCAM/UKIRT. Statistical methods, such as the reduced chi-square and correlation indices, were used in the search for variability, known to be a common characteristic of young stellar objects. 137 variable objects were found which show timescales of variation which can go from days to years, amplitude magnitude changes from a few tenths to $\sim$3 magnitudes, and colour variations of $\sim$0.2 magnitudes, in average. From the ρ Ophiuchi known population, 128 members have counter-parts in the WFCAM catalogue, and 45% are found to be variable. The dataset was merged with IRAC and MIPS/Spitzer observations to further extend the information about the detected variables and using colour-colour diagrams, an indication for the existence of IR-excess is found in 65 variable stars.

The variability trends found were interpreted in a physical context by comparison with previous suggested classifications for variability in the optical and near-IR. The characteristics observed are consistent with the existence of cool or/and hot spots on the stellar surface, variations in circumstellar extinction, or structural variations in accretion discs. However, a large fraction of the variable population does not fit into the predicted parameters for near-IR variability, which can be explained by the fact that the variability observed does not reflect a single event, but the net effect of several simultaneous processes.

Finally, in this near-IR variability survey, 80 variable stars have been uncovered which have not been previously associated with the stellar population of the ρ Ophiuchi cloud. These stars show characteristics similar to those of the cluster's variable members, and represent candidate pre-main-sequence stars of the cluster. To confirm the nature of these variable objects, a low-resolution near-IR spectroscopic follow-up has been conducted for a small sample and results will be present in the next chapter.

Table 3.3: Photometric Properties of the Variable Stars

AOC designation[1]	$<H>$[2] (mag)	$<K>$[2] (mag)	ΔH[3] (mag)	ΔK[3] (mag)	$\Delta(H\text{-}K)$[3] (mag)	Slope[4] (degrees)	IR-excess[5]	Variability[6,7]		Ref.[8]
J162555.67-240549.6	13.97	13.47	0.05	0.06	0.04	...	...	Y00Y	CS	...
J162558.29-241754.9	17.23	15.16	0.45	0.26	0.50	...	...	YYYY	...	...
J162600.16-240427.3	14.15	13.71	0.09	0.09	0.03	...	Y	Y0YY	CS	...
J162601.37-242520.4	12.30	11.04	0.45	0.29	0.17	54	Y	YYYY	E	2
J162607.03-242724.1	12.42	10.40	0.44	0.31	0.15	65	Y	YYYY	...	2,3
J162607.63-242741.4	11.88	10.27	0.17	0.16	0.06	...	...	YYYY	HS	2,3
J162609.92-243354.2	11.77	10.89	0.21	0.05	0.17	...	Y	YYY0	...	...
J162615.01-244114.8	15.19	14.31	0.31	0.26	0.22	...	...	YYYY	...	...
J162618.13-243033.1	12.98	11.67	0.06	0.08	0.04	-53	Y	Y0Y0	CS,AD	...
J162618.57-242951.4	15.13	13.55	0.07	0.08	0.07	...	Y	Y0Y0	HS	...
J162618.98-242414.0	14.28	12.15	0.54	0.47	0.18	...	Y	YYYY	...	1,2
J162619.10-240348.4	11.42	10.94	0.11	0.05	0.12	...	...	Y00Y	HS	...
J162620.83-242839.5	13.61	11.87	0.63	0.47	0.15	59	Y	YYYY	E	...
J162622.26-242407.0	14.83	13.69	0.10	0.14	0.05	-69	Y	YYY0	CS,AD	1,2
J162623.81-241829.0	14.59	13.49	0.12	0.04	0.08	20	Y	Y0Y0	HS	1
J162624.29-241549.7	15.81	13.65	0.14	0.16	0.03	...	...	YYYY	CS	...
J162624.41-244345.5	16.44	15.71	0.23	0.32	0.37	-36	...	YYY0	AD	...
J162626.08-241106.3	15.20	14.54	0.20	0.20	0.11	...	...	YYYY	HS	...
J162635.95-242058.7	15.99	13.59	0.51	0.53	0.31	...	Y	YYYY	...	...
J162636.07-242404.2	16.08	13.18	0.16	0.13	0.09	...	...	Y0YY	HS	...
J162636.81-241900.2	14.86	14.02	2.78	3.52	1.16	-72	Y	YYYY	AD,EV	2,3
J162637.41-240842.1	11.21	10.46	0.14	0.04	0.13	...	...	YYYY	...	...
J162637.78-242300.7	12.60	10.72	0.77	0.44	0.34	...	Y	YYYY	...	2
J162638.66-244144.4	14.96	14.15	0.09	0.10	0.10	...	...	Y00Y	HS	...
J162638.79-242322.8	12.84	11.52	0.06	0.07	0.04	...	Y	Y00Y	CS	2
J162639.92-242233.5	14.69	13.49	0.08	0.04	0.06	...	Y	Y00Y	HS	6
J162642.14-243103.0	13.68	11.05	0.88	0.56	0.36	...	Y	YYYY	...	2
J162642.51-242631.7	15.63	12.60	0.06	0.08	0.05	...	Y	Y0Y0	HS	1,2,3
J162642.89-242259.1	12.91	11.37	0.04	0.06	0.03	...	Y	Y0Y0	CS	2,3
J162643.90-240357.8	16.28	15.69	0.19	0.16	0.33	-24	...	Y00Y	AD	...
J162646.76-241908.4	11.68	10.29	0.06	0.07	0.05	...	...	Y0Y0	CS	3
J162647.05-244430.0	11.20	10.56	0.10	0.03	0.11	...	...	Y0YY	HS	2,4,5
J162648.39-242834.8	15.24	12.46	0.11	0.09	0.07	...	Y	Y00Y	HS	2,3
J162648.48-242838.9	14.07	11.09	0.49	0.31	0.21	...	Y	YYYY	...	1,2,3
J162648.53-241227.5	11.84	10.55	0.10	0.08	0.05	...	...	Y0YY	HS	...
J162650.47-241352.3	11.32	10.81	0.10	0.04	0.11	...	...	Y00Y	HS	5
J162651.52-241855.1	17.39	15.80	0.52	0.28	0.47	...	...	Y0Y0	...	...
J162651.97-243039.6	16.55	13.23	0.08	0.11	0.06	-57	Y	Y0YY	AD	1,2,3
J162653.48-243236.2	16.93	13.15	0.20	0.20	0.16	...	Y	YY0Y	...	1,2,3
J162654.77-242702.3	14.97	12.77	0.21	0.18	0.11	...	Y	YYYY	HS	2
J162654.98-242229.7	11.92	10.11	0.07	0.06	0.06	...	...	Y0YY	HS	2,3
J162656.27-241017.6	14.91	14.09	0.12	0.12	0.04	...	...	Y0YY	CS	...
J162658.39-242130.2	13.18	11.37	0.18	0.20	0.08	...	Y	YYYY	HS	2,3
J162658.64-241834.8	13.13	11.61	0.05	0.08	0.04	-63	Y	Y0Y0	CS,AD	2,3
J162658.65-242455.5	17.02	14.50	0.22	0.22	0.08	...	Y	YYYY	HS	...
J162659.04-243556.9	13.87	11.99	0.38	0.19	0.20	42	Y	YYYY	...	1,2
J162702.99-242614.7	15.83	12.42	0.25	0.20	0.11	...	Y	YYYY	HS	2,3
J162703.58-242005.5	14.88	13.51	0.34	0.29	0.21	...	Y	YYYY	...	2
J162704.10-242829.9	13.12	10.77	0.19	0.16	0.15	...	Y	YYYY	...	1,2,3
J162704.57-242715.6	13.22	11.10	0.39	0.28	0.17	47	Y	YYYY	E	2,3
J162704.88-244421.2	15.72	14.90	0.11	0.08	0.09	...	...	Y0YY	HS	...
J162705.66-244013.1	16.81	13.81	0.14	0.10	0.09	...	Y	Y0Y0	HS	2
J162706.59-244148.9	11.43	10.71	0.21	0.11	0.22	...	Y	YYYY	...	2,4,5
J162706.76-243815.1	14.19	11.25	0.38	0.46	0.13	-70	Y	YYYY	AD	1,2,4
J162707.02-244338.9	15.61	14.61	0.03	0.04	0.05	-39	...	0Y0Y	AD	...
J162709.34-244022.5	13.72	11.32	0.08	0.14	0.07	-61	Y	YYYY	AD	2
J162710.02-242913.3	15.21	14.16	0.29	0.21	0.10	...	Y	YYYY	HS	1
J162711.16-244046.7	13.47	10.55	0.97	0.62	0.52	...	Y	YYYY	...	2
J162711.71-243832.1	15.10	10.93	0.77	0.49	0.36	40	Y	YYYY	...	1,2,4
J162712.12-243449.1	13.09	11.32	0.79	0.55	0.27	58	Y	YYYY	E	2,4
J162714.34-243131.9	16.65	15.20	0.41	0.30	0.15	57	Y	Y0YY	E	...
J162714.49-242646.0	15.46	12.08	0.17	0.25	0.19	-55	Y	YYY0	AD	2
J162714.61-242312.6	16.65	15.14	0.12	0.22	0.15	-51	...	YYY0	AD	...
J162715.44-242639.8	13.43	10.55	0.33	0.25	0.24	...	Y	YYYY	...	4
J162715.50-243053.8	16.49	12.35	0.19	0.28	0.16	-53	Y	YYYY	AD	2
J162715.87-242514.1	16.12	13.15	0.33	0.27	0.11	61	Y	YYYY	HS	2
J162717.19-243512.8	16.59	14.65	0.14	0.03	0.15	...	...	Y00Y	...	...
J162718.36-242426.3	13.34	11.20	0.11	0.08	0.07	...	...	Y0YY	HS	...
J162718.37-243914.8	15.60	12.05	0.17	0.15	0.07	...	Y	YYYY	HS	1,2,4
J162721.78-242953.4	15.18	10.51	0.64	0.43	0.41	40	Y	YYYY	...	1,2,4
J162721.81-244335.8	13.40	10.74	0.06	0.06	0.03	...	...	Y0YY	CS	2,4
J162724.63-242935.5	14.99	12.40	0.12	0.11	0.05	...	Y	YYYY	CS	1,4
J162726.22-241923.1	14.42	12.91	0.08	0.09	0.08	-46	Y	Y0YY	AD	2
J162726.57-242554.4	12.33	11.77	0.18	0.23	0.10	-66	Y	YYYY	AD	5
J162727.06-243217.6	14.59	12.30	0.07	0.07	0.05	-47	...	Y0Y0	CS,AD	4
J162732.05-241956.3	17.21	15.47	0.18	0.06	0.17	...	...	Y00Y	...	...
J162732.70-243242.4	15.49	13.00	0.51	0.37	0.28	...	Y	YYYY	...	2
J162732.84-243234.9	12.86	10.90	0.12	0.12	0.09	...	Y	YYYY	HS	2,4
J162733.75-242234.9	16.49	15.66	0.60	0.38	0.28	52	Y	YY0Y	E	...
J162735.58-240918.7	14.85	14.11	0.05	0.07	0.04	-62	...	Y0Y0	CS,AD	...
J162736.14-240457.7	12.97	12.06	0.28	0.21	0.09	...	Y	YYYY	HS	...
J162737.23-244237.9	14.77	11.41	0.18	0.27	0.17	-58	Y	YYYY	AD	2
J162738.06-242527.8	15.37	12.70	0.12	0.04	0.09	20	...	Y00Y	HS	...
J162738.95-244020.7	14.19	12.42	0.23	0.35	0.14	-63	Y	YYYY	AD	2,4

Table 3.3: continued.

AOC designation[1]	$<H>$[2] (mag)	$<K>$[2] (mag)	ΔH[3] (mag)	ΔK[3] (mag)	$\Delta(H\text{-}K)$[3] (mag)	Slope[4] (degrees)	IR-excess[5]	Variability[6,7]		Ref.[8]
J162739.88-243851.3	15.41	14.06	0.05	0.06	0.04	...	...	Y0Y0	CS	...
J162740.28-240927.2	14.47	13.63	0.04	0.06	0.04	-56	...	Y0Y0	CS,AD	...
J162741.60-244644.8	15.78	13.84	0.39	0.15	0.32	...	Y	YYYY	...	2
J162741.74-244336.2	14.69	11.88	0.31	0.22	0.12	...	Y	YYYY	...	2
J162744.98-240628.6	11.78	10.74	0.66	0.44	0.47	...	Y	YYYY	...	...
J162747.08-244535.1	12.94	11.09	0.08	0.08	0.04	...	Y	Y0YY	CS	2,4
J162748.11-240155.9	16.49	15.90	0.48	0.38	0.72	...	...	0YYY	...	...
J162748.24-244225.6	16.92	14.86	0.54	0.52	0.18	...	Y	YYYY	...	...
J162749.45-240422.2	14.19	13.61	0.07	0.05	0.04	...	...	Y00Y	CS	...
J162751.90-244629.7	11.82	10.45	0.06	0.06	0.04	...	...	Y0YY	CS	2,4
J162800.20-240653.0	13.64	13.05	0.06	0.08	0.03	...	...	Y0YY	CS	...
J162802.10-240844.9	16.03	15.38	0.26	0.25	0.11	...	...	YYYY	HS	...
J162804.54-243448.6	15.11	12.67	0.11	0.14	0.08	-54	Y	YY0Y	AD	...
J162811.08-242919.7	11.26	10.63	0.18	0.02	0.18	...	...	YYYY	...	...
J162811.46-241458.7	15.88	15.28	0.10	0.11	0.07	...	...	Y0Y0	HS	...
J162812.71-241135.7	12.09	11.07	0.14	0.21	0.14	-45	Y	Y0YY	AD	2
J162814.72-242846.5	15.36	14.99	0.58	0.65	0.97	-31	...	YYYY	AD	...
J162814.76-242322.5	11.18	10.40	0.34	0.26	0.09	...	...	YYYY	HS	...
J162816.41-240738.4	14.24	13.52	0.13	0.10	0.10	...	...	YYYY	HS	...
J162817.73-241705.1	13.23	12.30	0.10	0.15	0.06	-61	Y	Y0YY	AD	...
J162819.82-240906.3	12.42	11.89	0.30	0.37	0.47	-35	...	YYYY	AD	...
J162821.73-241711.3	17.20	16.63	0.28	0.34	0.47	-33	...	Y00Y	AD	...
J162822.10-241229.6	16.69	15.96	0.32	0.33	0.41	...	...	0YY0	...	...
J162824.38-242145.3	14.93	14.34	0.11	0.11	0.03	...	Y	Y0YY	CS	...
J162838.34-242637.0	11.12	10.70	0.13	0.02	0.14	...	...	YY0Y	...	...
J162841.53-243323.8	11.13	10.69	0.08	0.02	0.09	...	...	YY0Y	HS	...
J162844.28-244724.7	15.92	15.42	0.17	0.16	0.06	...	...	Y0YY	HS	...
J162845.88-240835.6	13.98	13.33	0.22	0.23	0.15	...	...	YYYY	...	...
J162847.02-242813.9	12.74	12.07	0.63	0.44	0.21	65	Y	YYYY	...	...
J162847.38-242337.2	14.17	13.91	0.07	0.11	0.05	-65	...	Y0Y0	CS,AD	...
J162847.61-242536.3	12.92	12.64	0.07	0.12	0.05	-64	...	Y0Y0	AD	...
J162848.69-243150.1	14.34	14.04	0.23	0.18	0.09	...	...	YYYY	HS	...
J162849.98-243518.1	12.44	10.85	0.06	0.05	0.03	...	...	Y0YY	CS	...
J162850.84-242832.3	11.77	11.46	0.08	0.02	0.08	...	...	Y0Y0	HS	...
J162852.73-240926.2	15.67	15.01	0.07	0.09	0.05	...	...	Y0Y0	HS	...
J162855.25-244515.6	17.87	17.33	0.82	0.36	0.89	...	...	YYYY	...	...
J162856.53-244458.3	17.75	17.30	0.53	0.55	0.72	-35	...	Y0YY	AD	...
J162856.79-243810.1	11.16	10.53	0.13	0.01	0.14	-4	...	YYYY	AD	...
J162856.94-243109.8	11.51	10.88	0.07	0.06	0.04	...	Y	Y0Y0	CS	...
J162857.78-242804.6	11.08	10.77	0.12	0.02	0.13	...	...	YYYY	...	...
J162904.32-242125.7	16.49	13.95	0.10	0.05	0.06	...	...	Y00Y	HS	...
J162911.85-243955.9	16.38	15.32	0.14	0.10	0.09	...	...	Y0YY	HS	...
J162915.63-240958.5	16.94	16.26	0.32	0.25	0.43	...	...	YYYY	...	...
J162916.32-243844.0	14.04	13.49	0.30	0.28	0.03	82	...	YYYY	CS	...
J162919.97-240926.3	14.69	14.28	0.05	0.06	0.02	-67	...	Y0Y0	CS,AD	...
J162923.28-240914.9	13.97	13.51	0.05	0.07	0.07	...	...	Y0Y0	HS	...
J162924.58-240332.4	14.48	14.08	0.14	0.08	0.07	42	...	Y00Y	HS	...
J162927.18-241020.0	17.06	16.61	0.25	0.45	0.53	-35	...	YY0Y	AD	...
J162930.31-244139.0	11.25	10.55	0.08	0.01	0.09	-7	...	Y00Y	AD	...
J162931.01-243300.1	15.47	15.24	0.12	0.14	0.15	...	...	Y0Y0	...	...
J162932.80-243305.9	11.17	10.90	0.07	0.06	0.03	...	...	Y0YY	CS	...
J162937.23-243426.8	14.19	13.90	0.23	0.25	0.21	...	...	YYYY	...	...
J162938.15-243618.4	17.21	16.87	0.41	0.32	0.49	...	...	YY0Y	...	...

[1] J2000.0 IAU designation.

[2] Average magnitude over all available epochs.

[3] Peak-to-peak magnitude amplitude variation.

[4] Slopes in the colour-magnitude diagram K vs. $H-K$. See Sect. 3.4 for details.

[5] Evidence for IR-excess as defined from the combination of IRAC and MIPS/Spitzer and WFCAM/UKIRT data (Y). See Sect. 3.5 for details.

[6] First digit: star identified as variable from the CC indexes; second digit: star identified as variable from the χ^2_ν statistics; third digit: star is variable in year 1; fourth digit: star is variable in year 2 (a star is a long term variable when both these digits are Y). When each of these conditions is verified it is denoted by Y (as in yes), otherwise the digits are set to 0.

[7] CP = cool spots; HT = hot spots; E = extinction; AC = accretion discs; EV = Extreme Variability. See Sect. 3.8 for details.

[8] ρ Ophiuchi members, according to the following studies: 1. Comeron et al. (1993); 2. Bontemps et al. (2001); 3. Gagné et al. (2004); 4. Ozawa et al. (2005); 5. Wilking et al. (2005); 6. Strom et al. (1995).

Chapter 4

Spectroscopic follow-up of variable candidate-members

A robust list of variable stars has been established, extracted from thousands of detections in an area covering $\sim$0.8 deg^2 of the ρ Ophiuchi cluster. It is the objective of this section to investigate that this photometric technique is indeed effective in identifying young pre-main-sequence stars. In Sect. 3.7, I have studied the possible sources of contamination of the list of variables and it has been shown that, for the candidate members, only a statistical estimate can be obtained concerning their membership. Their positions in the colour-magnitude diagram K vs. $H-K$, and also the WFCAM/IRAC/MIPS colour-colour diagrams (Sect. 3.5), are indicative of their nature. However, magnitudes and colours are dependent on several factors such as mass, age, distance, extinction, and the presence, or not, of a circumstellar disc. Without knowing these parameters, it is not possible to assess membership of stars solely using photometry. Thus, a spectroscopic follow-up is needed to obtain information on the spectral types and ages of the variable candidate members. By combining low-resolution IR spectroscopy with photometric information, I will investigate the pre-main-sequence nature of a sample of candidate members.

4.1 The observing plan and proposal

Cluster membership of very low-mass young objects (from low-mass PMS stars, to brown dwarfs and planetary mass objects) has been confirmed by optical and near-IR low-resolution spectroscopy studies in several star-forming regions (e.g., Lucas et al. (2001), Barrado y Navascués et al. (2001), Martín et al. (2001), Jayawardhana & Ivanov (2006), Lucas et al. (2006), Allers et al. (2007)). In the optical, there are several relevant spectral features that can be used in spectral type classification and as an indicator of youth: the alkali elements (K_I λ7665 and λ7699 $\AA$, Na_I λ8183 and λ8195 $\AA$, Cs_I λ8521 and λ9843 $\AA$, and Rb_I λ7800 and λ7948 $\AA$), the molecular absorptions of TiO, FeH, CrH, and of VO and H2O (see Kirkpatrick et al. 1999, for detailed char-

acterisation of M and L field very low mass stars and brown dwarfs). Martín et al. (1999) developed a scheme to assign spectral types based on ratios of the average flux within particular wavelength regions of the spectra for field, old objects, which usually have surface gravity log g $\gtrsim$ 5.5. These scheme is frequently used to determine spectral types also in young objects (see, for example, Barrado y Navascués et al. 2001), for which evolutionary models predict surface gravities of 3.5 $\lesssim$ log g $\lesssim$ 4.0 (Allard et al. 2001). Young objects have larger radii than older stars since they are still contracting towards the main-sequence, having therefore a lower gravity. The effect of low gravity is seen in the strength of the alkaline lines, in particular Na I and K I, which are seen in old L-type field dwarfs but less intense in young L-type dwarfs (Barrado y Navascués et al. 2001). This provides a good indication of youth for the L spectral class. The dominant spectral features in the optical spectra of M dwarfs are the absorption bands from TiO and VO, which are very temperature sensitive, and therefore good indicators for spectral type classification. In M dwarfs the Na I doublet lines are strong in absorption, while much weaker for M-type young stars, thus providing a reliable signature of youth (Riddick et al. 2007). Finally, one of the most used indicators of youth, and thus membership, in optical spectroscopy of young objects is the existence of Hα (λ6563 $\mathring{A}$) in emission, which arises in magnetospheric accretion columns (Hartmann et al. 1994). However, optical spectroscopy of low-mass young stars and brown dwarfs is difficult to obtain since few of them have optical counterparts and are usually very faint due to extinction. Moreover, some of the described optical spectral features need high signal-to-noise ratio, which is difficult to obtain in faint objects, further restricting the use of this technique.

Spectroscopy of young objects in the near-IR regime can also be used to separate them from field stars and brown dwarfs, even at low resolution. As summarised by Allers et al. (2007), the spectral differences across the *J, H, K* are manifold. The *J* band spectra of field M dwarfs is marked by absorption of H_2O, VO, FeH, NaI, and KI. In young objects, the H_2O and VO absorption is deeper than in field dwarfs, while the NaI feature is weaker. In the *H* band, young stars and BDs show a peaked spectrum, while the field dwarfs have usually a plateau. Another characteristic is that young objects show a deeper H_2O absorption at the short wavelength of the *H*-band. The study of H_2O features has the advantage of them being broad, therefore requiring only moderate signal-to-noise ratios ($\sim$10). Finally, a triangular shape of the *H*-band has been reported in several studies as characteristic in young brown-dwarfs (Lucas et al. 2001; Kirkpatrick et al. 2006), although the cause of it is not entirely understood (Sect. 4.3). In the *K*-band, the NaI absorption line is strong in field dwarfs but very week in young objects.

I was co-investigator of a proposal to use ESO telescopes (in Period 79A) to carry out a spectroscopic follow-up for selected variable candidate members, entitled *"The nature of a new population of low-luminosity objects in the ρ Ophiuchi cluster"*. Telescope time allocated through a competitive process amount to two observing nights

in visitor mode, to use the low-resolution spectrograph part of *Son of Isaac* (SofI) at the New Technology Telescope (NTT). The initial proposal included targets that were selected using the results of the preliminary analysis done with the first part of the WFCAM dataset, i.e., the 7 epochs from 2005, since at the time the WFCAM observations were still not completed. After the submission date, but prior to the observations, the WFCAM observations were completed, and the full dataset was used to define a more robust list of candidates members, as presented in 3.1. The sample of candidate members chosen for spectroscopic observations was selected using the following criteria: variability (as defined in 3.1) detected across the two years of observations (for maximizing the likelihood of observing a highly active star, a defining characteristic of pre-main-sequence stars); relatively blue H-K colours, < 1.5 magnitudes, to minimise the contamination of light scattered by circumstellar material and/or increase the sensitivity given the lower extinction values. Although some of the selected sources were present in other source tables of previous surveys, they did not possess characteristics which enable them to be classified as young cloud members, rather than background stars or galaxies. The main objective of the proposal was therefore to clarify the nature of these objects, by trying to confirm their youth and also to determine their spectral type, fundamental parameter in calibrating the temperature from which the mass of the objects can be derived.

4.2 Observations and Data reduction

All the observations were done with SofI at the NTT, La Silla, in visitor mode. I have prepared all the observations using the ESO P2PP tool (Phase 2 Proposal Preparation) and was co-observer on the telescope run on May 22, 23, 2007. SofI (Son of ISAAC) is an IR imaging camera and spectrograph mounted on the Nasmyth A focus of the NTT, offering, among other observing modes, low resolution spectroscopy. The observations were done using long slit spectroscopy, with a slit width of 1" to match the seeing. The low resolution red grism was chosen for the observations, since it covers the wavelength range from 1.53 to 2.52 μm, important to study water absorption features. Observing in the IR brings several complications regarding the sky background, which compared to the optical regime shows stronger atmospheric absorption features (due to water vapour and carbon dioxide in the atmosphere) and stronger telluric emission. Several techniques have been developed to mitigate these problems in IR observations. The strategy used to assure accurate sky cancellation consisted of observing the same object at different slit positions (feasible if the object is small enough, which is the case for our sources). The telescope nods the object between two positions along the slit which were, for these observations, 60 arcseconds apart. Then, the sky contribution is efficiently cancelled when the two slit positions are subtract from each other. According to the NTT convention, these positions are called A and B, and together define one cycle, which can then be repeated. Table 4.1 shows for each object (AOCS-1 to

Table 4.1: SofI observations.

AOCS	AOC Designation	Date	Ndit x AB Cycles x Exp.time (s)
1	J162816.41-240738.4	23 May 2007	4 x 2 x 60
2	J162736.14-240457.7	23 May 2007	4 x 1 x 60
3	J162812.71-241135.7	23 May 2007	4 x 1 x 60
4	J162626.08-241106.3	23 May 2007	4 x 4 x 60
5	J162624.41-244345.5	23 May 2007	4 x 8 x 60
6	J162802.10-240844.9	23 May 2007	4 x 8 x 60
7	J162916.32-243844.0	23 May 2007	4 x 8 x 60
8	J162718.36-242426.3	24 May 2007	4 x 3 x 60
9	J162845.88-240835.7	24 May 2007	4 x 8 x 60
10	J162824.38-242145.3	24 May 2007	4 x 4 x 60
11	J162656.27-241017.6	24 May 2007	4 x 4 x 60
12	J162920.92-241936.8	24 May 2007	4 x 8 x 60
13	J162714.34-243131.9	24 May 2007	4 x 8 x 60
14	J162911.85-243955.9	24 May 2007	4 x 8 x 60
15	J162814.76-242322.5	24 May 2007	4 x 2 x 60
16	J162648.53-241227.5	24 May 2007	4 x 2 x 60

16, the naming follows the convention from Alves de Oliveira & Casali (2008), AOC, adding an S to differentiate the 'Spectroscopic follow-up') the summary of the log of observations, with the integration times for the individual spectra. Near-IR standard stars have also been observed (see Table 4.2) before and after each science target, using the same instrument set-up. The standards stars are then used to remove the time varying and air-mass dependent atmospheric absorption features.

Table 4.2: SofI observations of standard stars.

Near-IR standard	Spectral Type
hip82756	F0V
hip81617	F0V
hip79268	F0V
hip78374	F0V
hip77742	F0
hip68127	F0
hip69568	M2III
hip67830	M4III

The data reduction was done using standard IRAF[1] routines. The first step was to create a *master flat*. Flat fields were taken with the dome flat field screen, and a

[1]IRAF (Image Reduction and Analysis Facility), is a software system for reduction and analysis of astronomical data.

flat field is obtained by subtracting the image with the dome lamp off from an image with the dome lamp on (using the routine *imarith*). The flats are then combined into a *master flat* (using *imcombine*). For the science targets, As and Bs are added separately (only within a maximum of two cycles), subtracted one from the other (for sky subtraction), and the result divided by the *master flat*. The output is then multiplied by (-1) to obtain the inverse spectrum. The routine *twodspec - apextract - apall* is used to extract both spectra, which are then wavelength calibrated using an arc. For this purpose, the Xenon lamp was used as recommended for calibration of spectra taken with the red low resolution grism. The wavelength calibrated 1-dimensional spectra that were extracted from the 2-dimensional images are finally combined, to produce the final spectrum.

At this point, the telluric emission lines have been removed but spectrum of each target is still not ready for analysis since it is dominated by telluric absorption features. To remove these absorption features, standard stars from the Hipparcos Catalogue with spectral type F0 have been observed, chosen for having an almost featureless spectrum (apart from a few hydrogen lines). These were chosen in order to have similar airmass to that of the target being observed. The telluric standards' observations were taken at lower and higher airmasses than the target, and averaged with appropriate weights to give the closest airmass possible to that of the targets. Then, the target spectrum is divided by the telluric standard, which will remove the atmospheric absorption features, since they affect both spectra in the same way. Finally, the target spectrum is multiplied by the true intrinsic spectrum of a reference, and well calibrated (or modeled) standard star of the same spectral type as the observed standard. For that, we have used the reference spectral standards from the list of the Infrared Telecope Facility of Nasa[2].

4.3 H_2O bands and spectral-typing

One of defining features in the IR spectra for spectral types later than ∼M1, is that the atomic lines of H_2O molecules become stronger. Fig. 4.1 shows the broad and narrow band filters in SofI, and the atmospheric transmission (see caption for a detailed explanation). The temperature of a star is higher than the Earth's atmosphere which causes the absorption features to be broader, providing a good signal-to-noise of the H_2O in the wings of the H-band filter curve.

A distinct shape in the water vapour bands in the spectra of young stars, in comparison to field dwarfs, has been previously reported in the literature (Lucas et al. 2001; Kirkpatrick et al. 2006). In theses studies, a peaked, triangular continuum shape of the H-band has been seen in the spectra for brown-dwarfs, and used to claim low gravity,

[2] $http://irtfweb.ifa.hawaii.edu/IRrefdata/sp\_catalogs.html$

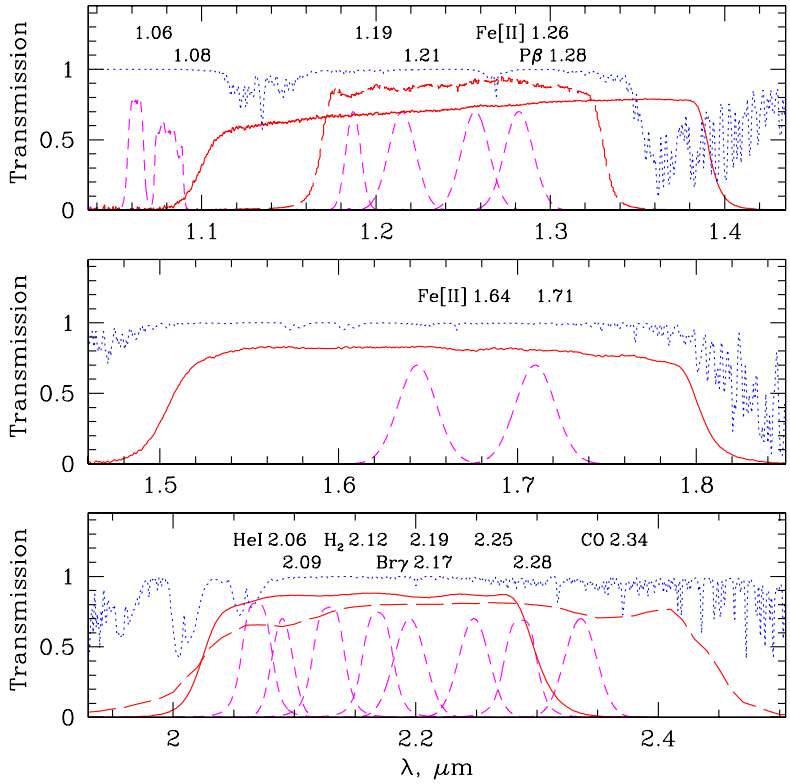

Figure 4.1: NTT's filter curves and atmospheric transmission model. The curves for the several broad-band JHKs filters and narrow-band filters at use in the NTT are plotted. The dotted line is the atmospheric transmission model for Mauna Kea, for airmass 1.0 and water vapour column of 1mm (Lord, S.D. 1992, NASA Technical Memor. 103957). Credits: ESO.

and hence youth and cluster membership, of the sources. However, while Lucas et al. (2001) did not attempt a physical explanation for this phenomenon, Kirkpatrick et al. (2006) has put forward an explanation that has been the subject of some discussion. Kirkpatrick et al. (2006) suggested that the 'triangular H-band shape' effect is due to H2 collisionally induced absorption. Molecular hydrogen exists in the low temperature atmospheres of stars/brown dwarfs, but this molecule does not have an electric dipole, required for a molecule to strongly absorb light. Welsh et al. (1949) discovered that collision-induced infrared absorption is observed for high enough gas densities in nonpolar gases, such as hydrogen. This process is termed collision induced absorption (CIA), where the collisions between molecules of high pressure gases produce temporary electric dipoles, responsible for absorption (see Frommhold 1993, and references therein). In astrophysics, this has been used to explain the atmospheric features of planets and cool stars (e.g. Borysow et al. 1997). But the hypotheses that CIA is the phenomenon responsible for the change in shape of H-band in the IR spectra of YSOs has been in-

vestigated and dismissed by Homeier (2008, private communication), who argues that this effect has been found not to be significant until much higher gravities and lower effective temperatures, and so unable to produced the observed spectral shapes of young BDs. The most likely cause of the distinct shape will probably be related to the difference in gravity between young and field dwarfs, but the exact cause is still unknown.

Given the low spectral resolution and modest signal-to-noise in the spectra taken, it is not possible to clearly distinguish atomic or molecular features, besides the broad water vapour absorption signatures. In order to estimate the spectral types, spectra with the same gravity as the observed target objects have been used. For this purpose, spectra of young low mass stars from Luhmann (2008, private communication) are used, which go from 0.8 to 2.5 μm with resolution $\sim$100 observed in the star-forming regions of Taurus and IC 348 (Luhman 2004). A key variable in fitting these reference spectra to the target spectra is the extinction, since this changes the overall shape of the continuum. A first estimate of the extinction for each target was made using the *H-K* colour or, when a *J* magnitude was available from 2MASS catalogues, *J-H* colour of the targets, and the wavelength dependence of extinction as defined by Rieke & Lebofsky (1985). This extinction was removed from the target spectra, and the target and reference spectra normalised to the same flux levels. During the fitting procedure, slight adjustments were made to the extinction value to improve the fit. However, in most cases, the extinction value derived using this photometric method gave an excellent fit and did not need to be modified. For each target spectrum, i was attempted to fit reference spectra from K5 to M9 and the best fit was used to determine the spectral type (Fig. 4.2). The results are listed in Table 4.3 along with the final extinction estimates for each source. Clear H_2O absorption was detected in 5 objects and reliable spectral type estimates were made for these. For most of the other targets, water vapour absorption was not detected, and only a limit to the spectral type can be set, i.e., they are generally earlier than M1. For two sources (AOCS-12 and AOCS-14) the spectra were too noisy to fit and these have been excluded from further discussion. Atmospheric absorption dominates all the spectra between $\sim$1.8 and 2.0 μm, causing the signal-to-noise ratio to be extremely poor, and these part of the spectra have, therefore, been removed.

4.4 Investigation of the youth of sources

The investigation of the youth for objects with a determined spectral type from the SofI observations, can disclose information about the membership of these stars in respect to the ρ Ophiuchi cluster. Photometric properties can provide signatures of youth at many wavelengths. In particular, I will look for the presence of thermal excesses, X-ray emission, and variability behaviours, characteristic of young stars to prove the youth of these stars.

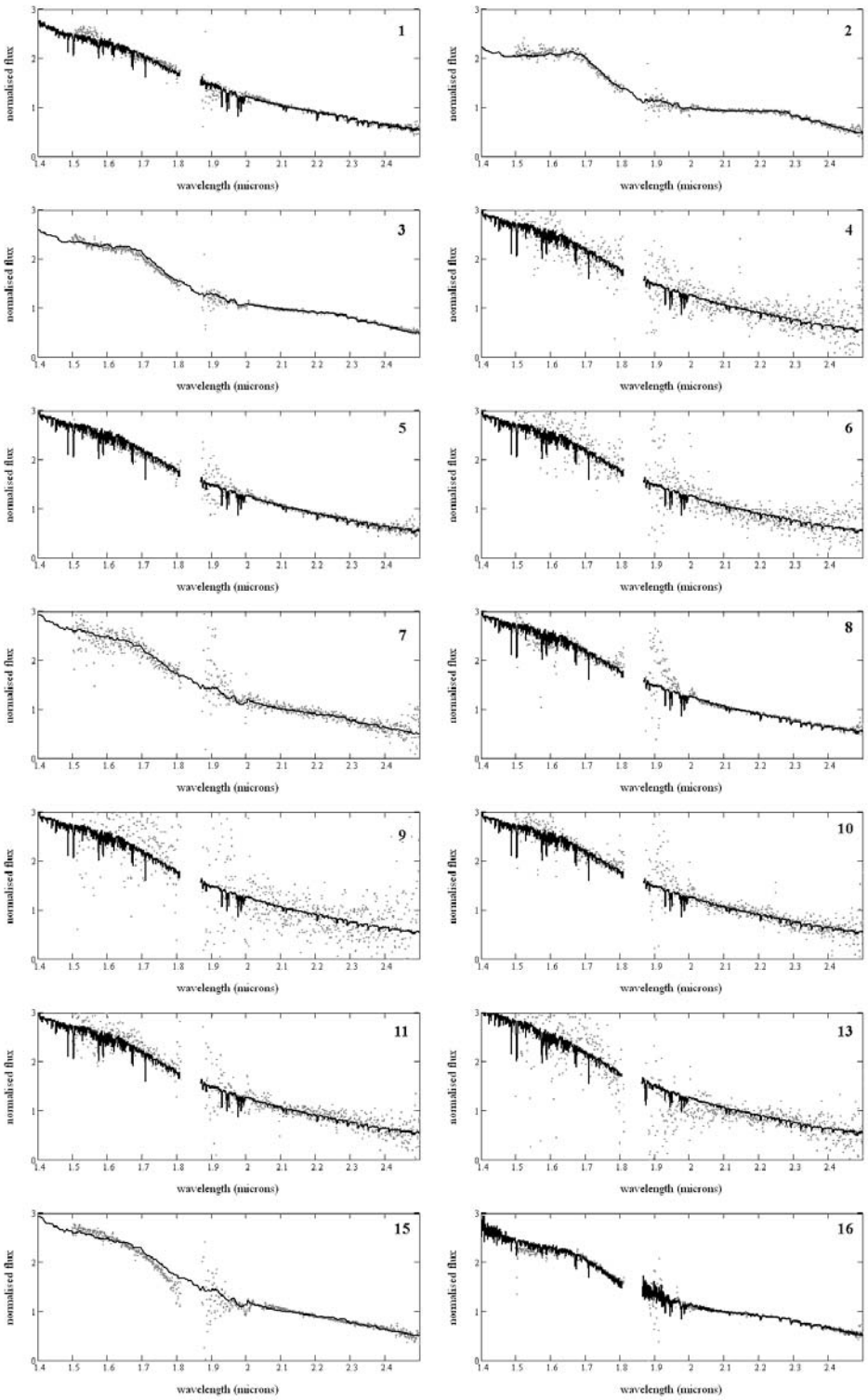

Figure 4.2: Low-resolution, near-IR spectra for the observed variable candidate members. The reference spectra are shown in solid line to which target spectra (grey dots) are fitted.

Table 4.3: Spectral-type and youth indicators.

ID	AOC Designation	A_V	SpT	Youth Indicator
1	J162816.41-240738.4	4.5	<M1	
2	J162736.14-240457.7	6.7	M5	Y (IR excess)
3	J162812.71-241135.7	9.1	M4	Y (IR excess, variability)
4	J162626.08-241106.3	6.3	<M1	
5	J162624.41-244345.5	5.2	<M1	Y (variability)
6	J162802.10-240844.9	6.7	<M1	
7	J162916.32-243844.0	6.3	M3	
8	J162718.36-242426.3	22.3	<M1	
9	J162845.88-240835.7	7.7	<M1	
10	J162824.38-242145.3	5.8	<M1	Y (IR excess)
11	J162656.27-241017.6	8.4	<M1	
13	J162714.34-243131.9	16.5	<M1	Y (IR excess)
15	J162814.76-242322.5	5.1	M3	
16	J162648.53-241227.5	12.4	M2	Y (X-ray emission)

4.4.1 Spitzer thermal excesses

The detection of IR excesses around classical T Tauri stars is one of the most direct evidence for the presence of discs around these stars. The accuracy in using the presence of IR excess as a single indicator for the existence of an accretion disc has been confirmed by the agreement that this indicator provides with other forms of detecting accretion in young stars, for example, through UV/optical excess emission (Kenyon & Hartmann 1995), spectroscopy or adaptive optics (Damjanov et al. 2007). Circumstellar discs are thought to dissipate withing ∼10 Myr after the formation of the parent star (Haisch et al. 2001; Cieza et al. 2007; Carpenter et al. 2005), thus their detection can be used as a youth indicator.

Mid-IR observations are more sensitive to detect excess emission from discs around young stars, since the emission from the stellar photosphere at these wavelengths has already decreased substantially from the blackbody peak, while the disc emission increases at longer wavelengths. The two imaging cameras IRAC and MIPS (Spitzer) covering the mid-IR part of the spectrum, are therefore the best current instruments to identify discs around young stars (see Sect. 2.2 and Sect. 3.5). All the 14 sources with spectroscopy are present in the Spizter catalogues, although not all of them are detected in all bands. It should also be noted that all the objects are classified in the Spitzer catalogues as point-like sources, i.e., the source is well fitted by a point source profile. Faint extended sources are likely to be extragalactic objects (although could also be YSOs), so it is reassuring that they do not exist in the spectroscopic sample.

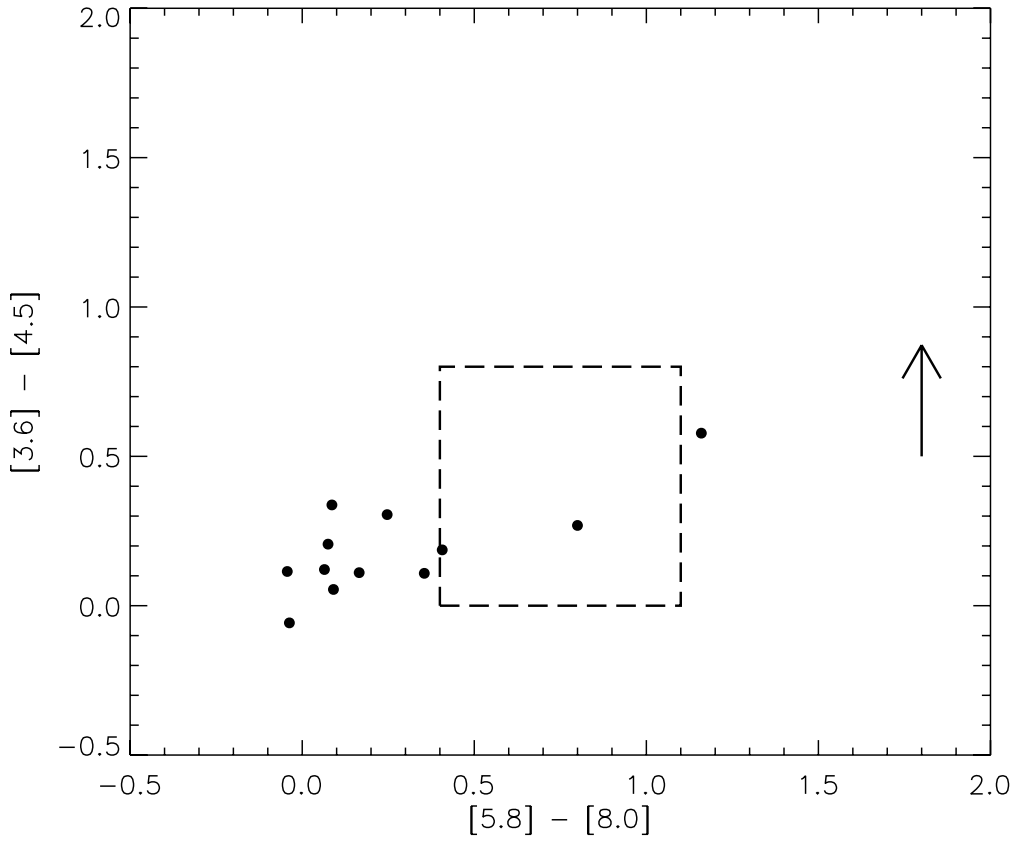

Figure 4.3: IRAC colour-colour diagram for candidate members with spectroscopy. Arrow represents the A_K=4 extinction vector for ρ Ophiuchi (Flaherty et al. 2007).

In order to look for IR excesses, the sources have been plotted in the colour-colour IRAC/Spitzer diagram, [3.6]−[4.5] vs. [5.8]−[8.0] (Fig. 4.3). There are 4 objects (AOCS-2, AOCS-3, AOCS-10, AOCS-13) located inside the box defined by Allen et al. (2004), which represents the colours expected from models of discs around young, low-mass stars. These objects show a flux excess at longer wavelengths that is evidence for the existence of a surrounding disc, consistent with the hypothesis that they are young pre-main-sequence stars. The other objects tend to cluster around the origin, [3.6]−[4.5],[5.8]−[8.0]=(0,0), where sources which have colours consistent with stellar photospheres and have no intrinsic IR-excess are expected. These can be foreground and background stars, but also Class III young stars which do not have significant circumstellar dust. In this region of the colour-colour plane, it is not possible to use this technique to differentiate between young stars and field contaminants.

Another useful tool to look for IR excess, is to combine near-IR data from WF-CAM with the MIPS/Spitzer 24 μm-band and study the magnitude-colour diagram K_s vs. K_s-[24] (Fig. 4.4). Unfortunately, the sensitivity of the [24] μm band is quite

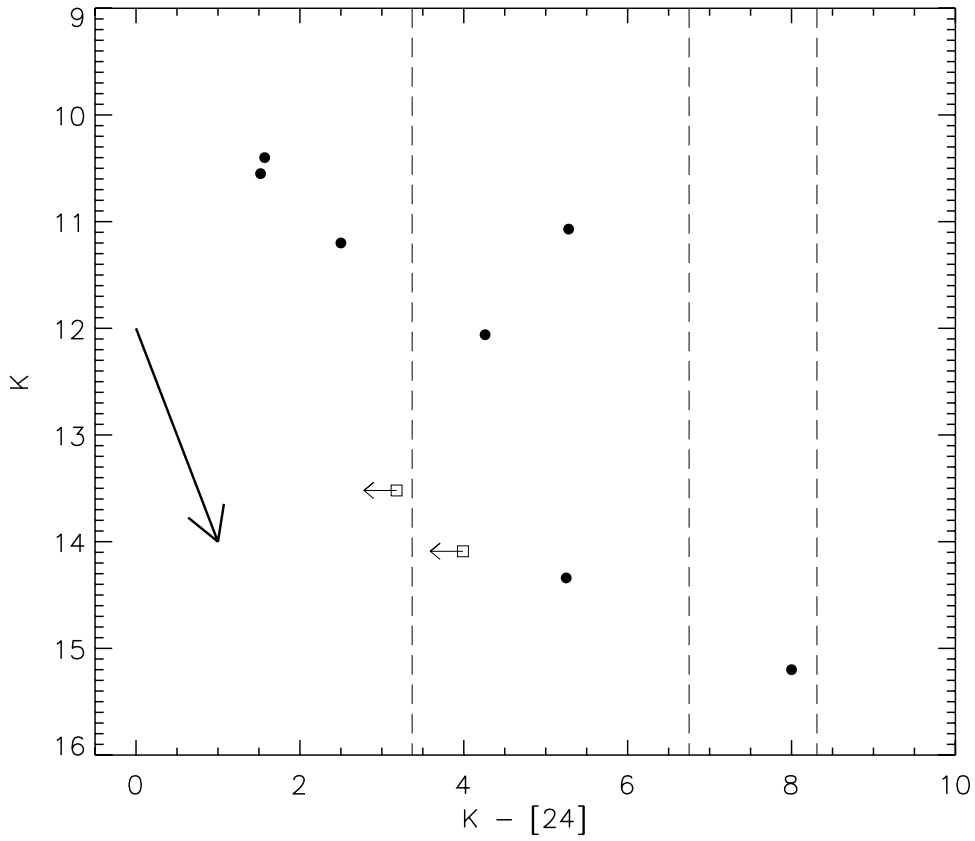

Figure 4.4: WFCAM/UKIRT and MIPS/Spitzer colour-magnitude diagram for candidate members with spectroscopy. The reddening vector is from Flaherty et al. (2007) and represents an A_K of 5 magnitudes. Two stars represented with arrows are only upper-limits. Objects with K_s-[24] > 8.31 are Class I objects, 6.75 < K_s-[24] < 8.31 are flat-spectrum objects, 3.37 < K_s-[24] < 6.75 are Class II objects, and K_s-[24] < 3.37 are Class III (Greene et al. 1994).

limited, and only 7 from our sources with spectroscopy have reliable photometry. Another 2 sources (AOCS-1 and AOCS-11) only have an upper limit determined in the Spitzer reductions and although the errors are significantly larger, they are also plotted in the diagram as upper limits. In this diagram, stellar photospheres are clustered around K_s−[24] μm∼0, and sources with K_s−[24] μm∼2 show a strong IR excess. The reddening vector is from Flaherty et al. (2007) and represents an A_K of 5 magnitudes. The four sources which had already shown an IR excess in the [3.6]−[4.5] vs. [5.8]−[8.0] diagram also show a significant excess at 24 μm, providing further evidence of the existence of a circumstellar disc (following the Greene et al. (1994) mid-IR classification scheme which was presented in Sect. 3.5). Additionally, 3 objects (AOCS-8, AOCS-15, AOCS-16) show a moderate excess, but they fall in the region designated for WTTSs (and also stellar photospheres), so nothing more can be concluded.

4.4.2 X-rays

A described previously in Sect. 3.6, ρ Ophiuchi has been the target of several X-ray surveys, first with *Einstein*, ROSAT and ASCA (Montmerle et al. 1983; Casanova et al. 1995; Martin et al. 1998; Grosso et al. 2000; Kamata et al. 1997), and more recently using new instruments which are more sensitive and have higher spatial resolution, such as Chandra and XMM-Newton (Imanishi et al. 2001; Gagné et al. 2004; Ozawa et al. 2005). Furthermore, in the compilation of known members of the Ophiuchus cluster done by Wilking et al. (2008), the authors use the results of two unpublished X-ray studies, one led by N. Grosso using Chandra surveying the outer regions of the cluster, and the other being the XMM DROXO survey by Sciortino et al. (2006). These compilation of X-ray catalogues from Wilking et al. (2008) was searched for X-ray counterparts for the targets with spectroscopy. AOCS-16 has an X-ray detection from the unpublished deep survey of N. Grosso in the outer parts of Ophiuchus, and has been classified solely on this X-ray detection as a young object. Therefore, this argument is used as evidence of youth. The rest of the objects, are not detected in X-rays. However, this could have several explanations and does not exclude in any way the possibility that they are young.

Recent and more sensitive studies carried out with XMM-Newton and Chandra (Imanishi et al. 2001; Gagné et al. 2004; Ozawa et al. 2005) were analysed and it was found that none of the spectroscopy targets falls in the field-of-view of the Chandra survey done by Gagné et al. (2004). Three of the targets fall in the fields-of-view of the Chandra study by Imanishi et al. (2001) and XMM-Newton by Ozawa et al. (2005). One of these objects, AOCS-3, has had its youth confirmed by previous studies in the literature (Bontemps et al. 2001; Natta et al. 2002), but it had missed the cross-match criterion to the WFCAM data. The reason was that its coordinates from ISOCAM (Bontemps et al. 2001) had a 7" offset and at the time of the observations this object had not been associated with source AOCS-3. The other two objects are AOCS-5 (K=15.71, A_V=5.2) and AOCS-8 (K=11.20, A_V=22.3), where the combination of their faint magnitudes with high visual extinctions could explain why they have not been detected in X-rays. Three other objects (AOCS-4, AOCS-11, and AOCS-16) are included in the field-of-view of a ROSAT survey by Grosso et al. (2000), however given their faint magnitude is it unlikely that they could have been detected. The remaining eight of our objects, are placed in the north-east side of the centre of the cluster, and are not included within the fields-of-view of these recent X-ray surveys (see Fig. 4.5). In fact, in this region there are only 11 objects classified as members of Ophiuchus with X-rays by three studies, one with XMM-Newton (7 sources with $K < 10.9$ mag, N. Grosso, unpublished) and the other ones made with *Einstein* (3 sources with $K < 9.0$ magnitudes Montmerle et al. 1983) and Rosat (1 source with K=6.85 Martin et al. 1998). Regarding the survey of N. Grosso, there is not any published information, such as the area surveyed or the exposure time of the observations, and it cannot be discussed if the spectroscopy sample could have been detected in X-rays or not. The

two other surveys, should not be sensitive enough to detect the X-ray emission from our faint sources, except if a large energetic event occurred at the time of their observations. Therefore, it is not known if these sources have or not X-ray emission, and no further statements can be made regarding their youth using X-rays.

4.4.3 IR variability

The variability characteristics of the sources can also be important in confirming their youth. In Chapter 3 it was shown that the amplitude magnitude and colour of the IR photometric variations can be associated with physical processes which are know to occur in young stars and brown dwarfs. Previous classification of possible causes of the variability, can be used as evidence that the targets of the spectroscopic survey show variability consistent with them being young, and unlikely to be present in field stars.

Objects AOCS-3 and AOCS-5 have variability characteristics which can be explained by changes in accretion disc structure (see Sect. 3.8 for an explanation). In particular, they show a negative slope (-45 and -36, respectively) in the colour-magnitude diagram K vs. $H-K$, which is in agreement with the disc models that have been addressed previously in Sect. 3.8. Also, AOCS-13 shows variability consistent with changes in the circumstellar extinction, having a positive slope of +57. The remaining sources, are consistent with the existence of cool or hot spots, but their amplitude magnitude and colour variations are also consistent with those of field M-dwarfs (see Sect. 3.1), so their nature remains unclear.

4.5 Membership and masses

A total of 6 objects show evidence of youth. In order to have an estimate of their masses, the derredened magnitudes (adjusted according to their A_K values found during the spectral analysis) are plotted in the K vs. $H-K$ colour-magnitude diagram (filled circles, see Fig. 4.6). The stars for which a signature of youth was not found with the available criteria (i.e., IR-excess, X-ray emission, or variability not consistent with M dwarfs) are also shown (open diamonds). The curves in the diagram show the model evolutionary tracks of the Lyon group (Baraffe et al. 1998; Chabrier et al. 2000; Baraffe et al. 2003) for a cluster at a distance of ∼119 pc (Lombardi et al. 2008). The curves in black are the theoretical 1 Myr isochrones, for low mass stars ranging from 0.4 $M_\odot$ down to 0.012 $M_\odot$ ($\sim 12 M_{Jup}$, approximately the deuterium burning limit). The isochrones are a combination of the NextGen and the DUSTY isochrones (Baraffe et al. 1998; Chabrier et al. 2000), and NextGen and Cond (Baraffe et al. 1998, 2003) (see Sect. 3.3 for an explanation), though at this temperature range there are no significant changes between the different evolutionary models. The filled black ar-

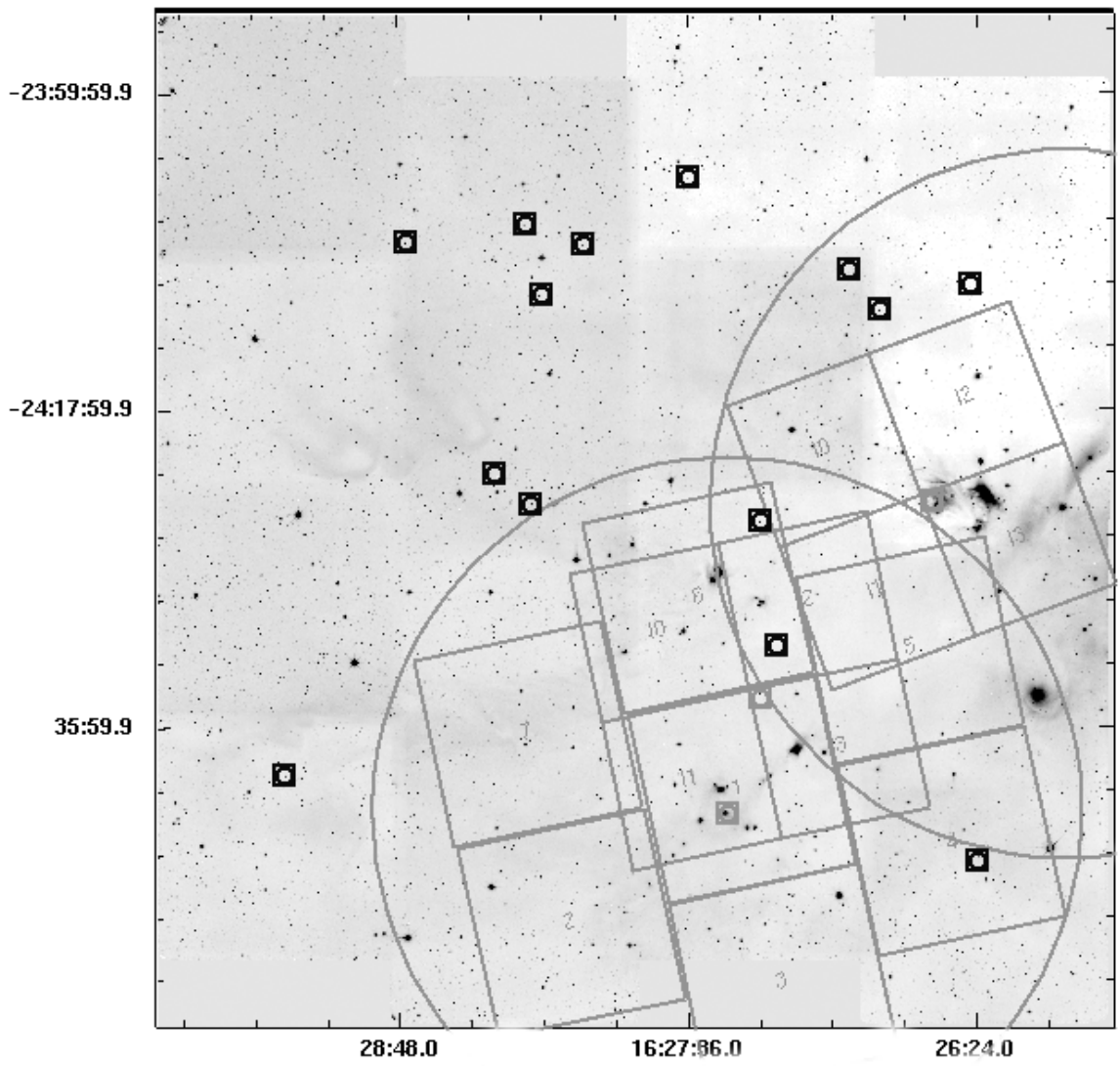

Figure 4.5: Variable candidates with spectroscopic follow-up. Overplotted are the fields-of-view of Chandra (Imanishi et al. 2001; Gagné et al. 2004), XMM-Newton (Ozawa et al. 2005), and ROSAT (Grosso et al. 2000)

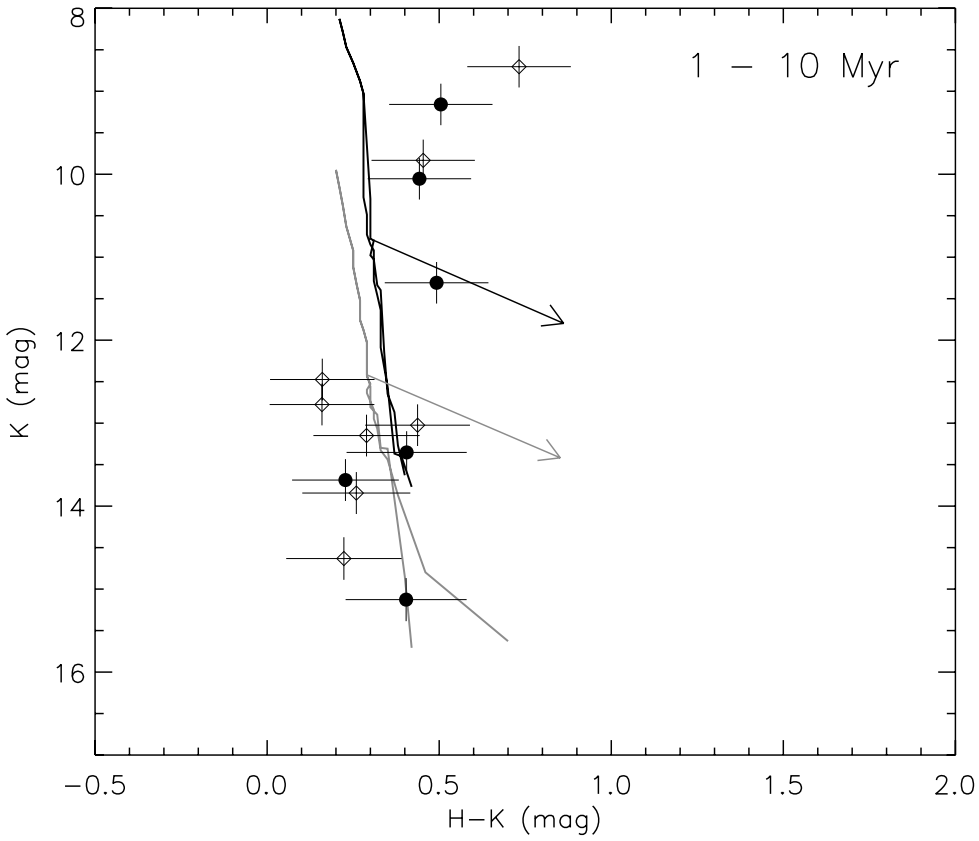

Figure 4.6: Colour-magnitude diagram of the derredened sources consistent with youth (filled circles) and also the ones for each there is no confirmation of youth (open diamonds). Black lines represent the 1 Myr isochrones (at 119 pc) of the Lyon group (see text for detailed explanation), while the gray lines are the 10 Myr isochrones.

row is the reddening vector for A_K=1 magnitudes, following the reddening law from Rieke & Lebofsky (1985), and denotes the hydrogen burning limit, i.e. $\sim$75 M_{Jup}. The curves in grey, show the same models but for an age of 10 Myr. The error bars shown include the photometric errors of the magnitudes and the error on the determination of the A_K extinction, done by spectral fitting, which is estimated to be $\pm$0.25 magnitudes.

At a first glance, the results do not seem consistent with a single age. In the colour-magnitude diagram (Fig. 4.6), seven stars lie to the right of the 1 Myr isochrone, where one expects to see stars with approximately this age, or younger. Within the errors, two of these objects (AOCS-11496, -933) are consistent with having masses below the hydrogen burning limit, and ages between 1 and 10 Myr. Furthermore, AOCS-933 shows mid-IR excess, which could indicate the existence of a circumstellar disc. However, water absorption features have not been seen in the spectra of these two objects, which would be expected for stars with such young ages, and low masses. For AOCS-993, one possibility which cannot be excluded is that this object could be

an extragalactic source, since its faint magnitudes and very red mid-IR colours are also consistent with those of AGN. Therefore, the nature of these objects remains uncertain.

Four other stars located to the right of the isochrones, (AOCS-2, -3, -15, and -16), seem to be consistent with having a single age, since their positions in the colour magnitude diagram seem to delineate an isochrone at an age <1 Myr. One of these sources, AOCS-3, is the target that had been previously observed by Natta et al. (2002), where the authors classify it as a brown dwarf with an age below <1 Myr and mass in the range from ∼40 to 80M_{Jup}, though they alert for the large uncertainties of evolutionary models at such young ages. However, it provides a good check that this object is young. Also, AOCS-3 and -16 have shown signatures of youth, according to the criteria presented in the previous section. It is, however, difficult to provide an accurate mass estimate for these objects, but from their position in the colour-magnitude diagram, they could have masses between those of more massive brown dwarfs and very low mass stars. Furthermore, water absorption features were clearly present in the spectra of these objects with spectral types M5, M4, M3, and M2 for AOCS-2, -3, -15, and -16, respectively. Based on the fact that they have a spectral type later than M1, that all (except one) showed clear signs of youth, and that their position in the colour-magnitude diagram is consistent with a single age, these sources are classified as *bona fide* members of the ρ Ophiuchi cluster.

Only one object is left to discuss at the right of the isochrones, AOCS-923. The position of this object seems odd in this diagram, since it would imply an extremely young age. The most likely explanation is that the extinction value calculated from the spectral fitting is not correct. This could be due to the position of this star on the sky, a region of high extinction (the value derived from spectral fitting is A_V=22, the largest of the whole spectroscopic sample) and nebulosity. Though this object seems consistent with being a young star, member of Ophiuchus, there is not enough evidence to confidently classify it as such.

Finally, 7 sources (AOCS-4, -5, -6, -7, -9, and -11) are located to the left of the isochrones, where objects older than 10 Myrs are expected. All sources are, within the limiting magnitude errors, consistent with an age of 10 Myr. However, the lack of a determined spectral type (only AOCS-7 has an assigned spectral type of M3) or indication of youth (only AOCS-10 showed IR-excess, and AOCS-5 showed variability inconsistent with that expected from a M dwarf), make difficult any sound classification of these stars.

4.6 Chapter conclusions

The results of a spectroscopy follow-up for a sample of variability selected candidate members of the ρ Ophiuchi cluster have been presented. The observations were done in visitor mode, resulting from a successful proposal to use ESO telescopes, using SofI at the NTT. Low-resolution near-IR spectra were taken for 16 targets. Following the first step of data-reduction, the spectra were derredened, compared with reference spectra of young low mass stars from another star forming region, and classified using primarily water vapour absorption features. Reliable spectral type estimates were made for 5 objects, ranging from spectral types M2 to M6. The presence of IR-excess, X-ray emission or variability behaviour inconsistent with that of M dwarfs, were used as criteria to identify signatures of youth. The membership of the sources was assessed by plotting them in a colour-magnitude diagram and making a comparison to evolutionary models of young low mass stars and brown dwarfs. According to evolutionary models, four sources with spectral types from M2 to M5 and showing signatures of youth, should be younger than 1 Myr and have masses between those of massive brown dwarfs and very low-mass stars. One of these sources has had its membership confirmed by another independent study, which reassures the success of the analysis methods employed in this chapter. The remaining three young stellar objects are classified as *bona fide* members of the ρ Ophiuchi cluster, found through variability.

Table 4.4: WFCAM and Spizter magnitudes.

AOC Designation	H	K	[3.6]	$Q_{3.6}$	[4.5]	$Q_{4.5}$	[5.8]	$Q_{5.8}$	[8.0]	$Q_{8.0}$	[24]	Q_{24}
J162816.41-240738.4	14.24	13.52	± 0.79	A	12.95 ± 0.75	A	12.90 ± 1.24	A	12.73 ± 1.56	A	...	...
J162736.14-240457.7	12.97	12.06	± 0.62	A	11.03 ± 0.71	A	10.41 ± 0.54	A	10.00 ± 0.55	A	7.80 ± 0.85	A
J162812.71-241135.7	12.09	11.07	± 0.51	A	9.91 ± 0.53	A	9.43 ± 0.46	A	8.63 ± 0.42	A	5.79 ± 0.54	A
J162626.08-241106.3	15.20	14.54	± 0.73	A	13.91 ± 0.79	A	13.97 ± 2.12	B	...	...	...	...
J162624.41-244345.5	16.44	15.71	± 0.97	A	15.05 ± 1.01	A	...	...	...	...	...	...
J162802.10-240844.9	16.03	15.38	± 0.94	A	14.86 ± 1.17	A	15.01 ± 3.82	C	...	...	...	...
J162916.32-243844.0	14.04	13.49	± 0.67	A	13.00 ± 0.66	A	12.89 ± 0.94	A	12.82 ± 1.31	A	...	...
J162718.36-242426.3	13.34	11.20	± 0.49	A	9.65 ± 0.47	A	9.34 ± 0.44	A	9.25 ± 0.45	A	8.70 ± 1.68	B
J162845.88-240835.7	13.98	13.33	± 0.63	A	12.70 ± 0.62	A	12.56 ± 0.79	A	12.60 ± 1.22	A	...	...
J162824.38-242145.3	14.93	14.34	± 0.69	A	13.77 ± 0.73	A	13.62 ± 1.28	A	13.27 ± 2.40	B	9.09 ± 1.81	B
J162656.27-241017.6	14.91	14.09	± 0.87	A	13.43 ± 0.83	A	13.39 ± 1.90	A	13.30 ± 3.21	C	10.10 ± 5.92	...
J162920.92-241936.8	16.36	15.90	± 1.00	A	15.37 ± 1.16	A	...	...	...	...	...	...
J162714.34-243131.9	16.65	15.20	± 0.72	A	13.49 ± 0.67	A	13.06 ± 1.16	A	11.90 ± 0.94	A	7.20 ± 0.72	A
J162911.85-243955.9	16.38	15.32	± 0.82	A	14.39 ± 0.79	A	14.17 ± 2.15	B	14.10 ± 4.65	C	...	...
J162814.76-242322.5	11.18	10.40	± 0.47	A	9.35 ± 0.46	A	9.07 ± 0.43	A	8.83 ± 0.42	A	8.83 ± 1.53	B
J162648.53-241227.5	11.84	10.55	± 0.49	A	9.89 ± 0.60	A	9.44 ± 0.46	A	9.48 ± 0.50	A	9.03 ± 2.66	C

Chapter 5

Near-IR instrumentation: HAWK-I

HAWK-I (High-Acuity Wide-field K-band Imager) is the new wide-field IR camera installed at the ESO Very Large Telescope (VLT), operating from 0.9 to 2.4 μm (Kissler-Patig et al. 2008b). In this chapter, I will present the instrument, which was constructed and commissioned by the HAWK-I team at ESO. The first section is included for completeness, and presents a summary of the instrument and its science case for the star formation research field. The other sections describe work performed by me, first at the ESO laboratories where the testing and characterisation of the filter system was done (Sect. 5.2), and secondly the tasks with which I was directly involved during the commissioning of the instrument in Paranal (Sect. 5.3).

5.1 Introducing HAWK-I

There were several drivers for the construction of a new IR camera on the VLT. Firstly, the technological advance in IR detectors has made possible the exploration of the IR wavelength regime, where emission from the colder Universe, signatures from extremely obscured objects, or emission from highly redshifted galaxies is detected. This has caused an increase in the demand from the scientific community for the IR imaging facilities at ESO telescopes, which have been provided by SofI (NTT) and ISAAC (VLT) (also NACO but with a smaller field-of-view and fed by AO, used for somewhat different applications). However, both SofI and ISAAC are still using the first generation 1k x 1k array detectors and cannot support an upgrade for the new 2k x 2k arrays (since the field is limited by the instrumental design) which are currently being used in several instruments around the world, primarily for surveys (e.g., WFCAM at the UKIRT, or WIRCAM at CFHT). Secondly, in the future, when VISTA (IR camera with sixteen 2k x 2k detectors and 0.34" pixel scale) and KMOS (IR multi-object integral field spectrometer) start to operate, the deep imaging and high spatial resolution images of HAWK-I would be a fundamental complementary capability (Casali et al. 2005, 2006). HAWK-I is the first IR camera of its kind on an 8 meter telescope (Fig. 5.1), being capable of delivering well sampled images down to the best seeing limit on Paranal.

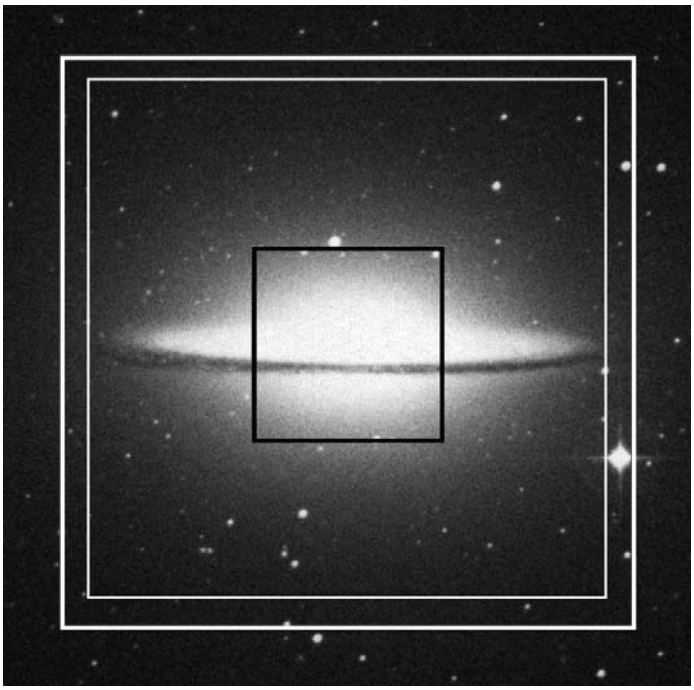

Figure 5.1: Comparing HAWK-I and ISAAC fields-of-view (Casali et al. 2005). An image of the Sombrero galaxy is shown with the fields-of-view of ISAAC-VLT (central black line), FORS2-VLT (inner white line), and HAWK-I (outer white line) overlaid.

5.1.1 The star formation science case

There are several science cases for HAWK-I, from high redshift galaxies to nearby star-forming regions (Moorwood et al. 2003). The star formation science case is here briefly presented, since it is relevant for the context of this thesis. The main science goals for star formation are the following:

- *Massive stars:* The formation of massive stars is still widely debated with two competing paradigms being studied at the moment (e.g. Beuther et al. 2007, and references therein). The basis of the problem is that massive star formation causes radiation pressure on the disc and gas around it, which can be strong enough to halt the accretion process. When this happens, the paradigm of formation of low-mass stars no longer applies to these massive objects. One of the theories to form massive stars proposes that the accretion scenario still holds if changes are applied to several parameters (e.g., dust properties, accretion rates, existence of cavities, instabilities, etc.). Opposing this idea, is the coalescence scenario which defends that in high density clusters, protostars undergo collision and merge, suppressing the effects of radiation pressure. Coupled with this, are the environmental effects, still largely unknown both for the impact they may have in the IMF of massive star formation, or for the impact massive star formation has for adjacent low-mass stars. HAWK-I can provide the high sensitivity and

spatial resolution necessary for the study of these regions (located further away than low-mass star-forming regions) but also of the photometric and astrometric inhomogeneity over a large field, more suitable to study this extended regions.

- *Dynamical studies of young, protostellar jets:* The production of jets and collimated outflows is a fundamental aspect for the study of accretion, rotation and magnetic field scenarios in young stars (e.g. Bally et al. 2007; Ray et al. 2007, and references therein). Proper-motion studies can measure the velocities involved at various stages of the outflows, such as the accretion rate timescale or the interaction of the jet with the surrounding medium. However, these jets can extend for several arcminutes on the sky, and mosaicing is often required which limits the accuracy of the astrometric measurements and also costs greater amounts of time. HAWK-I's large field-of-view allows to cover large regions of a jet in a single-pointing which combined with the high spatial resolution of the camera allows a more accurate measurement of lower velocities.

- *Measuring the initial mass function (IMF):* Measuring the IMF as a function of environment (metallicity, cluster density, etc) is an important and much attempted goal of star formation (e.g. Bonnell et al. 2007, and references therein). The comparison of the IMF from different star forming regions would help answering some of the key questions such as the timescale for star formation within a molecular cloud, the role of the environment in the stellar masses, etc. Also the extension of the IMF to the brown dwarf and planetary regime and the search for the end of the mass function would provide a large observational contribution to the development in the theory of star formation. HAWK-I can provide deep near-IR photometry over large scales of nearby star-forming regions together with accurate proper-motion measurements, which will enable to find a full census of the low-mass members of these clusters.

5.1.2 Instrument description

HAWK-I is a cryogenic instrument equipped with four 2k x 2k Rockwell HgCdTe MBE HAWAII 2 RG detectors and has a field of view of 7.5' x 7.5' with a 0.106" pixelscale (Kissler-Patig et al. 2008b). The four detectors are separated by a small gap of ∼15" (see Fig. 5.2). The catadioptric design with its all reflective configuration (excluding the entrance window) provides a high throughput which gives HAWK-I a signal-to-noise improvement of 10-20% over, for example, ISAAC (Casali et al. 2006). Figure 5.3 shows the optical layout of the instrument. The entrance window is used to form a pupil image on the M3 mirror, which is the system cold stop and defines the field of view. M1 is a large flat mirror used for beam accommodation. M2 is a tilted spherical mirror, while M3 and M4 are aspherical mirrors, and are configured to achieve the required F/4.36. The two filter wheels are located in front of the detector mosaic. All the optics and the focal plane are mounted inside a spherical aluminium

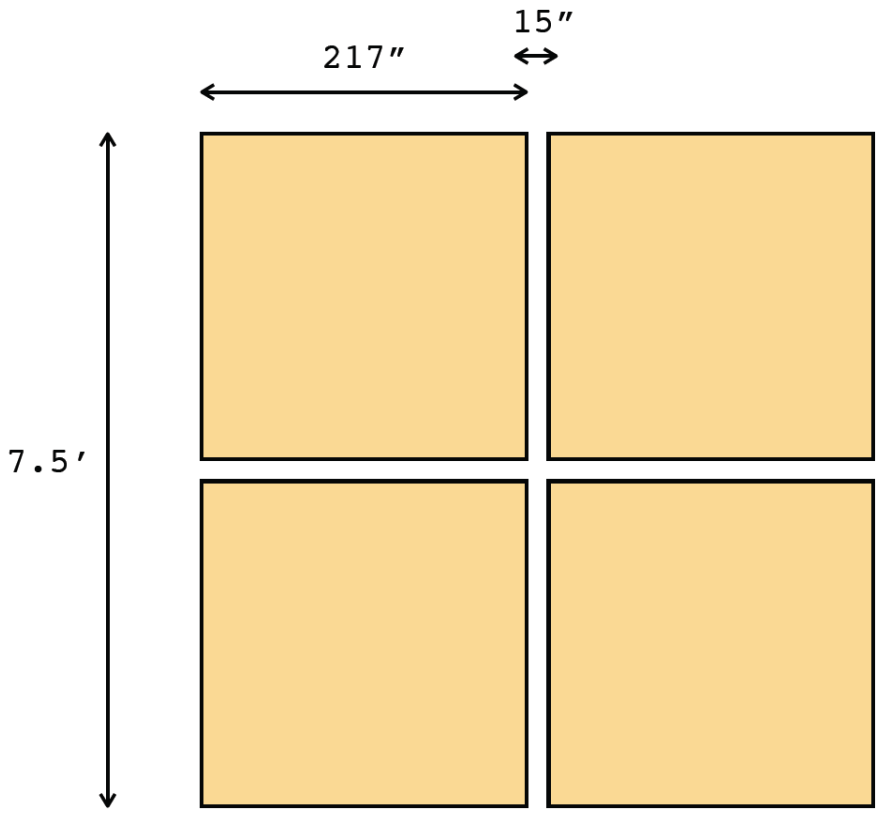

Figure 5.2: HAWK-I field of view covered by the mosaic of the four detectors on the sky.

cold structure, which is cooled to cryogenic temperatures using a liquid pre-cooling circuit and two closed cycle coolers. An overview of the HAWK-I characteristics has been presented by Kissler-Patig et al. (2008b) and shown in Table 5.1.2 for completeness.

HAWK-I started regular operations on April 2008, after being commissioned on the ESO VLT between August 2007 and February 2008. Fig. 5.4 shows the instrument mounted on the telescope, attached to the Nasmyth focus of the Unit Telescope 4 of the ESO VLT.

5.2 Evaluation of broad band filters for HAWK-I

HAWK-I has two filter wheels cooled at cryogenic temperature with six positions each. The two wheels together host 4 broad band filters, 6 narrow band filters, and an open position (each). The broad-band filters are *YJHK* and follow the Mauna Kea Observatory specifications (see Tokunaga & Vacca 2005, and references therein). This convention allows an easy cross-calibration and comparison between HAWK-I

Table 5.1: HAWK-I properties.

Parameter	Value
Scale	106 mas/pixel
Field of View	7.50' x 7.50'
Image quality	<0.2"
Distortion	<0.3% across the field
Optics throughput	>70% (without detector)
Filters	4 Broad Band, 6 Narrow Band
Detectors	four 2k x 2k Hawaii 2RG arrays
Detector Q.E.	> 80%
Detector Temperature	75 K ± 1 mK
Read noise	$\sim 5e^-$ for DIT>15s
Instrument background	$\sim 0.10-0.15$ e^-/s
Instrument Temperature	<140 K

and the UKIDSS survey (Hewett et al. 2006) as well as the VISTA infrared camera (Dalton et al. 2006). The narrow band filters include three cosmological filters (for Lyα at z$\sim$7.7 (at 1.06 μm) and z$\sim$8.7 (at 1.19 μm), and Hα at z$\sim$2.2 (at 2.09 μm) as well as three *galactic* filters (CH4, H_2, Brγ). The broad band filters have been produced and delivered by the company Research Electro-Optics Inc., while Barr Associates Inc. provided the wide and narrow band filters. In this section, I will present the results of the evaluation of the broad-band filters for the HAWK-I instrument which I have conducted at the IR-laboratory at ESO.

5.2.1 Environmental and Spectral Requirements

ESO provided the companies producing the filters with technical specifications, which involved the filters design, and the environmental and spectral requirements. The aim of the tests was to check the compliance of the delivered filters with these requirements.

The filter environmental requirements provide the temperature, humidity and pressure range, both for storage and operating conditions, for the filters as follows:

- Storage conditions:
  - temperature between -33 °C and +85 °C
  - humidity between 0 and 95%
- Operating conditions:
  - Temperature: 90+/-5 K
  - Pressure: $< 10^{-6}$ Torr

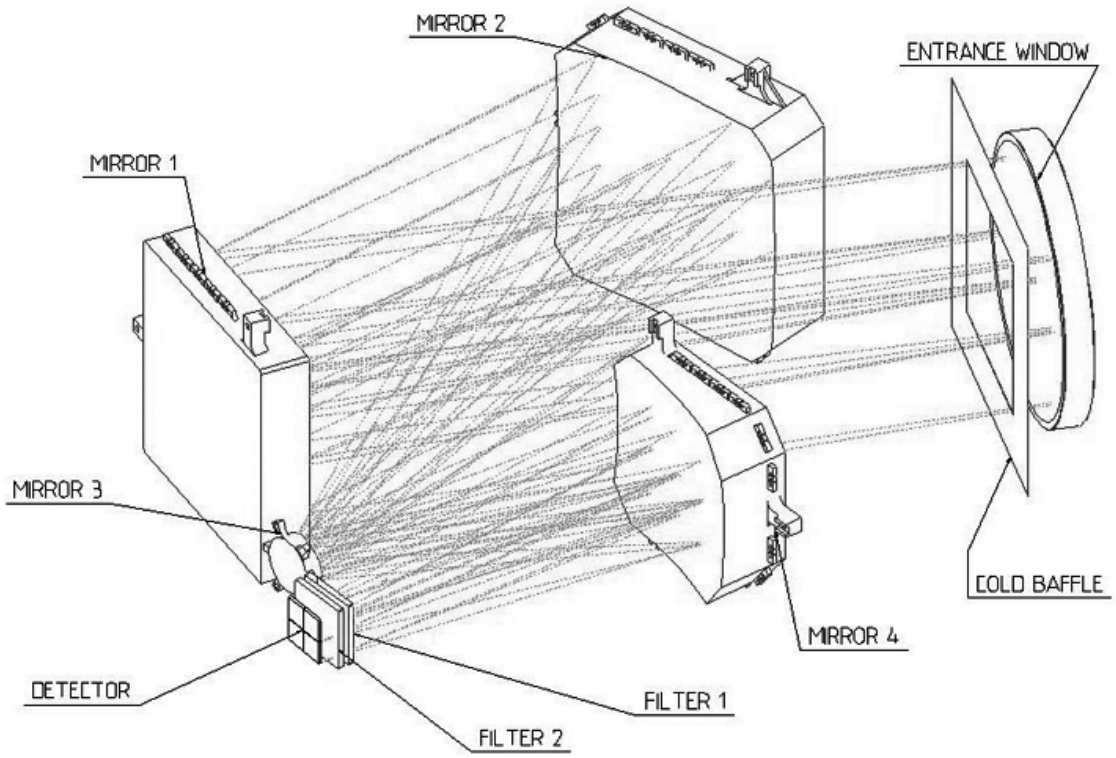

Figure 5.3: HAWK-I optical layout (Kissler-Patig et al. 2008b).

Besides complying to these requirements, the filters should also be tested to evaluate the effects from pressure or temperature transition during the change from atmospheric pressure to vacuum, and/or from room to cryogenic temperature, and vice versa.

The spectral requirements for the broad band filters have been specified at operating conditions (cryogenic temperatures, beam aperture F/4 and under vacuum), and set the desired values for several parameters which defined the spectral shape, such as the central wavelength, the bandwidth 50% cut-on and 50% cut-off half power points, the absolute transmission and the out of band transmission. These are summarised in Table 5.2.1.

5.2.2 Laboratory tests

The aim of the laboratory tests was to study the transmission spectrum of each filter, which shows which portion of the energy is reflected by the filter (out-of-band), and what is the efficiency of the remaining light that travels through the filter, which should be high within the filter band (<80%), and low (>0.01%) in the out-of-band regions.

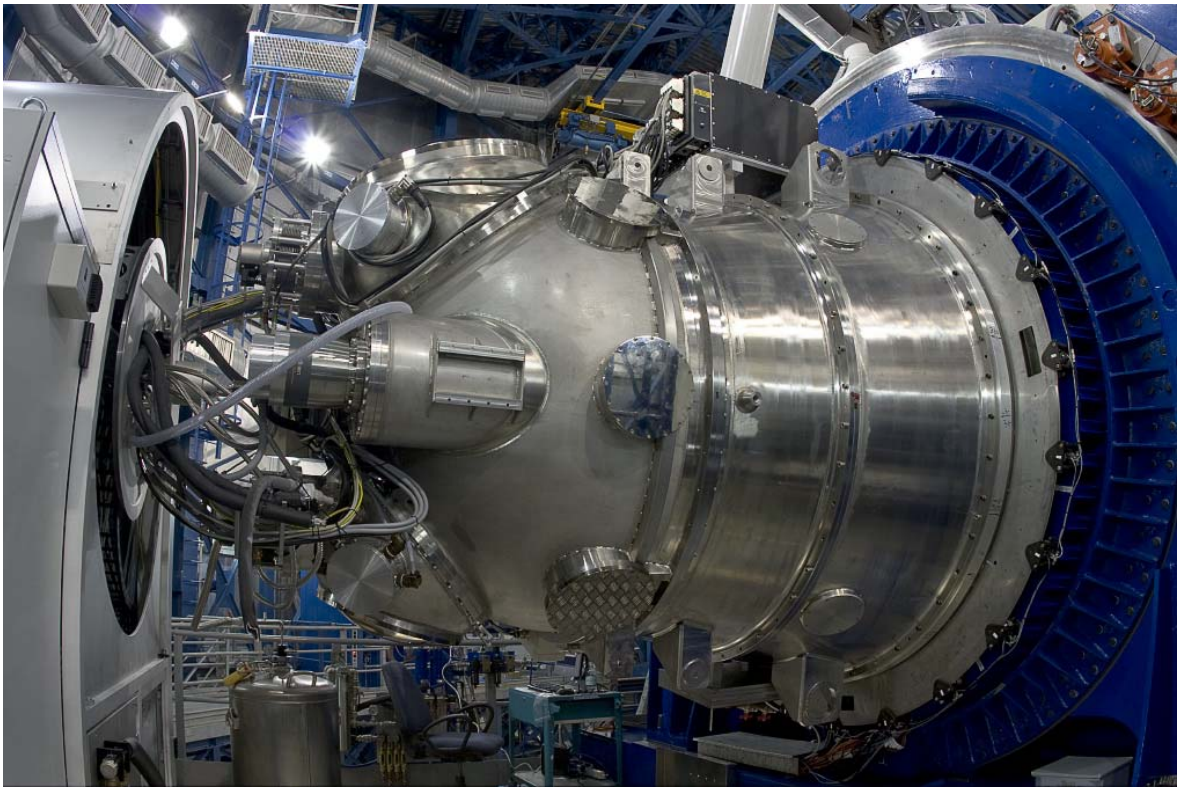

Figure 5.4: HAWK-I on the Nasmyth focus of the UT4/VLT. On the right in blue is the adapter/rotator of the telescope. On the left in light grey is the cable co-rotator fixed on the Nasmyth platform. Credits: ESO.

ESO received 3 examples for each broad band filter, so besides verifying the filters' compliance, it was also the goal of these tests to identify the best filter (closer to the specifications) which would be used at the telescope.

Performance at cryogenic temperatures

The first set of tests consisted of measuring the transmission spectra of small samples from the real filters (usually called *witness*) in vacuum conditions both at room and cryogenic temperatures, in order to investigate the possible occurrence of a shift in wavelength when cooling down the filter. These tests were performed using the Fourier Transform Infrared Spectrometer (NICOLET 5700). Witnesses were used since the real filters were too big (105 x 105 mm) to fit in the equipment used. The experiment was done in three stages. First, a witness was placed inside a variable temperature cell, a device used to study the transmission of samples at cryogenic temperatures. This device consists of a vacuum outerlayer containing a refrigerant dewar and a heating block which contains the sample. The temperature of the dewar is measured externally. The whole system is operated in vacuum conditions (achieved by using an external pump,

Table 5.2: Spectral requirements for HAWK-I broad-band filters.

Filter name	Half Power point cut-on, -off (μm)	Central Wavelength (μm)	Average Efficiency
Y	0.97 , 1.07 ±0.5%	1.02 ±0.5%	>80%
J	1.16 , 1.34 ±0.5%	1.25 ±0.5%	>80%
H	1.49 , 1.79 ±0.5%	1.64 ±0.5%	>80%
K_s	1.99 , 2.31 ±0.5%	2.15 ±0.5%	>80%

at a pressure level of $\sim 10^{-3}$-10^{-4} Barr). The dewar is then placed inside the FT-IR spectrometer, and a transmission spectrum of the witness is taken at room temperature. After, the witness is cooled down to cryogenic temperatures (-187 °C) using liquid nitrogen. For the cooling, the external windows of the dewar were heated to prevent condensation. When the witness was cooled to a stable temperature, a second transmission spectrum was taken. The witness was then passively warmed up to room temperature, and another transmission spectrum was collected. A background spectrum is always taken before each measurement, and the background subtraction from the witness spectra is done automatically by the FT-IR spectrometer software. However, during these experiments a systematic variation of the background level was detected, which interfered with the background subtraction, and effected the absolute transmission values calculated for the witnesses, but not the wavelength measurements.

Uniformity and angle of incidence

Given that the absolute transmission could not be measured with the FT-IR spectrometer, transmission spectra of the real filters were taken with another spectrometer (Varian Cary5). These measurements were also used to test the uniformity of the coating across the filter's surface, for which spectra were taken at five different points of each filter, i.e. at the four corners and centre. Also, spectra were taken with an angle of incidence of ∼5 degrees, to test the filters' performance at conditions which mimic HAWK-I's optical configuration.

5.2.3 Analysis and Results

The analysis of the data consisted in characterising the shape of the spectra taken for each witness and filter. To that end, several parameters were derived, including the peak transmission, and the wavelengths for the half power and central points. The cut-on and cut-off half power points are calculated as the 50% value between 0 and the peak transmission. For each filter, these parameters were compared to evaluate the consequences of changes in temperature, position and angle of incidence.

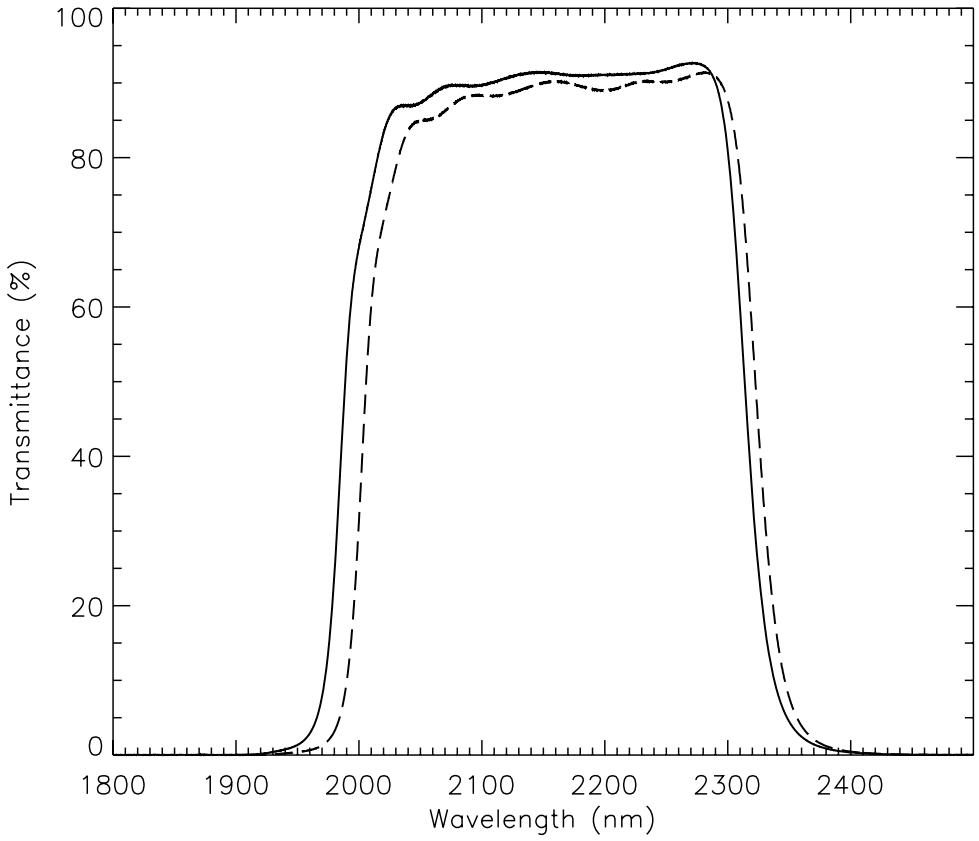

Figure 5.5: Shift in wavelength caused by temperature for a witness measured at room temperature (dashed line) and at cryogenic temperature (solid line). Note that transmission values are not absolute.

A careful analysis revealed the occurrence of a shift in the central wavelength in all the witnesses due to temperature changes, in this case cooling down from room to cryogenic temperature. This shift was always measured to be <1.0%, though not negligible. Figure 5.5 shows the two spectra taken at room and cryogenic temperature for the witness of the K_s filter. As temperature goes from ∼295 to 86 K, the witness shifts shortward by ∼16 nm at 50% cut-on, and ∼8 nm at 50% cut-off. The same comparison was done for the measurements of each filter at different pointings, and with a different angle of incidence. The changes in wavelength were always $\lesssim$0.5%, and considered negligible, confirming the uniformity of the filters.

All the delivered filters were found to be compliant with the specifications. Tables with all the measurements are included, for completeness, in Annex 1. All the filter curves were corrected for the computed change in wavelength caused by the cooling down, since the operating conditions of the filters are at cryogenic temperatures. The shift applied was the value derived in the tests of the respective witnesses. Based on the tests and analysis described, a recommendation was made regarding the filters that

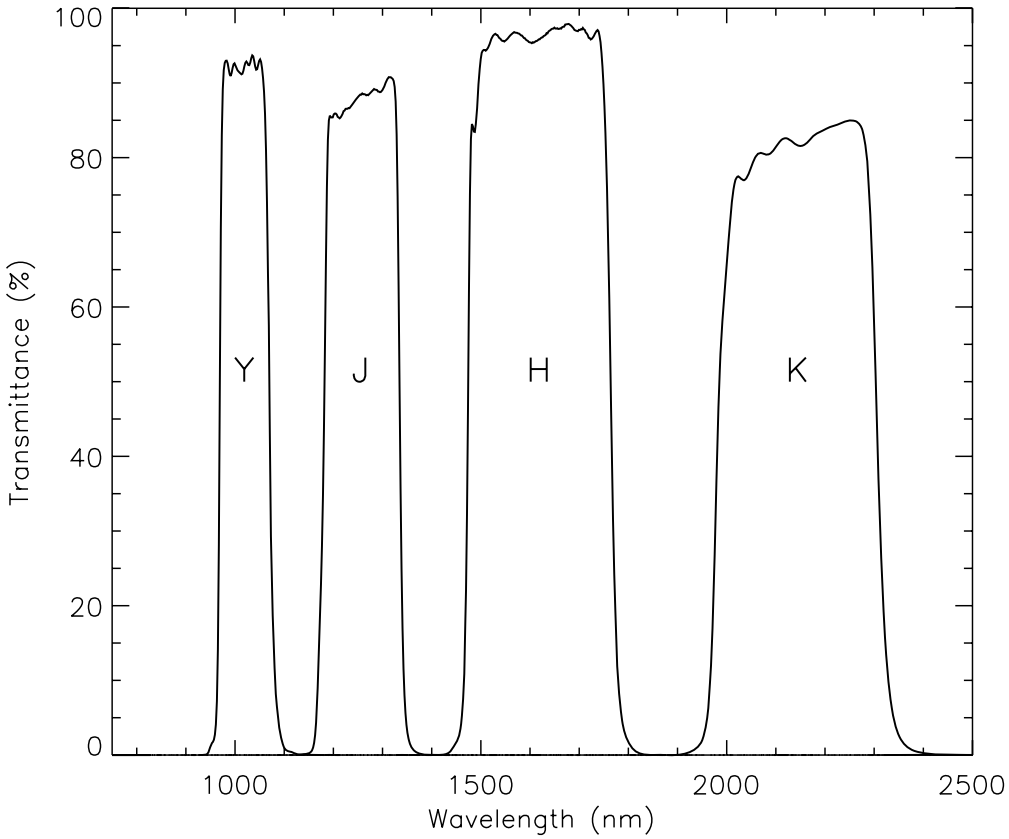

Figure 5.6: HAWK-I broad band filter transmission curves.

showed better performance, and which ones should be used as a backup, or be kept at ESO for future laboratory tests and experiments. The corrected curves for the filters which are now in use at the telescope are shown in Fig. 5.6, and have been made available to the HAWK-I users. A summary of the results derived for these filters is shown in Table. 5.3.

5.3 First commissioning of the instrument

I participated in the first commissioning of HAWK-I, that took place on Paranal between July 31 and August 7. I contributed to the normal operations of the instrument by preparing the observation blocks and assisting in the image acquisition. I was also responsible for studying the orientation of the detectors and determining the pixel scale. Furthermore, using my experience gained with WFCAM data, I have explored the possibility of using 2MASS stars present in the observed fields for the photometric calibration HAWK-I. A summary of the main steps and results of these tests is provided below.

Table 5.3: Results from filter tests.

Filter name	central wavelength [nm]	cut-on (50%) [nm]	cut-off (50%) [nm]	width [nm]	transmission [%]
Y	1021	970	1071	101	92
J	1258	1181	1335	154	88
H	1620	1476	1765	289	95
Ks	2146	1984	2308	324	82

Table 5.4: Relative Orientation of the 4 Detector Quadrants.

Quadrant	Orientation	Angle wrt Q1 [deg]
Q1	101.19 ± 0.02	0
Q2	101.06 ± 0.02	-0.13
Q3	101.15 ± 0.01	-0.04
Q4	101.16 ± 0.03	-0.03

5.3.1 Positioning of the detectors on sky

The accurate measurement of the pixel scale, absolute orientation of the mosaic of detectors on sky, and the relative position of the detectors with respect to each other, is a fundamental step in the characterisation of a new instrument. These are the base parameters on which all the astrometric calibration relies, to convert the pixel coordinates of each detector into accurate positions on sky (in the case of HAWK-I, $\sim$1 milli arcsecond).

Detector orientation and pixel scale

The data were obtained in the second night of observations (01 August 2007), and five images were taken - the first one at origin, the second with telescope offset 50" north, the third with telescope offset 50" east, the fourth with an offset of 50" south, the last offset 50" west (back to origin). Three stars per quadrant were measured on the image at the original position and on the images at the offset positions. The North-East orientation was measured to be pointing along the -X axis, and East along the -Y axis. The average rotation to be applied is 101.16 ± 0.02 deg North of East (clockwise). The average orientation of each of the 4 quadrants is shown in Table. 5.4. The measurement also returned an average pixel scale, calculated under the assumption of precise telescope offsets. The average pixel scale is 0.10643" arcsec/pixel.

Gap between detectors

Using the same set of images and the value found for the pixel scale, the gap between detectors has been determined. The gap was measured at four points in the horizontal axis and four points in the vertical axis. Four stars per quadrant, which were chosen to be close to the detector edge, were measured on the image at the origin position. The

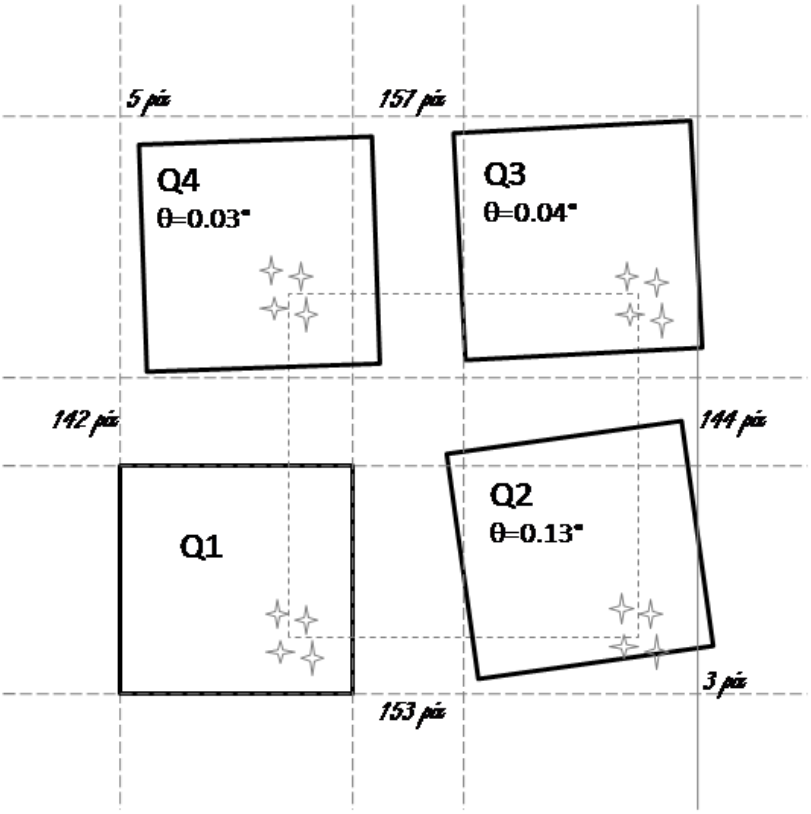

Figure 5.7: HAWK-I gaps between detectors and rotation.

same stars were then measured on the image at the offset position, after the star has moved to another quadrant due to the applied offset. The procedure is repeated for all sky positions. The average values calculated for the gap are 154 pixels (16.4") in the y-axis and 143 pixels (16.3") in the x-axis. The results found are shown in Fig. 5.7.

5.3.2 Photometric calibration using 2MASS stars

One of the first steps in the reduction of astronomical imaging surveys is to relate the signal from the detectors to a meaningful physical quantity. The output of a CCD camera is the number counts of Analog to Digital Units (ADU) per pixel, where ADU is the process of digitalisation of the analogue output of the detector, which is approximately proportional to the number of incident photons. A proper calibration of this relation is needed in order to extract the values for physical flux densities of objects on sky. This is usually done by comparing the photometric observations to known and well calibrated standard stars.

First calibration steps

A sky region of the Galactic Plane (18:01:43.7 -29:57:51.1, J2000 coordinates) was observed and used for photometric calibration. An image was taken in each of the *JHK* HAWK-I filters, with a single detector integration time of 5 seconds (DIT = 5s), which was repeated over 20 exposures (NDIT = 20). This technique avoids the saturation of the detector by bright sources, but most important, improves the signal-to-noise ratio of the observations, in comparison to a single long exposure. A jitter was applied to each of the images (i.e., DIT x NDIT), where the telescope moves by a small offset to a set of positions which vary randomly within a 20 arcsec box. This is later used for sky subtraction, and to get a deeper image which results from adding all the jitter pointings. The main reduction of the images was done using the preliminary test version of the HAWK-I pipeline. After, catalogues of objects were extracted from the reduced images using the source detection algorithm SExtractor. For each object in these catalogues, the flux given in ADUs was multiplied by the detector gain to convert the flux to electrons. The gain for each of the 4 detectors is 1.705, 1.870, 1.735, and 2.110 e^-/ADU. Instrumental magnitudes were then calculated from the flux in electrons using the following expression:

$$Mag_{instrumental} = const. - 2.5\ log10(Flux/t) \quad , \tag{5.1}$$

where the flux is in e^-, and t is the total exposure time given in seconds.

All ground observations suffer from absorption from the atmosphere, which has its minimum at zenith, and increases at positions away from the zenith, since the path light has to travel through the atmosphere is longer. This quantity is usually referred to as *airmass*, which represents a normalised scale of the path length with respect to the zenith. Furthermore, the intensity of the light coming from a star that is collected at the instrument is affected by scattering when it passes through the atmosphere. The combination of these two effects, atmospheric absorption and scattering, on the flux of star received on a ground telescope is wavelengths dependent and is referred to as extinction. Concluding, the measured instrumental magnitude of a star is a combination of these effects:

$$Mag_{instrumental} = Mag_{star} + Extinction_{\lambda}\ .\ Airmass \quad . \tag{5.2}$$

The extinction term is usually stable throughout the night and mean extinction values are commonly used.

The next step in the calibration of the photometry, is to bring the magnitude values into a standard system, which is done by a linear relation between the instrumental magnitudes and those of known standard stars. However, to derive this relation, the instrumental magnitudes must be extinction corrected. A first approximation of the *Zero Point* (ZP) between the two systems is given by:

$$ZP \ \sim \ Mag_{standard} - Mag_{instrumental} \quad . \tag{5.3}$$

However, one more term needs to be considered in this transformation, which is the colour term (CT). The colour term is a constant which applies a correction as a function of spectral type. It is usually calculated by regressing the differences between the standard and extinction corrected instrumental magnitudes, and a set of standard star's colours between two different filters. The transformation from instrumental to photometric calibrated magnitudes is then given by:

$$Mag_{calibrated} = Mag_{instrumental} + ZP + CT\ .\ Colour + ExtinctionTerm \quad . \quad (5.4)$$

Choice of standard system

There are several standard photometric systems which have established for different observatories, detectors, and wavelengths bands (see the review by Bessell (2005). A standard system consists of a list of stars spread over the sky, which are known not to vary in brightness, and for which precise magnitudes and colours corrected for extinction are available. The photometric standard stars used for calibration of near-IR broad band imaging done, for example, at ISAAC/VLT, are usually taken from the list of the UKIRT Faint Standards[1](Hawarden et al. 2001) or the Persson list of standards[2] (Persson et al. 1998), and are measured before, between, and after the observations. However, in a 2 seconds exposure with HAWK-I, the saturation limit is reached for stars with 11.0, 11.3, and 10.2 magnitudes, for *J*, *H*, and K_s-bands, respectively. This means that most of the standard stars are saturated even in short exposures. Therefore, another calibration system must be considered.

I have looked at the possibility of using the 2MASS all-sky point-source catalogues (Cutri et al. 2003), which have photometry consistent to ∼1% (Nikolaev et al. 2000), as calibrators for HAWK-I. The idea originated from the fact that the wavelength operating range and sensitivity of HAWK-I resemble those of WFCAM, where the photometric calibration is already being done with 2MASS stars present in the observation fields (see Sect. 2.1.3). 2MASS point-source catalogues were retrieved for the HAWK-I calibration field, only considering stars with magnitudes between 12.5 and 14.0 in *J,H,K*, and errors less than 0.1 magnitudes. In the four quadrants there are over ∼400 2MASS stars which satisfy these criteria, and these were used to derive the magnitude zeropoints for the HAWK-I broad-band *J,H,K* filters. For all these stars, the J_{2MASS}-H_{2MASS} and J_{2MASS}-K_{2MASS} colours were computed. The HAWK-I instrumental magnitudes were corrected for extinction using the atmospheric extinctions for Paranal[3], which for *J,H,K* are 0.11, 0.06 and 0.07 magnitudes per airmass, and the airmass at the time of observations, which was taken to be the average between the airmass at the start and at the end of the observations for each filter (1.34, 1.22, and 1.14 for *J,H,K*, respectively). The zero points and colour terms were calculated

[1]http://www.jach.hawaii.edu/UKIRT/astronomy/calib/phot_cal/fs_extended.html
[2]http://www.naoj.org/Science/Resources/standards/persson.html
[3]http://www.eso.org/sci/facilities/paranal/instruments/isaac/tools/imaging_standards.html#Extinction

by computing a linear regression from the difference between 2MASS and instrumental magnitudes, and the colours of the 2MASS stars. From the best fit of the linear regression, the zero-point (simple shift of all the magnitudes vertically by a constant amount), and the slope (the colour term) are computed with an accuracy of 0.05 units. The 2MASS photometry is transformed into HAWK-I system using the following equations:

$$J_{HAWK-I} = J_{instrumental} + 26.86 + 0.14(J_{2MASS} - H_{2MASS}) + ExtinctionTerm \quad , \quad (5.5)$$

$$H_{HAWK-I} = H_{instrumental} + 27.28 - 0.26(J_{2MASS} - H_{2MASS}) + ExtinctionTerm \quad , \quad (5.6)$$

$$K_{HAWK-I} = K_{instrumental} + 26.30 - 0.14(J_{2MASS} - K_{2MASS}) + ExtinctionTerm \quad , \quad (5.7)$$

where the zero point and the colour terms are given in electrons per second.

5.4 Current state of HAWK-I

The excellent optical and throughput performances, together with the large field of view make it the most efficient near-infrared imager on 8 to 10m class telescopes to date. The instrument was commissioned and the science verification programmes conducted in 2007. HAWK-I has been offered in the ESO call for proposals in September 2007 and has started regular operation on April 1st, 2008 (Period 81) where already 21 runs were scheduled. The science verification covered a large variety of research fields, intended to demonstrate the instrument capabilities. These included studies of distant galaxies, clusters of galaxies, star clusters, and star formation.

In the star formation area, different projects have been conducted during the Science Verification runs. HAWK-I was used to observe NGC 602/N 90, in the Small Magellanic Cloud (SMC), which hosts young stellar objects and Class 0 protostars, detected by ACS/HST and IRAC/Spitzer. HAWK-I data were used to construct SEDs of these sources, which revealed fundamental to study the nature of these objects. Another project targeted the Carina Nebula to study the physics of massive star formation and its feedbacks. The HAWK-I data revealed young stars seen through extinction as high as $A_v = 25$ magnitudes, and brown dwarfs down to 35 Jupiter masses through 10 magnitudes of extinction. Deep observations of the Chamaeleon I star-forming region, complete to 5 Jupiter masses, reached an internal astrometric precision better than 25 milli-arcseconds. A second epoch of observations taken 3 years from these observations can reveal the proper motions of all the Chamaeleon members. These results have been briefly discussed by (Kissler-Patig et al. 2008a), and will certainly be soon reported in refereed journals.

Chapter 6

Research in progress

The projects presented in the previous chapters, the variability survey of young stellar objects and the subsequent spectroscopic follow-up for a sample of candidate members of ρ Ophiuchi, are only some of the applications of this large dataset, unique in this star forming region. The unprecedented sensitivity of the WFCAM over large areas on the sky has already shown its potential in the area of star formation (e.g. Lodieu et al. 2007). It is a very interesting step to combine all the epochs from the variability study to get a single deep image of ρ Ophiuchi which would be the deepest near-IR image of this star forming region over such a large scale. The combination of this dataset with Spitzer data recently released to the public (see Sect. 2.2), is ideal to search for very low mass stars and brown-dwarfs members of this molecular cloud, using the state-of-art instruments for the study of young objects in the IR. In this chapter, I highlight the main aspects of this project, which I have already begun to develop beyond the work presented in this thesis.

6.1 Deep-stack of the ρ Ophiuchi cluster

All the WFCAM image data in Ophiuchus were taken at the same sky pointings and set of filters over the several observing blocks that were presented in Sect. 2.1.1. Thus, it is relatively straightforward to stack these data to produce final deep images, with the main difficulty arising from dealing with such large amounts of data. The stacking of all the images was done by the WFCAM Science Archive (WSA), where all the quality data were combined into a final mosaic made up of the four pointings, for each filter. In each year of observations, there was one night where the microstepping mode was used, and to avoid complexity these have not been included in the deep stacks. The deep images contain therefore 11 nights in K, and 12 nights in H. The catalogue production was also performed at the archive. All the necessary information is contained in FITS catalogues which need, however, some further treatment since they are not yet the final database tables. The FITS catalogues contain un-calibrated fluxes that can be converted to calibrated magnitudes using the information in the FITS header. This

was done with the following calculations (nomenclature according to CASU):

- instrumental magnitude (instMag):

$$instMag = -2.5 * log_{10}\,(flux) \tag{6.1}$$

- extinction correction (extCorr):

$$extCorr = -EXTINCT * \left(\frac{AMSTART + AMEND}{2} - 1\right) \tag{6.2}$$

- exposure correction (texpCorr):

$$texpCorr = 2.5 * log_{10}(EXP\_TIME) \tag{6.3}$$

- and finally, the calibrated magnitude(calMag):

$$calMag = instMag + magZpt + extCorr + texpCorr - aperCor \tag{6.4}$$

where,

- AMSTART = Airmass at start of observation
- AMEND = Airmass at end of observation
- EXP_TIME = Integration time per exposure
- APCOR = Stellar aperture correction
- MAGZPT = Photometric ZP (mags) for default extinction
- EXTINCT = Extinction coefficient (mags)

The deep stacks are composed of frames taken at a variety of airmasses and extinctions, and so an average value over all the nights has been taken for the calculations. Other steps in assuring the reliability of the final catalogue will include most of the steps described in Sect. 2.1.3. Figure 6.1 shows the H-band mosaic of the combined data. The spatial resolution and deep exposure make this image the first of its kind over the Ophiuchus Molecular Cloud.

Figure 6.1: ρ Ophiuchi very deep H-band image, combining 12 epochs of observations. The cloud structure is seen with an unprecedented detail in this region.

6.2 Candidate low-mass stars and brown dwarfs

One of the mains goals of this project is to obtain a more complete census of the young stellar populations in the regions of the cloud where the density is higher, specially to identify candidate brown-dwarfs in the ρ Ophiuchi cluster. Using the deep stack of WFCAM data, fainter magnitude limits can be achieved ($H \lesssim 21.0$ and $K \lesssim 20.0$) than with the individual catalogues used for the variability study. However, such sensitivity brings a major challenge to this study, which is to quantify and avoid background contamination. For that, an analogous strategy to that used by Allen et al. (2002) will be used. In that work, a NICMOS/HST J and H survey was done over small areas of high extinction of Ophiuchus. The limiting magnitudes were comparable to the ones from the WFCAM data. Allen et al. (2002) show that if the column density of molecular gas (measured in Ophiuchus, for example, by Wilking & Lada (1983) using $C^{18}O$ and ^{12}CO observations) is convolved with the Galactic model of Wainscoat et al. (1992), the number of estimated background sources decreases to 0.50 stars arcmin^{-2} for regions with $A_V = 40$ mag, and 0.02 stars arcmin^{-2} for regions with $A_V = 80$ mag. This is shown in Fig. 6.2 taken from Allen et al. (2002), where the distribution of stars predicted by the Wainscoat's models and convolved with the Ophiuchus extinction map is displayed. Therefore, if the WFCAM study is restricted to high extinction areas, the contamination by background sources seen through the cloud should be very low, and evidence for young candidate members can be found using colour-magnitude diagrams. Furthermore, the combination with Spitzer data on this region, will allow nearly complete information over the near- and mid-IR spectral energy distribution of these objects. Luhman & Rieke (1999) have argue that the Initial Mass Function of Ophiuchus should contain a large number of substellar objects, though so far only $\sim$22 brown dwarfs have been confirmed in this star forming region (see Sect. 3.9). This WFCAM study could uncover new brown dwarfs candidates, which would enable a more accurate study of the low-mass end of the IMF of Ophiuchus.

6.3 Morphologies of young stellar objects

Given the high spatial distribution of the WFCAM deep image, the morphology of some known young stellar objects is revealed, showing features previously not observed. An example of an interesting object is shown in Fig. 6.3. *GY 344 (AOC J162745.76-244453.3)*, is a known member of Ophiuchus and the WFCAM images reveal its almost edge-on disc. The large apparent size of the disc can be explain by the shadow of a much smaller disc which is projected into the surrounding dust of the molecular cloud.

The unprecedented combination of high resolution and sensitivity achieved in the WFCAM deep image unveils many other structures in young objects which have been previously unresolved, and will be studied as a future project.

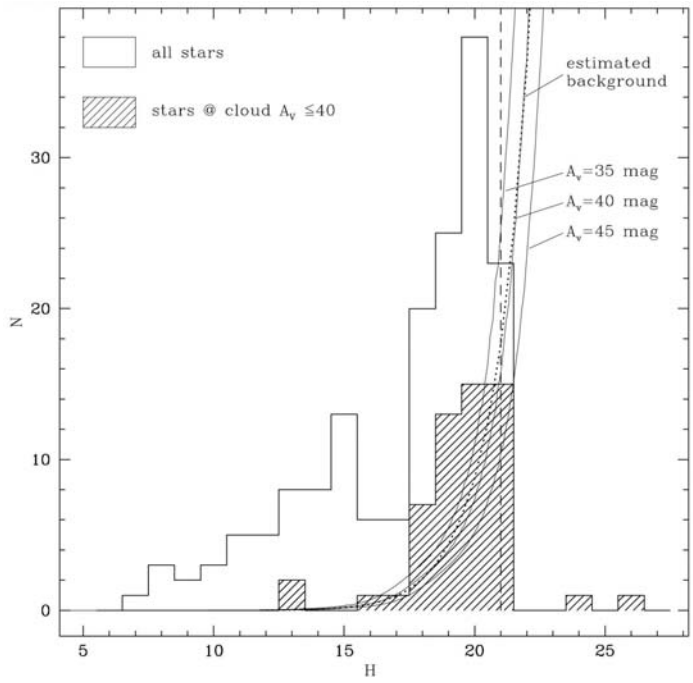

Figure 6.2: The plot is from Allen et al. (2002), a NICMOS/HST study over small areas of ρ Ophiuchi, and shows the distribution of the H magnitudes. The solid curves show the estimated background contamination using the Galatic model of Wainscoat et al. (1992), convolved with an extinction map of Ophiuchus for different A_V.

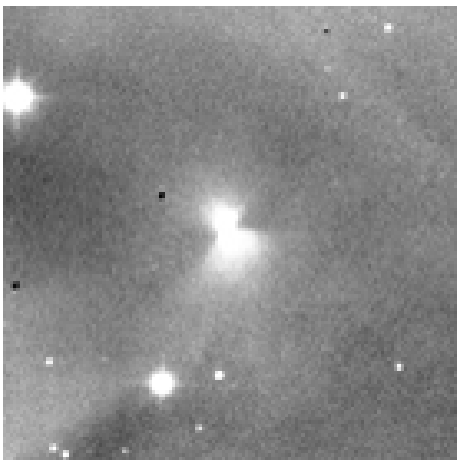

Figure 6.3: WFCAM image of *GY 344* which reveals the existence of an almost edge-on disc, which is seen has a projected shadow in the surrounding dusty cloud material.

Chapter 7

Summary and outlook

T Tauri stars were discovered nearly 60 years ago because of their variability, marking the start of observational research of star formation in our Galaxy. From that point until the present day, a consensus picture of how stars form out of molecular clouds and evolve into the main-sequence has emerged, though many elements of this process are not yet understood. The recent developments of astronomical instrumentation on ground and space have provided scientists with myriads of new information and access to the whole electromagnetic spectrum. The conciliation between the results originating from all these observations, and a consistent theoretical frame, is the current goal of research in many areas of star formation. Large observational studies, such as the one presented in this thesis, can provide sufficient number statistics to consistently derive the properties of a particular class of objects, on which the basis of a theoretical framework can rely. At the present time, many mechanisms of the star formation process remain unexplained. For example, the role and evolution of magnetic fields in young stars and their circumstellar accretion discs, the stellar angular momentum evolution, or the structure of the inner disc where star-disc interaction occurs by the means of magnetospheric accretion. The answer to these problems has an interest on its own, but moreover is a fundamental key in understanding the scenario of the formation of planetary systems. Furthermore, the observational discovery of the first brown dwarfs and extrasolar planets in 1995, means star formation theories must also be able to explain the physical processes dominating at the lower-mass end.

The work presented in this thesis looks at one of the defining characteristics of young stellar objects, photometric variability, in an attempt to better describe the influence that magnetic field regions and/or accretion discs may have in the light emitted by a star- or brown dwarf-disc system. To that end, the stellar population of the young ($\sim$1 Myr) and nearby ($\sim$119 pc) cluster ρ Ophiuchi was studied in terms of its variability properties in the near-IR regime. In this study other variable stars were uncovered, which show characteristics consistent with being also part of this cluster, with low, but not negligible, probability of contamination by field stars or extragalactic objects.

The core dataset for this project consisted of near-IR photometric time-series observations conducted with the Wide Field Imager (WFCAM) at the United Kingdom Infrared Telescope (UKIRT) on Mauna Kea, Hawaii. These observations allowed the extraction of a list of variable objects for which the time dependence of their brightness was studied. This list included part of the known population of Ophiuchus, but also previously unclassified stars. By studying its characteristics, it was possible to relate variability to possible physical mechanisms taking place in the stellar surface and circumstellar environment. Complementary to the variability survey, a search for mid-IR excesses has been conducted using mid-IR photometry from the Infrared Array Camera (IRAC) and the Multiband Imaging Photometer (MIPS) on board of Spitzer space telescope. In combination with the WFCAM data, IR excesses were detected for approximately half of the variable objects. This information was used to study the relation of the variability characteristics to the detection of IR excess, which is an indicator of the presence of a circumstellar disc. X-ray emission in young stellar objects is intrinsically related to near-IR variability, since both phenomena depend on the stellar magnetic fields. X-ray studies of Ophiuchus present in the literature were studied, and it is found that stars with previously detected X-ray variability, are also found to be variable in this near-IR survey. Finally, a near-IR low-resolution spectroscopic follow-up was carried out at the New Technology Telescope (NTT) with the spectrograph SofI, with the intent of clarifying the nature of a sample of variable stars which have not previously been associated with the population of the ρ Ophiuchus cluster.

7.1 Variability in young stellar objects

Despite the $\sim$Myr timescales involved in the early evolution of young stars, there are physical processes which have timescales comparable to those of human lifetime. Young stars have been found to rotate with periods in the order of days, offering to an observer the opportunity to study different regions of its surface. Cool spots exist on the surface of young stars and, in analogy to sunspots, are regions of lower temperature than the stellar photosphere, which have intense magnetic activity. As the star rotates, the spots cause rotational modulation of the stellar flux. For stars surrounded by circumstellar discs, hot spots (regions with higher temperature than the stellar photosphere, interpreted as the impact points on the stellar surface from disc accretion through magnetic field lines), structural features of the inner disc (as, for example, a warped inner disc), or inhomogeneous distribution of circumstellar material, can cause photometric variability from rotational modulation of the star, or by variations in the accretion rate of material onto the star. These processes represent the potential ideas which were developed to explain the variability observed mainly in optical wavelengths, where most of the photometric monitoring has been done. However, characterisation of these phenomena in the IR regime, more suitable to probe the circumstellar disc temperature regime, is still largely missing. Furthermore, using IR wavelengths it is

possible to penetrate into the cloud and detected stars which are not accessible in the optical.

In the near-IR photometric monitoring campaign conducted in this thesis, 137 variable stars were extracted from catalogues containing ∼16000 sources. Fifty seven of these are known to be members of ρ Ophiuchi, which represents approximately half of the known population of these cluster which is detected within the spatial and magnitude limits of the WFCAM dataset. In a survey of the Trapezium region of the Orion Nebula Cluster (ONC, at a distance of ∼400 pc), done by Carpenter et al. (2001) with the 2MASS, the authors find ∼45% of the cloud members with K<11.0 to be variable, but only ∼14% of the cloud members with K>12.0 show variability, which they claim to be due to an increase in photometric noise at the fainter limits, and not to the fainter cloud members being intrinsically less variable. The WFCAM data provides excellent photometry at this wavelengths, with average errors ∼0.01 magnitudes up to K∼15.0. Therefore, in the magnitude range of the known variable members ($10.0 \lesssim K \lesssim 15.0$), the levels of photometric noise are uniform and this question can be addressed. It is observed that the fraction of variable stars as a function of magnitude closely follows that of the number of members. Thus, there is no indication that the frequency of variable member stars depends on the magnitude.

The light curves of the variable stars have revealed a variety of behaviours, with variability found on intermediate (within only one year of observations) and long (across the two years of observations) timescales, colourless variability as well as stars that get redder when faint, and stars that get bluer as they fade, and extreme variability. The mean peak-to-peak photometric fluctuations in H and K is ∼0.2 magnitudes, and the mean H- K colour variation is ∼0.16 magnitudes. The variability characteristics can be used to constrain the mechanisms responsible for the observed variations for each object. This was done by comparing the properties of each star, such as the amplitude of the variations and the correlation between magnitude and colour variations, to the expected parameters derived by models of spots and discs from the literature. Stars with low amplitudes often showed colourless variations, and had no IR-excess, which are the characteristics expected for stars whose variations are caused by the rotational modulation by cool spots on the stellar surface. 23% of the variable stars have variability consistent with this scenario. A fraction (∼30%) of the stars with larger colour variations and colours becoming redder as the object fades, show variations consistent with hot spots or variations in circumstellar extinction.

Changes in an accretion disc are another potential mechanism which can cause variability. The existence of a warped inner disc which co-rotates with the star, or changes in the accretion rate from the disc to the star along magnetic-field lines, could explain the correlations with a negative slope in the K vs. H-K colour magnitude diagram, which represent stars which became bluer as they fade. This effect as never been observed in optical variability studies, and only reported in IR obser-

vations (Carpenter et al. 2001; Eiroa et al. 2002), further supporting the hypothesis that the origin of the changes lies in the circumstellar disc and not in the stellar photosphere. However, many variable stars (∼30%) show variability with large colour variations which cannot be explain by any of these models. The same is found by (Carpenter et al. 2001) in the ONC. This provides two independent pieces of evidence that more extreme events or alternative mechanisms must occur in young stars. A recent optical variability study which combined ∼20 years of observations of weak-line T Tauri stars (Grankin et al. 2008), claims that the observed variations for 4 stars with more extreme amplitude variations can be explained by considering a fractional coverage by spots of the visible stellar photosphere >30%, which is the maximum value imposed from previous variability studies done in the optical. Therefore, the explanation of near-IR extreme variables might arise by allowing larger fractional coverage of cool spots in the stellar surface. For stars surrounded by circumstellar discs, as Classical T Tauri stars, hot spots, variations in circumstellar extinction, and structural changes in the inner disc, could be operating together producing variations which are the net result of all these contributions.

Finally, an extreme object was found with a brightening of ∼3 magnitudes from the first to the second year. This type of variations in the IR are extremely rare, especially given that the star is bluer when fainter by >1 magnitude. This star is a known member of Ophiuchus with active accretion, and the variability observed must express a large event related to accretion instabilities. This was the only object, out of ∼16000 detections in the whole WFCAM field, which showed such a large magnitude change. A spectroscopic follow-up of this object is needed to clarify the nature of its large brightness variations.

7.2 Spectroscopy of candidate young stars

The analysis of the variability did not provide evidence that all the variable candidate members represented a different population from the ρ Ophiuchi confirmed members, since they show similar timescales of variability, as well as magnitude and colour changes. An assessment was made to identify the possible extent of contamination from other classes of variable objects, namely, stars in the Asymptotic Giant Branch (AGB-stars), variable Active Galactic Nuclei (AGN), and active M dwarfs. The contamination levels were found to be low, though not negligible, with the following estimated numbers of contaminants within one square degree of the WFCAM observations: < 1 AGB star/long-period variable, 9 variable AGN, and 30 active M dwarfs.

Low-resolution spectroscopy was used to study water vapour features in the near-IR spectra of a sample of candidate variable stars, with the aim of determining their spectral type and look for signatures of youth. For 5 objects which show clear H_2O

absorption, a defining IR spectral feature for stars with spectral type later than ∼M1, reliable spectral types were determined by fitting reference spectra of known young stars. Their spectral types range from M2 to M5. One of these objects is a previously known member of Ophiuchus. Spitzer thermal excesses, X-ray emission, and variability characteristics are used to investigate the youth of these objects. Two objects with an assigned spectral type M3 did not show youth characteristics in the diagnostics used, which does not excluded them as young, given the limitations of the criteria used. Three objects show signs of youth but their spectral type could not be determined (most likely <M1). Two objects (plus the star known to be a member) show IR excess or X-ray emission characteristic of young stellar objects. The two spectroscopically confirmed objects, with spectral types M5 and M2, represent new *bona-fide* members of the ρ Ophiuchi cluster found through variability. The colour-magnitude diagram for the derredened magnitudes has been used as an indication of their masses, which should be above the deuterium burning limit. For the other objects with spectroscopy, since they did not show water vapour absorption features in their spectra, they should have spectral types earlier than <M1, and spectroscopy at other wavelengths is needed to classify them. This does not exclude them though, from being candidate members of Ophiuchus.

7.3 IR instrumentation and its importance in Star Formation

The variability survey presented in this thesis was only possible due to the development of IR instrumentation for astronomy, and in particular the new near-IR imager, WFCAM. The increasing sensitivity of IR imagers allows for new science cases to be investigated. An example is the new High-Acuity Wide-field K-band Imager (HAWK-I) presented in this thesis, which combines a mosaic of IR detectors to achieve a large field of view on sky (7.5' x 7.5') in an 8-meter class telescope, the ESO Very Large Telescope (VLT). The contribution of HAWK-I to star formation studies will be seen in several fields, such as the study of jets, accurate measurement of proper-motions, or the detection of brown dwarfs at the Deuterium burning limit. The contribution of such an instrument for variability studies is presented in the next section, which provides an outlook of future projects and implications from the work presented in this thesis.

7.4 Outlook

In the presented work, variability characteristics of known young stars, as well as candidate pre-main-sequence stars, have been determined. The inclusion of the time domain

in the study of young stars has been shown to be fundamental to better understand the ongoing physics in these objects. As with any large observational survey, the initial work provides the solid ground for smaller follow-up projects. In this sense, the work presented is valuable since it uncovered stars for which, from the study of photometric variations alone, phenomena related to the star-disc interaction can be investigated. A detailed study of stars for which signatures of magnetospheric accretion and inner disc changes were found is now possible, and can yield a new input to the understanding of the inner disc structure. There is a growing interest on what can be learned from variability studies of young stellar objects. As an example, one of the white papers for the Spitzer Warm mission is a proposal to carry out a mid-IR variability study of young stars from space, with the main scientific objective of better understanding the physics involved in the interaction between an accreting star and its surrounding disc. Other current projects in variability include the WFCAM surveys in Cygnus OB2 (M. M. Guimaraes, private communication), and the Orion Nebula Cluster (briefly mentioned in Chapter 2). These studies will enable a comparison of the properties of young variable stars for different star forming regions.

The identification of significant amplitude variations of three known brown dwarfs is an important result, and a project to use either ESO telescopes, or the WFCAM, for a photometric follow-up is foreseen. The study of the substellar angular momentum evolution still lacks important determinations of rotation rates and periods. A photometric monitoring campaign of these objects can be carried-out in few nights (since the known periods of brown dwarfs have a duration of only ∼hours) and will provide both the first period determination for brown dwarfs in this cluster which is only ∼1 Myr old, and a more detailed study of their activity indicators.

Reaching a complete census of a cluster's population and the determination of the low-mass end of the IMF is one of the main goals of today's research in star formation. Large-scale surveys are being conducted in many star forming regions with the goal of searching for the origin of brown dwarfs, and their relationship to planets. One of such studies is being started at the Laboratoire d'Astrophysique de l'Observatoire de Grenoble (LAOG) targeting the ρ Ophiuchi cluster using multi-wavelength photometry and spectroscopic follow-ups. The results presented in this thesis will therefore provide additional information for this study, and contribute for constraining theoretical evolutionary models.

7.5 The uniqueness of this thesis

This study is the first near-IR variability survey of a star forming region reaching faint magnitude limits ($H\sim19$ and $K\sim18$) and covering such a large area on sky (~0.8 deg^2). Prior to this work, only two near-IR variability studies of entire clusters have ever been done (Carpenter et al. 2001, 2002). It is also the first deep IR survey encompassing a

large area of ρ Ophiuchi, which will provide the scientific community with a database of IR magnitudes for all sources brighter than $K = 18$, with importance comparable to that of the 2MASS legacy for this region. The identification of variable stars in Ophiuchus with such sensitivity is a pioneering result, and will provide the targets for future follow-up studies of variable young stars.

Furthermore, I was one of the first scientists to use data from the WFCAM, which represented an additional challenge in the reductions of the data, since the very first versions of the pipeline were still of poor quality. I have developed many routines to improve the data reductions and I provided the pipeline and archive teams with my feedback as a user. The fact that not a single instrumental artifact showed up in the list of variables shows the success of my commitment to assure the quality in the final data catalogues. Furthermore, I was the first to analyse data of IRAC/Spitzer in Ophiuchus, from observations conducted by the c2d team, which were made available to the public during this project.

As part of my thesis work, I had also the opportunity to contribute to the development and commissioning of HAWK-I, and to witness its very first light.

Appendix A

Filter measurements

Y filter

		Spec.	Centre (±1nm)	Extr.1 (±1nm)	Extr.2 (±1nm)	Extr.3 (±1nm)	Extr.4 (±1nm)	Incidence: θ=5° (±1nm)	Max. λ shift from centre
Y 1	50% cut-on	970±5nm	971	972	971	970	971	969	∼0.2%
Iz881	(nm)		(∼0.1%)						
SN001	50% cut-off	1070±5nm	1073	1075	1073	1071	1073	1071	∼0.2%
	(nm)		(∼0.3%)						
Y 2	50% cut-on	970±5nm	971	971	972	972	971	969	∼0.2%
Iz881	(nm)		(∼0.1%)						
SN002	50% cut-off	1070±5nm	1072	1072	1074	1074	1072	1070	∼0.2%
	(nm)		(∼0.2%)						
Y 3	50% cut-on	970±5nm	970	971	971	970	970	968	∼0.2%
Iz881	(nm)		(∼0.0%)						
SN003	50% cut-off	1070±5nm	1071	1072	1073	1072	1072	1069	∼0.2%
	(nm)		(∼0.1%)						

		Spec.	T=295K (δ=±0.1nm)	T=87K (δ=±0.1nm)	λ shift (cooling down)
Witness	50% cut-on	970±5nm	967	966	∼0.1%
X1-3827	(nm)		(∼0.3%)		
S5220	50% cut-off	1070±5nm	1069	1068	∼0.1%
S5233	(nm)		(∼0.1%)		

		Spec	Measurements
Y 1	Ave %T btw. 90%	90%	91.57%
Iz881	min %T btw. 90%	80%	85.54%
SN001	%T < .01% Range	500-2600nm	500-939, 1164-2360 (nm)
			leak %T<0.05%:2360-2556 (nm)
Y 2	Ave %T btw. 90%	90%	91.84%
Iz881	min %T btw. 90%	80%	85.69%
SN002	%T < .01% Range	500-2600nm	500-928, 1168-2356 (nm)
			leak %T<0.05%:from 2356nm on
Y 3	Ave %T btw. 90%	90%	91.93%
Iz881	min %T btw. 90%	80%	85.86%
SN003	%T < .01% Range	500-2600nm	500-926, 1172-2352 (nm)
			leak %T<0.05%:from 2355nm on

J filter

		Spec.	Centre (±1nm)	Extr.1 (±1nm)	Extr.2 (±1nm)	Extr.3 (±1nm)	Extr.4 (±1nm)	Incidence: θ=5° (±1nm)	Max. λ shift from centre
J 1	50% cut-on	1170±5.8nm	1188	1184	1183	1185	1186	1186	∼0.4%
X1-3777-P1	(nm)		(∼1.5%)						
S1-333-P1	50% cut-off	1330±6.6nm	1347	1342	1342	1344	1344	1345	∼0.4%
	(nm)		(∼1.3%)						
J 2	50% cut-on	1170±5.8nm	1182	1180	1182	1180	1178	1180	∼0.3%
X1-3778-P1	(nm)		(∼1.0%)						
S1-334-P1	50% cut-off	1330±6.6nm	1336	1334	1336	1334	1332	1334	∼0.3%
SN012	(nm)		(∼0.5%)						
J 3	50% cut-on	1170±5.8nm	1182	1179	1179	1179	1179	1180	∼0.3%
X1-3778-P1	(nm)		(∼1.0%)						
S1-334-P1	50% cut-off	1330±6.6nm	1336	1332	1334	1334	1333	1334	∼0.3%
SN013	(nm)		(∼0.5%)						

		Spec.	T=295K (δ=±0.1nm)	T=87K (δ=±0.1nm)	λ shift (cooling down)
Witness1	50% cut-on	1170±5.8nm	1174	1173	∼0.1%
X1-3777-P1	(nm)		(∼0.3%)		
S1-333-P1	50% cut-off	1330±6.6nm	1334	1332	∼0.1%
	(nm)		(∼0.3%)		
Witness2	50% cut-on	970±5.8nm	1185	1184	∼0.1%
X1-3778-P1	(nm)		(∼1.3%)		
S1-334-P1	50% cut-off	1330±6.6nm	1340	1339	∼0.1%
	(nm)		(∼0.8%)		

		Spec	Measurements
J 1	Ave %T btw. 90%	90%	88.90%
S1-233	min %T btw. 90%	80%	84.50%
X1-3686	%T < .01% Range	500-3000nm	500-928, 1008-1134, 1416-3000 (nm) leak %T<0.3%:930-1006
J 2	Ave %T btw. 90%	90%	87.75%
S5-235-1	min %T btw. 90%	80%	82.38%
X1-3834	%T < .01% Range	500-3000nm	500-1126, 1402-3000 (nm)
J 3	Ave %T btw. 90%	90%	87.10%
S5-235-3	min %T btw. 90%	80%	81.59%
X1-3834	%T < .01% Range	500-3000nm	500-1128, 1400-3000 (nm)

H filter

		Spec.	Centre (±1nm)	Extr.1 (±1nm)	Extr.2 (±1nm)	Extr.3 (±1nm)	Extr.4 (±1nm)	Incidence: θ=5° (±1nm)	Max. λ shift from centre
H 1	50% cut-on	1490±7.5nm	1501	1505	1508	1509	1506	1499	∼0.5%
S1-233	(nm)		(∼0.7%)						
X1-3686	50% cut-off	1780±8.9nm	1786	1793	1796	1796	1793	1784	∼0.6%
	(nm)		(∼0.3%)						
H 2	50% cut-on	1490±7.5nm	1477	1476	1476	1475	1475	1475	∼0.1%
S5-235-1	(nm)		(∼0.9%)						
	50% cut-off	1780±8.9nm	1767	1767	1767	1766	1766	1765	∼0.1%
	(nm)		(∼0.7%)						
H 3	50% cut-on	1490±7.5nm	1472	1470	1472	1470	1469	1470	∼0.2%
S5-235-3	(nm)		(∼1.2%)						
	50% cut-off	1780±8.9nm	1759	1758	1760	1759	1756	1756	∼0.2%
	(nm)		(∼1.2%)						

		Spec.	T=295K (δ=±0.1nm)	T=87K (δ=±0.1nm)	λ shift (cooling down)
Witness1	50% cut-on	1490±7.5nm	1497	1495	∼0.3%
S1-233	(nm)		(∼0.4%)		
X1-3686	50% cut-off	1780±8.9nm	1781	1780	∼0.1%
	(nm)		(∼0.1%)		
Witness2	50% cut-on	1490±7.5nm	1458	1456	∼0.1%
S5-235	(nm)		(∼2.1%)		
X1-3834	50% cut-off	1780±8.9nm	1740	1738	∼0.1%
	(nm)		(∼2.2%)		

		Spec	Measurements
H 1	Ave %T btw. 90%	90%	96.65%
S1-233	min %T btw. 90%	80%	89.17%
X1-3686	%T < .01% Range	500-3000nm	500-1434, 1886-3000 (nm)
H 2	Ave %T btw. 90%	90%	96.11%
S5-235-1	min %T btw. 90%	80%	88.16%
X1-3834	%T < .01% Range	500-3000nm	500-1410, 1816-3000 (nm)
H 3	Ave %T btw. 90%	90%	95.58%
S5-235-3	min %T btw. 90%	80%	85.83%
X1-3834	%T < .01% Range	500-3000nm	500-1414, 1848-3000 (nm)

K_s filter

		Spec.	Centre (±1nm)	Extr.1 (±1nm)	Extr.2 (±1nm)	Extr.3 (±1nm)	Extr.4 (±1nm)	Incidence: θ=5° (±1nm)	Max. λ shift from centre
Ks 1	50% cut-on	1990±10nm	1998	1999	2000	2001	1998	1996	∼0.2%
T-2479	(nm)		(∼0.4%)						
T-2481	50% cut-off	2310±11.5nm	2306	2308	2309	2310	2306	2304	∼0.2%
	(nm)		(∼0.2%)						
Ks 2	50% cut-on	1990±10nm	1994	1996	1996	1996	1996	1992	∼0.1%
T-2480	(nm)		(∼0.2%)						
T-2482	50% cut-off	2310±11.5nm	2320	2324	2324	2323	2323	2319	∼0.2%
SN002	(nm)		(∼0.4%)						
Ks 3	50% cut-on	1990±10nm	1999	2000	2000	2002	2002	1997	∼0.2%
T-2480	(nm)		(∼0.5%)						
T-2482	50% cut-off	2310±11.5nm	2305	2308	2307	2308	2308	2303	∼0.1%
SN005	(nm)		(∼0.2%)						

		Spec.	T=295K (δ=±0.1nm)	T=87K (δ=±0.1nm)	λ shift (cooling down)
Witness1	50% cut-on	1990±10nm	2004	1988	∼0.8%
T-2479	(nm)		(∼0.7%)		
T-2481	50% cut-off	2310±11.5nm	2324	2316	∼0.3%
	(nm)		(∼0.6%)		
Witness2	50% cut-on	1990±10nm	1997	1980	∼0.9%
T-2480	(nm)		(∼0.4%)		
T-2482	50% cut-off	2310±11.5nm	2312	2303	∼0.4%
	(nm)		(∼0.1%)		

		Spec	Measurements
Ks 1	Ave %T btw. 90%	90%	80.65%
T-2479	min %T btw. 90%	80%	75.07%
T-2481	%T < .01% Range	500-3000nm	500-1906, 2492-3000 (nm)
Ks 2	Ave %T btw. 90%	90%	81.95%
T-2480	min %T btw. 90%	80%	76.98%
T-2482	%T < .01% Range	500-3000nm	500-1904, 2504-3000 (nm)
SN002			
Ks 3	Ave %T btw. 90%	90%	79.82%
T-2480	min %T btw. 90%	80%	75.16%
T-2482	%T < .01% Range	500-3000nm	500-1900, 2486-3000 (nm)
SN005			

Bibliography

Ali, B. & Depoy, D. L. 1995, AJ, 109, 709

Allard, F., Hauschildt, P. H., Alexander, D. R., Tamanai, A., & Schweitzer, A. 2001, ApJ, 556, 357

Allen, L. E., Calvet, N., D'Alessio, P., et al. 2004, ApJS, 154, 363

Allen, L. E., Myers, P. C., Di Francesco, J., et al. 2002, ApJ, 566, 993

Allers, K. N., Jaffe, D. T., Luhman, K. L., et al. 2007, ApJ, 657, 511

Alves de Oliveira, C. & Casali, M. 2008, A&A, 485, 155

Ambartsumian, V. A. 1954, Memoires of the Societe Royale des Sciences de Liege, 1, 293

Andre, P., Ward-Thompson, D., & Barsony, M. 1993, ApJ, 406, 122

Audard, M., Briggs, K. R., Grosso, N., et al. 2007, A&A, 468, 379

Bally, J., Reipurth, B., & Davis, C. J. 2007, in Protostars and Planets V, ed. B. Reipurth, D. Jewitt, & K. Keil, 215–230

Baraffe, I., Chabrier, G., Allard, F., & Hauschildt, P. H. 1998, A&A, 337, 403

Baraffe, I., Chabrier, G., Barman, T. S., Allard, F., & Hauschildt, P. H. 2003, A&A, 402, 701

Barrado y Navascués, D., Zapatero Osorio, M. R., Béjar, V. J. S., et al. 2001, A&A, 377, L9

Barsony, M., Kenyon, S. J., Lada, E. A., & Teuben, P. J. 1997, ApJS, 112, 109

Barsony, M., Kenyon, S. J., Lada, E. A., & Teuben, P. J. 1998, VizieR Online Data Catalog, 211, 20109

Barsony, M., Ressler, M. E., & Marsh, K. A. 2005, ApJ, 630, 381

Bertout, C. 2007, in IAU Symposium, Vol. 243, IAU Symposium, ed. J. Bouvier & I. Appenzeller, 1–12

Bessell, M. S. 2005, ARA&A, 43, 293

Beuther, H., Churchwell, E. B., McKee, C. F., & Tan, J. C. 2007, in Protostars and Planets V, ed. B. Reipurth, D. Jewitt, & K. Keil, 165–180

Blaauw, A. 1961, Bull. Astron. Inst. Netherlands, 15, 265

Bochanski, J. J., Hawley, S. L., Reid, I. N., et al. 2005, AJ, 130, 1871

Bondar', N. I. 2002, Astronomy Reports, 46, 489

Bonnell, I. A., Larson, R. B., & Zinnecker, H. 2007, in Protostars and Planets V, ed. B. Reipurth, D. Jewitt, & K. Keil, 149–164

Bontemps, S., André, P., Kaas, A. A., et al. 2001, A&A, 372, 173

Borysow, A., Jorgensen, U. G., & Zheng, C. 1997, A&A, 324, 185

Bouvier, J., Alencar, S. H. P., Boutelier, T., et al. 2007, A&A, 463, 1017

Bouvier, J. & Appenzeller, I. 1992, A&AS, 92, 481

Bouvier, J. & Appenzeller, I., eds. 2007, IAU Symposium, Vol. 243, Star-Disk Interaction in Young Stars

Bouvier, J. & Bertout, C. 1989, A&A, 211, 99

Bouvier, J., Cabrit, S., Fernandez, M., Martin, E. L., & Matthews, J. M. 1993, A&A, 272, 176

Bouvier, J., Covino, E., Kovo, O., et al. 1995, A&A, 299, 89

Brun, A. S. & Zahn, J.-P. 2006, A&A, 457, 665

Buchanan, C. L., Gallimore, J. F., O'Dea, C. P., et al. 2006, AJ, 132, 401

Burrows, C. J., Stapelfeldt, K. R., Watson, A. M., et al. 1996, ApJ, 473, 437

Caballero, J. A., Béjar, V. J. S., Rebolo, R., & Zapatero Osorio, M. R. 2004, A&A, 424, 857

Calvet, N. & Hartmann, L. 1992, ApJ, 386, 239

Cambrésy, L. 1999, A&A, 345, 965

Camenzind, M. 1990, in Reviews in Modern Astronomy, Vol. 3, Reviews in Modern Astronomy, ed. G. Klare, 234–265

Carpenter, J. M., Hillenbrand, L. A., & Skrutskie, M. F. 2001, AJ, 121, 3160

Carpenter, J. M., Hillenbrand, L. A., Skrutskie, M. F., & Meyer, M. R. 2002, AJ, 124, 1001

Carpenter, J. M., Wolf, S., Schreyer, K., Launhardt, R., & Henning, T. 2005, AJ, 129, 1049

Casali, M., Adamson, A., Alves de Oliveira, C., et al. 2007, A&A, 467, 777

Casali, M., Pirard, J.-F., Kissler-Patig, M., et al. 2006, in Presented at the Society of Photo-Optical Instrumentation Engineers (SPIE) Conference, Vol. 6269, Ground-based and Airborne Instrumentation for Astronomy. Edited by McLean, Ian S.; Iye, Masanori. Proceedings of the SPIE, Volume 6269, pp. 62690W (2006).

Casali, M., Pirard, J.-F., Kissler-Patig, M., et al. 2005, The Messenger, 119, 6

Casanova, S., Montmerle, T., Feigelson, E. D., & Andre, P. 1995, ApJ, 439, 752

Chabrier, G. 2003, PASP, 115, 763

Chabrier, G. & Baraffe, I. 1997, A&A, 327, 1039

Chabrier, G., Baraffe, I., Allard, F., & Hauschildt, P. 2000, ApJ, 542, 464

Cieza, L., Padgett, D. L., Stapelfeldt, K. R., et al. 2007, ApJ, 667, 308

Collier Cameron, A. & Campbell, C. G. 1993, A&A, 274, 309

Comeron, F., Rieke, G. H., Burrows, A., & Rieke, M. J. 1993, ApJ, 416, 185

Cushing, M. C., Tokunaga, A. T., & Kobayashi, N. 2000, AJ, 119, 3019

Cutri, R. M., Skrutskie, M. F., van Dyk, S., et al. 2003, 2MASS All Sky Catalog of point sources. (The IRSA 2MASS All-Sky Point Source Catalog, NASA/IPAC Infrared Science Archive. http://irsa.ipac.caltech.edu/applications/Gator/)

Dalton, G. B., Caldwell, M., Ward, A. K., et al. 2006, in Presented at the Society of Photo-Optical Instrumentation Engineers (SPIE) Conference, Vol. 6269, Ground-based and Airborne Instrumentation for Astronomy. Edited by McLean, Ian S.; Iye, Masanori. Proceedings of the SPIE, Volume 6269, pp. 62690X (2006).

Damjanov, I., Jayawardhana, R., Scholz, A., et al. 2007, ApJ, 670, 1337

de Geus, E. J. 1992, A&A, 262, 258

Donati, J. F., Jardine, M. M., Gregory, S. G., et al. 2008, ArXiv e-prints, 804

Eiroa, C., Oudmaijer, R. D., Davies, J. K., et al. 2002, A&A, 384, 1038

Elias, J. H. 1978, ApJ, 224, 453

Elmegreen, B. G. 2006, Meteoritics & Planetary Science, Vol. 41, Supplement, Proceedings of 69th Annual Meeting of the Meteoritical Society, held August 6-11, 2006 in Zurich, Switzerland., p.5022, 41, 5022

Engelbracht, C. W., Young, E. T., Rieke, G. H., et al. 2000, Experimental Astronomy, 10, 403

Enya, K., Yoshii, Y., Kobayashi, Y., et al. 2002, ApJS, 141, 31

Evans, II, N. J., Allen, L. E., Blake, G. A., et al. 2003, PASP, 115, 965

Evans, II, N. J., Allen, L. E., Blake, G. A., et al. 2005, Third Delivery of Data from the c2d Legacy Project: IRAC and MIPS(Pasadena, SSC)

Evans, II, N. J., Harvey, P. M., Dunham, M., et al. 2008, Final Delivery of Data from the c2d Legacy Project: IRAC and MIPS(Pasadena, SSC)

Fazio, G. G., Hora, J. L., Allen, L. E., et al. 2004, ApJS, 154, 10

Fazio, G. G., Hora, J. L., Willner, S. P., et al. 1998, in Presented at the Society of Photo-Optical Instrumentation Engineers (SPIE) Conference, Vol. 3354, Proc. SPIE Vol. 3354, p. 1024-1031, Infrared Astronomical Instrumentation, Albert M. Fowler; Ed., ed. A. M. Fowler, 1024–1031

Feigelson, E. D. & Decampli, W. M. 1981, ApJ, 243, L89

Feigelson, E. D., Gaffney, III, J. A., Garmire, G., Hillenbrand, L. A., & Townsley, L. 2003, ApJ, 584, 911

Feigelson, E. D. & Montmerle, T. 1999, ARA&A, 37, 363

Fernandez, M. & Eiroa, C. 1996, A&A, 310, 143

Flaherty, K. M., Pipher, J. L., Megeath, S. T., et al. 2007, ApJ, 663, 1069

Frommhold, L. 1993, Collision-induced Absorption in Gases (Cambridge, New York: Cambridge University Press)

Gagné, M., Skinner, S. L., & Daniel, K. J. 2004, ApJ, 613, 393

Gallagher, D. B., Irace, W. R., & Werner, M. W. 2003, in Presented at the Society of Photo-Optical Instrumentation Engineers (SPIE) Conference, Vol. 4850, IR Space Telescopes and Instruments. Edited by John C. Mather . Proceedings of the SPIE, Volume 4850, pp. 17-29 (2003)., ed. J. C. Mather, 17–29

Giacconi, R., ed. 1981, Astrophysics and Space Science Library, Vol. 87, X-ray astronomy with the Einstein satellite; Proceedings of the Meeting, Cambridge, MA, January 28-30, 1980

Grankin, K. N., Bouvier, J., Herbst, W., & Melnikov, S. Y. 2008, A&A, 479, 827

Grankin, K. N., Melnikov, S. Y., Bouvier, J., Herbst, W., & Shevchenko, V. S. 2007, A&A, 461, 183

Greene, T. P. & Meyer, M. R. 1995, ApJ, 450, 233

Greene, T. P., Wilking, B. A., Andre, P., Young, E. T., & Lada, C. J. 1994, ApJ, 434, 614

Greene, T. P. & Young, E. T. 1992, ApJ, 395, 516

Grosso, N., Montmerle, T., Bontemps, S., André, P., & Feigelson, E. D. 2000, A&A, 359, 113

Gullbring, E., Calvet, N., Muzerolle, J., & Hartmann, L. 2000, ApJ, 544, 927

Haisch, Jr., K. E., Lada, E. A., & Lada, C. J. 2001, ApJ, 553, L153

Hambly, N. C., Collins, R. S., Cross, N. J. G., et al. 2008, MNRAS, 384, 637

Hartmann, L., Hewett, R., & Calvet, N. 1994, ApJ, 426, 669

Hartmann, L., Megeath, S. T., Allen, L., et al. 2005, ApJ, 629, 881

Harvey, P., Merín, B., Huard, T. L., et al. 2007, ApJ, 663, 1149

Hawarden, T. G., Leggett, S. K., Letawsky, M. B., Ballantyne, D. R., & Casali, M. M. 2001, MNRAS, 325, 563

Hayashi, C. & Nakano, T. 1963, Progress of Theoretical Physics, 30, 460

Herbig, G. H. 1962, Advances in Astronomy and Astrophysics, 1, 47

Herbig, G. H. 2008, AJ, 135, 637

Herbst, W., Bailer-Jones, C. A. L., Mundt, R., Meisenheimer, K., & Wackermann, R. 2002, A&A, 396, 513

Herbst, W., Eislöffel, J., Mundt, R., & Scholz, A. 2007, in Protostars and Planets V, ed. B. Reipurth, D. Jewitt, & K. Keil, 297–311

Herbst, W., Herbst, D. K., Grossman, E. J., & Weinstein, D. 1994, AJ, 108, 1906

Herbst, W. & Shevchenko, V. S. 1999, AJ, 118, 1043

Hester, J. J., Scowen, P. A., Sankrit, R., et al. 1996, AJ, 111, 2349

Hewett, P. C., Warren, S. J., Leggett, S. K., & Hodgkin, S. T. 2006, MNRAS, 367, 454

Hillenbrand, L. A. 1997, AJ, 113, 1733

Houck, J., van Cleve, J., Brandl, B., et al. 2000, in ESA Special Publication, Vol. 456, ISO Beyond the Peaks: The 2nd ISO Workshop on Analytical Spectroscopy, ed. A. Salama, M. F. Kessler, K. Leech, & B. Schulz, 357–+

Imanishi, K., Koyama, K., & Tsuboi, Y. 2001, ApJ, 557, 747

Irwin, M., Lewis, J., Riello, M., et al. 2008, *in preparation*

Irwin, M. J. 1985, MNRAS, 214, 575

Jardine, M., Cameron, A. C., Donati, J.-F., Gregory, S. G., & Wood, K. 2006, MNRAS, 367, 917

Jayawardhana, R. & Ivanov, V. D. 2006, ApJ, 647, L167

Johns-Krull, C. M. & Valenti, J. A. 1996, ApJ, 459, L95+

Johns-Krull, C. M., Valenti, J. A., Hatzes, A. P., & Kanaan, A. 1999, ApJ, 510, L41

Johnstone, D., Wilson, C. D., Moriarty-Schieven, G., et al. 2000, ApJ, 545, 327

Joy, A. H. 1945, ApJ, 102, 168

Joy, A. H. 1949, ApJ, 110, 424

Kaas, A. A. 1999, AJ, 118, 558

Kamata, Y., Koyama, K., Tsuboi, Y., & Yamauchi, S. 1997, PASJ, 49, 461

Kenyon, S. J. & Hartmann, L. 1995, ApJS, 101, 117

Kenyon, S. J., Hartmann, L., Hewett, R., et al. 1994, AJ, 107, 2153

Kenyon, S. J., Lada, E. A., & Barsony, M. 1998, AJ, 115, 252

Kirkpatrick, J. D., Barman, T. S., Burgasser, A. J., et al. 2006, ApJ, 639, 1120

Kirkpatrick, J. D., Reid, I. N., Liebert, J., et al. 1999, ApJ, 519, 802

Kissler-Patig, M., Fontana, A., Venemans, B., et al. 2008a, The Messenger, 132

Kissler-Patig, M., Pirard, J.-F., Casali, M., et al. 2008b, A&A, in press

Koenigl, A. 1991, ApJ, 370, L39

Kumar, S. S. 1963, ApJ, 137, 1121

Lada, C. J. 1987, in IAU Symposium, Vol. 115, Star Forming Regions, ed. M. Peimbert & J. Jugaku, 1–17

Lada, C. J. & Lada, E. A. 2003, ARA&A, 41, 57

Lada, C. J. & Wilking, B. A. 1984, ApJ, 287, 610

Lai, D. 1999, ApJ, 524, 1030

Larson, R. B. 1969, MNRAS, 145, 271

Lawrence, A., Warren, S. J., Almaini, O., et al. 2007, MNRAS, 379, 1599

Liseau, R., Lorenzetti, D., Molinari, S., et al. 1995, A&A, 300, 493

Lodieu, N., Dobbie, P. D., Deacon, N. R., et al. 2007, MNRAS, 380, 712

Lombardi, M., Lada, C. J., & Alves, J. 2008, A&A, 480, 785

Lucas, P. W. & Roche, P. F. 2000, MNRAS, 314, 858

Lucas, P. W., Roche, P. F., Allard, F., & Hauschildt, P. H. 2001, MNRAS, 326, 695

Lucas, P. W., Weights, D. J., Roche, P. F., & Riddick, F. C. 2006, MNRAS, 373, L60

Luhman, K. L. 2004, ApJ, 617, 1216

Luhman, K. L., Joergens, V., Lada, C., et al. 2007, in Protostars and Planets V, ed. B. Reipurth, D. Jewitt, & K. Keil, 443–457

Luhman, K. L., Liebert, J., & Rieke, G. H. 1997, ApJ, 489, L165+

Luhman, K. L. & Rieke, G. H. 1999, ApJ, 525, 440

Luhman, K. L., Whitney, B. A., Meade, M. R., et al. 2006, ApJ, 647, 1180

Lynden-Bell, D. & Pringle, J. E. 1974, MNRAS, 168, 603

Martín, E. L., Delfosse, X., Basri, G., et al. 1999, AJ, 118, 2466

Martin, E. L., Montmerle, T., Gregorio-Hetem, J., & Casanova, S. 1998, MNRAS, 300, 733

Martín, E. L., Zapatero Osorio, M. R., Barrado y Navascués, D., Béjar, V. J. S., & Rebolo, R. 2001, ApJ, 558, L117

Megeath, S. T., Allen, L. E., Gutermuth, R. A., et al. 2004, ApJS, 154, 367

Mohanty, S. 2007, in IAU Symposium, Vol. 243, IAU Symposium, ed. J. Bouvier & I. Appenzeller, 345–356

Mohanty, S., Jayawardhana, R., & Basri, G. 2005, ApJ, 626, 498

Montmerle, T., Koch-Miramond, L., Falgarone, E., & Grindlay, J. E. 1983, ApJ, 269, 182

Moorwood, A., Brandner, W., Comeron, F., et al. 2003, Science case for 0.9-2.5micron infrared imaging with the VLT (ESO Archive), http://www.eso.org/projects/iridt/irace/pdffiles/HAWK

Motte, F., Andre, P., & Neri, R. 1998, A&A, 336, 150

Najita, J. R., Tiede, G. P., & Carr, J. S. 2000, ApJ, 541, 977

Nakajima, T., Oppenheimer, B. R., Kulkarni, S. R., et al. 1995, Nature, 378, 463

Natta, A., Testi, L., Comerón, F., et al. 2002, A&A, 393, 597

Nikolaev, S., Weinberg, M. D., Skrutskie, M. F., et al. 2000, AJ, 120, 3340

Oppenheimer, B. R., Kulkarni, S. R., Matthews, K., & Nakajima, T. 1995, Science, 270, 1478

Ozawa, H., Grosso, N., & Montmerle, T. 2005, A&A, 429, 963

Padgett, D. L., Rebull, L. M., Stapelfeldt, K. R., et al. 2008, ApJ, 672, 1013

Padoan, P. & Nordlund, Å. 2002, ApJ, 576, 870

Peacock, J. A. 1983, MNRAS, 202, 615

Persson, S. E., Murphy, D. C., Krzeminski, W., Roth, M., & Rieke, M. J. 1998, AJ, 116, 2475

Pizzolato, N., Maggio, A., Micela, G., Sciortino, S., & Ventura, P. 2003, A&A, 397, 147

Porras, A., Jørgensen, J. K., Allen, L. E., et al. 2007, ApJ, 656, 493

Preibisch, T., Kim, Y.-C., Favata, F., et al. 2005, ApJS, 160, 401

Ray, T., Dougados, C., Bacciotti, F., Eislöffel, J., & Chrysostomou, A. 2007, in Protostars and Planets V, ed. B. Reipurth, D. Jewitt, & K. Keil, 231–244

Reach, W. T., Megeath, S. T., Cohen, M., et al. 2005, PASP, 117, 978

Rebolo, R., Zapatero-Osorio, M. R., & Martin, E. L. 1995, Nature, 377, 129

Rebull, L. M., Stapelfeldt, K. R., Evans, II, N. J., et al. 2007, ApJS, 171, 447

Reipurth, B., Aspin, C., Beck, T., et al. 2007a, AJ, 133, 1000

Reipurth, B. & Clarke, C. 2001, AJ, 122, 432

Reipurth, B., Jewitt, D., & Keil, K., eds. 2007b, Protostars and Planets V

Riddick, F. C., Roche, P. F., & Lucas, P. W. 2007, MNRAS, 381, 1067

Ridge, N. A., Di Francesco, J., Kirk, H., et al. 2006, AJ, 131, 2921

Rieke, G. H., Blaylock, M., Decin, L., et al. 2008, AJ, 135, 2245

Rieke, G. H. & Lebofsky, M. J. 1985, ApJ, 288, 618

Robin, A. C., Reylé, C., Derrière, S., & Picaud, S. 2003, A&A, 409, 523

Schmitt, J. H. M. M., Robrade, J., Ness, J.-U., Favata, F., & Stelzer, B. 2005, A&A, 432, L35

Scholz, A. & Eislöffel, J. 2005, A&A, 429, 1007

Schultheis, M., Ganesh, S., Glass, I. S., et al. 2000, A&A, 362, 215

Schulz, N. S. 2005, From Dust To Stars Studies of the Formation and Early Evolution of Stars (From Dust To Stars Studies of the Formation and Early Evolution of Stars, by N.S. Schulz. Springer-Praxis books in astrophysics and astronomy. Praxis Publishing Ltd, 2005. ISBN 3-540-23711-9)

Sciortino, S., Pillitteri, I., Damiani, F., et al. 2006, in Proceedings of the The X-ray Universe 2005 (ESA SP-604). 26-30 September 2005, El Escorial, Madrid, Spain. Editor: A. Wilson, p.111, ed. A. Wilson, 111–+

Shu, F., Najita, J., Ostriker, E., et al. 1994, ApJ, 429, 781

Shu, F. H., Adams, F. C., & Lizano, S. 1987, ARA&A, 25, 23

Skrutskie, M. F., Meyer, M. R., Whalen, D., & Hamilton, C. 1996, AJ, 112, 2168

Stanke, T., Smith, M. D., Gredel, R., & Khanzadyan, T. 2006, A&A, 447, 609

Stassun, K. G., Mathieu, R. D., Mazeh, T., & Vrba, F. J. 1999, AJ, 117, 2941

Stassun, K. G., van den Berg, M., & Feigelson, E. 2007, ApJ, 660, 704

Stassun, K. G., van den Berg, M., Feigelson, E., & Flaccomio, E. 2006, ApJ, 649, 914

Strom, K. M., Kepner, J., & Strom, S. E. 1995, ApJ, 438, 813

Strom, K. M., Strom, S. E., Edwards, S., Cabrit, S., & Skrutskie, M. F. 1989, AJ, 97, 1451

Struve, O. & Rudkjøbing, M. 1949, ApJ, 109, 92

Tokunaga, A. T. & Vacca, W. D. 2005, PASP, 117, 421

Treister, E., Urry, C. M., Van Duyne, J., et al. 2006, ApJ, 640, 603

Vrba, F. J. 1977, AJ, 82, 198

Vrba, F. J., Rydgren, A. E., Chugainov, P. F., Shakovskaia, N. I., & Zak, D. S. 1986, ApJ, 306, 199

Vrba, F. J., Strom, K. M., Strom, S. E., & Grasdalen, G. L. 1975, ApJ, 197, 77

Wainscoat, R. J., Cohen, M., Volk, K., Walker, H. J., & Schwartz, D. E. 1992, ApJS, 83, 111

Walker, M. F. 1972, ApJ, 175, 89

Walter, F. M. 1987, in IAU Symposium, Vol. 122, Circumstellar Matter, ed. I. Appenzeller & C. Jordan, 107–+

Welch, D. L. & Stetson, P. B. 1993, AJ, 105, 1813

Welsh, H. L., Crawford, M. F., & Locke, J. L. 1949, Phys. Rev., 76, 580

Whelan, E. T., Ray, T. P., Bacciotti, F., et al. 2005, Nature, 435, 652

Whitworth, A., Bate, M. R., Nordlund, Å., Reipurth, B., & Zinnecker, H. 2007, in Protostars and Planets V, ed. B. Reipurth, D. Jewitt, & K. Keil, 459–476

Wilking, B. A. 1992, Star Formation in the Ophiuchus Molecular Cloud Complex (Low Mass Star Formation in Southern Molecular Clouds), 159–+

Wilking, B. A., Gagné, M., & Allen, L. E. 2008, in Handbook of Low Mass Star Forming Regions Vol II: The Southern Sky, ed. B. Reipurth, in press

Wilking, B. A., Greene, T. P., & Meyer, M. R. 1997, in Bulletin of the American Astronomical Society, Vol. 29, Bulletin of the American Astronomical Society, 1317–+

Wilking, B. A. & Lada, C. J. 1983, ApJ, 274, 698

Wilking, B. A., Lada, C. J., & Young, E. T. 1989, ApJ, 340, 823

Wilking, B. A., Meyer, M. R., Robinson, J. G., & Greene, T. P. 2005, AJ, 130, 1733

Wilson, C. D., Avery, L. W., Fich, M., et al. 1999, ApJ, 513, L139

Zapatero Osorio, M. R., Béjar, V. J. S., Martín, E. L., et al. 2000, Science, 290, 103

Acknowledgments

The list of people I want to thank to is long, but is worth writing it because without them this thesis would not have been possible. Twenty years ago I was starting my primary school in a small village in the north of Portugal. If someone had told me back then that this is where I would be now, I would most probably have laughed at it, or even ran away. Many years of dedicated work softened by a wonderful family, a caring boyfriend, many good friends, and inspiring mentors. Let's name them.

I would like to thank my supervisor Mark Casali, for the support and encouragement during this work, for the many meetings over these 3 years, but mainly for starting me off in star formation research. Thank you for teaching me to be precise with my science, and for giving me space to find myself as a young scientist. Thank you for encouraging my participation in important international conferences, where I've learned a lot and had a chance to present my work.

I also want to thank my supervisor at the LMU, Andreas Burkert, for finding time in his tight schedule to meet me, and for showing interest and giving useful advice about my work.

All my Ph.D. work was done at ESO, where I have to thank the great conditions which were offered to me at so many levels, from the interesting and constant scientific discussions, to the very efficient IT support. All these things make one's life easier and I cannot think of a better place to have spent these three years than in this institution. In particular, I would like to thank Bruno Leibundgut for always finding time for a little chat and for the wise advice I got from him. Also, thank you for reading this thesis!

I will also like to thank Jeff Pirard and Markus Kissler-Patig for letting me go on board the HAWK-I project, and specially for taking me with the team for the commissioning in Paranal. I've learnt a lot during that time, and I am very thankful I was given the chance to see how an instrument is build from the laboratory to the telescope.

Another inspiring scientist I have to thank to is Bo Reipurth, for hosting me in his institute in Hawaii for some weeks. It was inspiring to discuss science with him, but above all I thank him for sharing with me his knowledge of astronomy.

Many friends at ESO have made these years memorable. I have started the Ph.D. together with Mariya, whose support has always been important to me. Other students have helped me in many ways, from programming to comic relief, they are Daniela, Marcelo, Carmona, Andreas, Karina, Jarek, Jouni, Davide, Steffano, Gerrit, Audrey, Gina, Fatme, Silvia, Briggita, Veronica, Claudio, and probably others that I now forget to mention. A very special thanks goes to Tina, with whom I've share the office in these last years. From tears to laughter, we have shared the many days of this Ph.D. life and learned together how to survive it. Thanks for your patience!

I owe a special thanks to my friends in Munich, who shared with me the life outside work. The portuguese community, Luis, Andrea, Sofia, Pedro, Mariana, Raul, Paulo, Bruno, Aires, Joana, Luis Dj, Mafalda, and Alex and Katrin, for being with me in so many concerts, dinners, nights out, or trips to the lake, and with whom I always had a lot of fun. I have to thank to other friends spread all over the world whom I visited and who visited me, and besides the distance remain so important in my life, Aaron, Shahram, Regina, William, and Goran.

This thesis is dedicated to my parents, Jose and Sameiro, to whom I owe much of who I am. Thank you for believing that education is the best investment, for always encouraging me to go further, for all the good values that you have passed on to me, for building a family that is still the key to my achievements and to whom I know I can always come back. Thank you for helping me moving around the world so many times, for finding me an apartment in Munich, for calling me many times to know how I am, for giving me comfort and strength when things go wrong, and for being proud of me when I succeed. You are the best parents in the world, and you have done a great job in raising us the way you did, thank you. Also to my two sisters, Andreia and Marta, my best friends. I can only be happy when they are too, and they are the inspiration in my life and in my work. Thank you for visiting me, for keeping contact by phone, email, and postcards!, for sharing with me your achievements, for always supporting and believe in what I am doing. And thank you as well Bruno! Finally, thank you Johannes, for being there for me every day, to bring solace in the bad moments and celebrate the good ones, for helping me to overcome difficulties and fears, for the great adventures around the world, and for making me happy every day of my life.